The Thesis committee for Joshua Bruce Burrus

Certifies that this is the approved version of the following thesis:

Structural and stratigraphic evolution of the Weepah Hills Area, NV - Transition from Basin-and-Range extension to Miocene core complex formation

APPROVED BY

SUPERVISING COMMITTEE:

Supervisor: _____

Daniel Stockli

_____

Mark Cloos

_____

Richard Ketcham

Structural and stratigraphic evolution of the Weepah Hills Area, NV - Transition from Basin-and-Range extension to Miocene core complex formation

by

Joshua Bruce Burrus, B.S.

Thesis

Presented to the Faculty of the Graduate School

of the University of Texas at Austin

in Partial Fulfillment

of the Requirements

for the Degree of

Master of Science in Geological Sciences

The University of Texas at Austin

May 2013

Acknowledgements

The research presented in this transcript was funded by the Department of Energy under the topic area 'Validation of Innovative Exploration Technologies'. Additional funding from Ram Power Corporation also contributed necessary financial and logistical support for this research project. Financial support was also obtained from the University of Texas at Austin and the University of Kansas Department of Geology. I thank my wife, Heather Harryman, for moral support and patience during my graduate career. I am very grateful for the moral support and advice given to me from members of the isotope geochemistry and thermochronolgy lab group, both while at the University of Kansas and at the University of Texas at Austin. A special thank you goes out to my advisor Dr. Danny Stockli, whose guidance and help with this project could never be overstated. I am grateful for all of the guidance and input from the members of my committee. I would like to thank all of the researchers working in the Clayton Valley area for their assistance and guidance; Joshua Feldman from the University of Kansas; Dr. Charles Verdel; Caleb Stoup from Ram Power Corporation; Dr. Katie Keranen, Matthew McGuire and Cullen Hoag from the University of Oklahoma; Dr. LeeAnn Munk from the University of Alaska at Anchorage.

Structural and stratigraphic evolution of the Weepah Hills Area, NV - Transition from Basin-and-Range extension to Miocene core complex formation

by

Joshua Bruce Burrus, M.S.Geo.Sci.

The University of Texas at Austin, 2013

SUPERVISOR: Daniel Stockli

The Weepah Hills Area (Nevada) exposes exhumed metamorphic and plutonic rocks and upper-plate (supradetachment) volcano-sedimentary rocks that have experienced a complex, multi-stage deformational and depositional history. The Weepah Hills metamorphic core complex (WHMCC) is located in a region of the western Cordillera that was affected by both Miocene Basin-and-Range style E-W extension and Mio-Pliocene Walker Lane transcurrent shearing. Mio-Pliocene transcurrent deformation is transferred across a ~175 km releasing bend, known as the Mina Deflection, that kinematically links dextral strike-slip faults of the Death Valley-Fish Lake Valley with the central Walker Lane Belt. Progressive Mio-Pliocene transtension is characterized by core complex detachment faulting and younger high-angle normal faults. Timing of detachment faulting is constrained by both (U-Th)/He thermochronometry of footwall rocks and detailed chronostratigraphy of upper-plate strata to between 9-6 Ma. This age is supported by deformation recorded in the upper-plate strata that is attributed to progres-

sive folding of the detachment associated with corrugation development. Earlier Miocene Basin-and-Range style extension is characterized by N-S trending high-angle normal faults and half-grabens that are strongly overprinted by Mio-Pliocene structures. (U-Th)/He zircon cooling ages from the detachment footwall range from ~12-20 Ma and are attributed to exhumation and unroofing related to E-W Basin-and-Range extension. New detailed sedimentological and geochronologic data show that, in contrast to previous research, the WHMCC upper-plate strata do not form a single supradetachment package, but rather three temporally distinct Miocene stratigraphic packages bounded by angular unconformities. The stratigraphic, structural, and exhumational record preserved in the WHMCC elucidates the timing of deformation and sedimentary basin evolution related to both Basin-and-Range E-W extension and Walker Lane related NW-directed transtension.

Table of Contents

List of Tables

List of Figures

1. INTRODUCTION

Due to the complex interaction of tectonic processes (sedimentation, exhumation, erosion, faulting) governing tectonic response in highly extended terrains, the evolution of sedimentary basins generated in these environments is still poorly constrained in many areas. In some well-exposed localities, the timing of exhumation and uplift along various structures can often be inferred solely by the record of basin sedimentation due to the direct control faulting exerts on patterns of sedimentation and synextensional basin formation (Dorsey and Becker, 1995). On the other hand, many regions of large-magnitude extension (>10 km) that have experienced detachment faulting lack a precise temporal and spatial association between the upper-plate sediments and structures controlling their deposition and morphology due to a lack of marker beds needed to correlate dismembered basin sediments (Dorsey and Becker, 1995; Oldow, 2009).

The Weepah Hills metamorphic core complex (WHMCC) is marked by a lithologically similar but temporally diverse stratigraphy, resulting in a stratigraphic sequence that is not characteristic of a particular depositional setting (supradetachment or half-graben), and hinders correlation across faults active during deposition. Unraveling the depositional history of these domains has implications for the timing of regional structural events and relies on the ability to differentiate temporally disparate sediment packages (Friedman et al., 1996). Regional mapping with thermochronologic techniques is an approach necessary to unravel basin evolution in localities that experienced a multistage depositional history. There are three hypotheses for the depositional history of the

sediments of the WHMCC: 1) the strata record deposition solely in a half-graben basin geometry during early Miocene east-west extension, 2) deposition in one supradetachment basin during Miocene transtension, 3) deposition that records the pre-, syn-, and post-tectonic evolution of the WHMCC. The presence of volcanic sediments in the upper-plate sediments of the WHMCC yields a unique opportunity to apply temporal constraints using (U-Th)/He and U-Pb zircon chronometry to an area that has experienced a complex history of faulting. By correlating the zircon chronometry from the upper-plate with zircon and apatite chronometry from the lower plate, this study concludes that basin sediments represent deposition from Oligo-Miocene to early Miocene time, and records the kinematic transition from east-west extension to transtension.

2. TECTONIC SETTING

Western Nevada has experienced two major episodes of Tertiary extension. The earlier episode is associated with early to middle Miocene Basin and Range style east-west extension characterized by N-NW striking normal faults and tilted footwall blocks characteristic of the Basin and Range province (Figure 1) (Proffett, 1977; Stockli et al., 2002; Surpless et al., 2008). Later transtension, driven by stress propagating to the north-east from the Pacific and North America plate boundary (Dokka and Travis, 1990; Henry et al., 2007), resulted in the exhumation of mid-crustal rocks along low-angle normal faults in accommodation zones punctuated by attenuated continental crust (Figure 2) (Stockli et al., 2003; Oldow et al., 2008). Strain generated by movement along the Pacific and North America plate boundary is not entirely accommodated along the San Andreas Fault system; ~9 to 14 mm of motion per year propogates northward into the eastern California shear zone (ECSZ) and the Walker Lane structural belt (Humphries and Weldon, 1994; Bennett et al., 2003; Hoeft and Frankel, 2010). Although the two structural domains are both comprised of Cenozoic extensional structures and are kinematically linked in the Pliocene, the Walker Lane belt and ECSZ differ in their structural evolution and timing of inception (Oldow et al., 2008).

The Walker Lane structural belt is comprised primarily of northwest-trending dextral strike-slip faults, forming a structural boundary that separates the extended crust of the Basin and Range province from the nearly undeformed Sierra Nevada block (Figure 1) (Hardyman and Oldow, 1991; Oldow, 2003; Wesnousky, 2005). Basin and Range

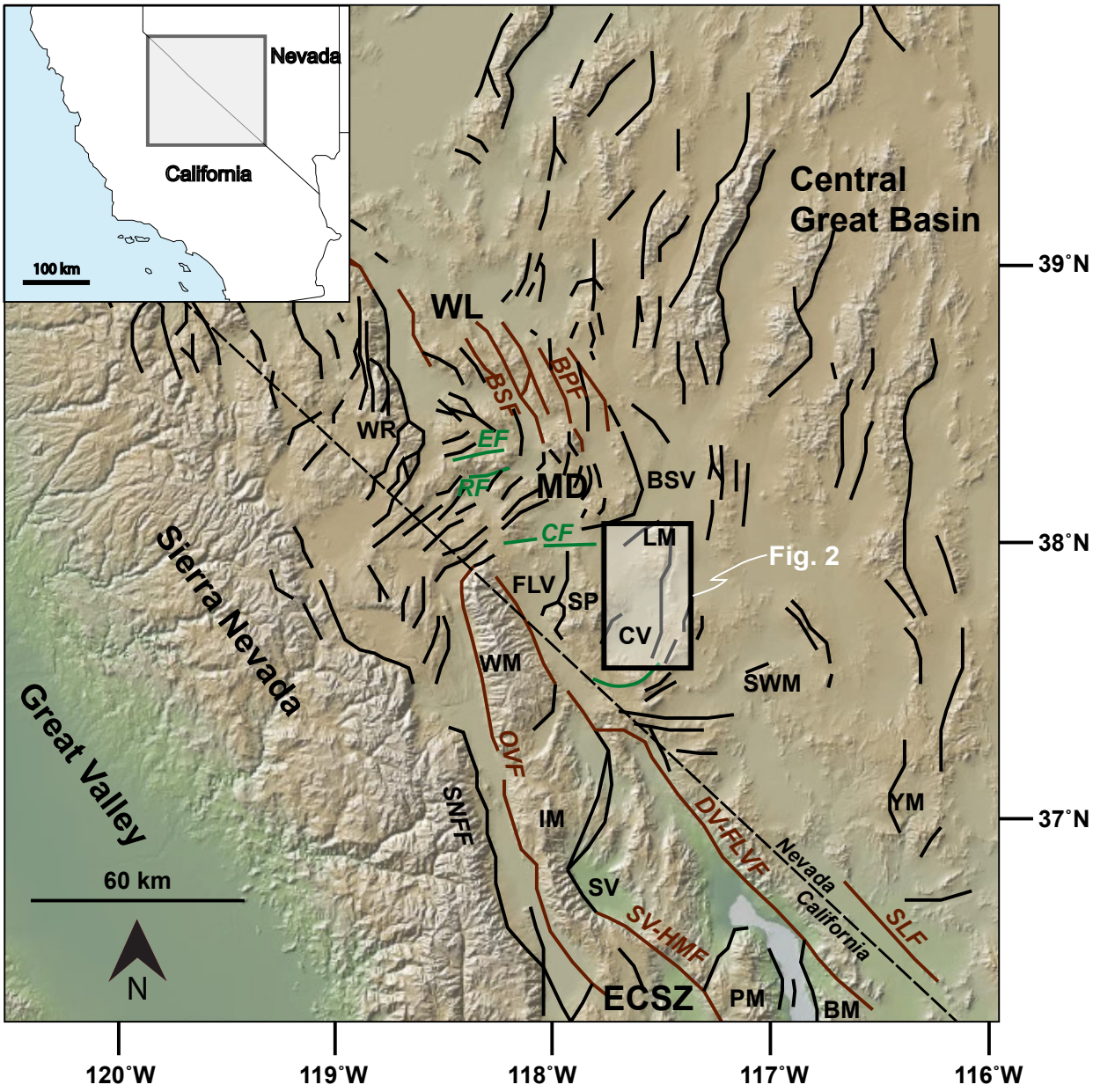

Figure 1: Major late Cenozoic faults of the western Great Basin and Sierra Nevada. Normal faults-black; dextral strike-slip faults-orange; sinistral strike-slip faults-green. Image is Global Multi-Resolution Topography (http://www.geomapapp.org). Cenozoic faults after Oldow et al., (2009). BM-Bare Mt.; BPF-Bettles Well-Petrified Springs fault; BSF-Benton Springs fault; BSV-Big Smokey Valley; CF-Coaldale fault; CGB-Central Great Basin; CV-Clayton Valley; DV-FLVF-Death Valley-Fish Lake Valley fault; ECSZ-eastern California shear zone; EF- Excelsior Mts. fault; FLV-Fish Lake Valley; LM-Lone Mt.; IM-Inoyo Mts.; MD-Mina Deflection; OVF-Owens Valley fault; PM-Panamint Mts.; RF-Rattlesnake Flat fault; SLF-Stateline fault; SNB-Sierra Nevada batholith; SNFF-Sierra Nevada Frontal fault; SP-Silver Peak Range; SV-HMF-Saline Valley-Hunter Mt. fault; SV-Saline Valley; SWM-Stonewall Mt.; WL-Walker Lane structural belt; WM-White Mts.; WR-Wassuk Range; YM-Yucca Mt.

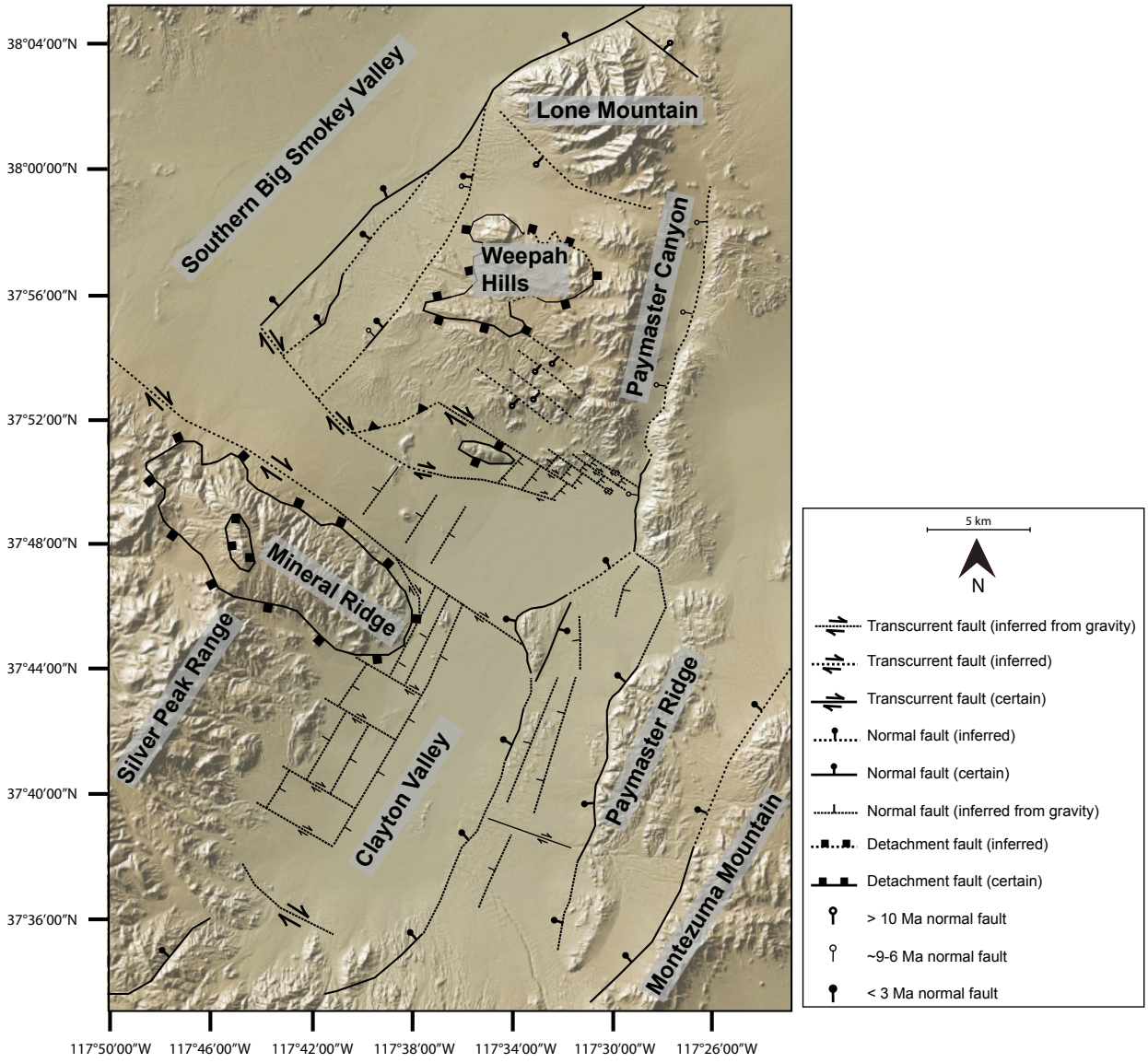

Figure 2: Global Multi-Resolution Topography image of Clayton Valley and Southern Big Smokey Valley area. High-angle normal faults are differentiated based on timing of activity. The major Mio-Pliocene high-angle normal faults and transcurrent faults produce a structural step-over that kinematically links the Eastern California shear zone and the Walker Lane structural belt through a complex network of faults that tranfers strain across the Silver Peak-Lone Mountain extensional domain. Faulting prior to 10 Ma accomodated extension during early Miocene Basin and Range style extension. Imagery from http://www.geomapapp.org; Ryan et al., (2009).

extension initiated in the Walker Lane across the late Oligocene to early Miocene time (Stewart, 1998; Stockli, 2003; Surpless et al., 2002), producing north-south striking normal faults with pronounced rotation in the footwall block that typically tilt toward the west (Dilles and Gans, 1995; Stockli et al., 2003; Stewart, 1998; Surpless et al., 2002). Structural and thermochronometric data across the Walker Lane suggests the amount of extension during the earlier stage of Tertiary extension in the Walker Lane varies from younger, middle Miocene extension (~12 Ma) along the western boundary of the region, to highly extended (>150% extension) terrains revealing early Miocene exhumation further to the east. This structural trend suggests a westward propagation of extensional deformation in the Walker Lane belt (Wernicke, 1992; Stockli et al., 2000; Surpless et al., 2002). The mechanism promoting extension is believed to be tectonically derived from the increasing angle of the subducted Farallon Slab under the North American craton (Christiansen et al., 1992).

After progressively impinging further west throughout the early and middle Miocene, large-magnitude extension began to dissipate as the western extent of the North American plate margin underwent a major tectonic rearrangement from a predominately convergent margin to a dextral transform boundary (Atwater and Stock, 1998; Dixon et al., 2000; Faulds and Henry, 2008). The reorganization of the boundary between the Pacific and North American plate, induced a later episode of deformation resulting in the generation of the ECSZ and the continuous transtension from the late-Miocene to present time experienced in the Walker Lane (Atwater and Stock, 1998; Faulds and Henry, 2008).

Several north-east striking right-lateral strike-slip fault systems of the ECSZ transfer strain to and reactivate normal faults of the Walker Lane belt by means of releasing bends (~100-150 km wide), resulting in accommodation zones of highly extended continental crust (Figure 1) (Stewart, 1985, 1998; Stockli et al., 2003; Oldow et al., 2008).

There are four primary right-lateral fault systems actively accommodating dextral shear within the ECSZ and Walker Lane from late Miocene to early Pliocene time: the Death Valley-Fish Lake Valley, the Owens Valley-White Mountains, the Saline Valley-Hunter Mountain, and the Stateline fault systems (Figure 1) (Oswald and Wesnousky, 2002; Kylander and Clark et al., 2005; Bartley et al., 2007; Frankel et al. ,2008). Large-magnitude extension (~8 km) was accommodated during the early Miocene along these transcurrent fault systems, and is responsible for range-forming crustal fault blocks (e.g. White and Inyo Mountains) that form the western-most boundary of the north-central Basin and Range province (Stockli et al., 2003). These strike-slip fault systems of the ECSZ are kinematically linked to the northwest trending faults of the Walker Lane belt via eastward, propagating releasing bends (Stewart, 1985; Nielsen, 1965; Oldow et al., 2001; Wesnousky, 2005b; Hoeft and Frankel, 2010). These eastward structural stopovers, including the Mina Deflection, the Emigrant Peak fault and the Silver Peak-Lone Mountain extensional complex (SPLM), form major strain transfer zones that transmit motion away from the plate boundary by means of the ECSZ, eventually propogating into the Walker Lane since the late Miocene (Figures 1 and 2) (Reheis and Sawyer, 1997; Oldow et al., 2008; Ganev et al., 2010; Hoeft and Frankel, 2010).

The Mina Deflection is an extensional step-over largely comprised of east-west trending strike-slip faults that accommodate deformation within the step-over by means of clockwise block rotations and left-lateral motion (Stewart, 1985; Oldow, 1992; Faulds, 2005; Stockli et al., 2003; Oldow et al., 2008). The SPLM extensional complex is a complex network of transtensional and extensional faulting that bypasses the northern Mina Deflection and is responsible for the exhumation of metamorphic core complexes between the northwest-trending Death Valley-Fish Lake Valley fault system into the Walker Lane, therefore bypassing the northern Mina Deflection (Figure 2) (Reheis and Sawyer, 1997; Oldow, 1992; Oldow et al., 2008; Hoeft and Frankel, 2010). The SPLM topography is marked by elevated exposures of metamorphosed upper Proterozoic to lower Paleozoic meta-sedimentary rocks intruded by multiple episodes of plutonism (Robinson et al., 1976; Oldow et al., 1994). These range forming structures have experienced metamorphism in the range of greenschist to amphibolite facies exposed at Mineral Ridge, in the Weepah Hills and at Lone Mountain (Oldow et al., 1994). Folding and imbrication in the lower Paleozoic section is attributed to shortening during the middle Paleozoic and early Mesozoic (Oldow, 1984). Three exposures of the intruded meta-sedimentary rocks define northwest-trending doubly plunging antiforms (Kirsch, 1971), forming corrugations in the detachment faults. The northwest-trending detachment bounded exposures are overlain on their flanks by faulted sedimentary and volcanic rocks primarily believed to be deposited throughout the Tertiary (Stewart and Diamond, 1990; Oldow, 1994; Petronis et al., 2007). Volcanic and sedimentary packages unconformably overlie isolated outcrops

of lower Paleozoic strata in the upper plate of the detachment (Stewart and Diamond, 1990; Petronis et al., 2007). The Tertiary sediments are affected by two generations of high-angle normal faults, one associated with east-west extension and the second generation attributed to later transtension (Figures 2 and 3) (Stewart and Diamond, 1990; Oldow et al., 2009). The detachment fault cuts the older system of high-angle normal faults, but is decapitated by the Pliocene faults. Both the Mina Deflection and the SPLM extensional complex have been active since the late Miocene (Oldow, 1992; Stockli, 2003; Oldow et al., 2008; Schroeder et al., in prep.), with the transient strain transferred through the accommodation zones by the right-lateral strike-slip fault systems that define the Walker Lane belt (Stewart, 1988; Oldow et al., 2001; Oldow, 2003; Wesnousky, 2005). In recent geologic history, the amount of movement accomodated along transcurrent and high-angle normal faults within the SPLM and WHMCC systems form a region of dextral shear accommodation at a rate of 3.3-5.2 mm/yr based on geologic evidence (Hoeft and Frankel 2010; Foy et al., 2012). This is only about half of the geodetically derived rate of 9.3±0.2 mm/yr (Bennett et al., 2003).

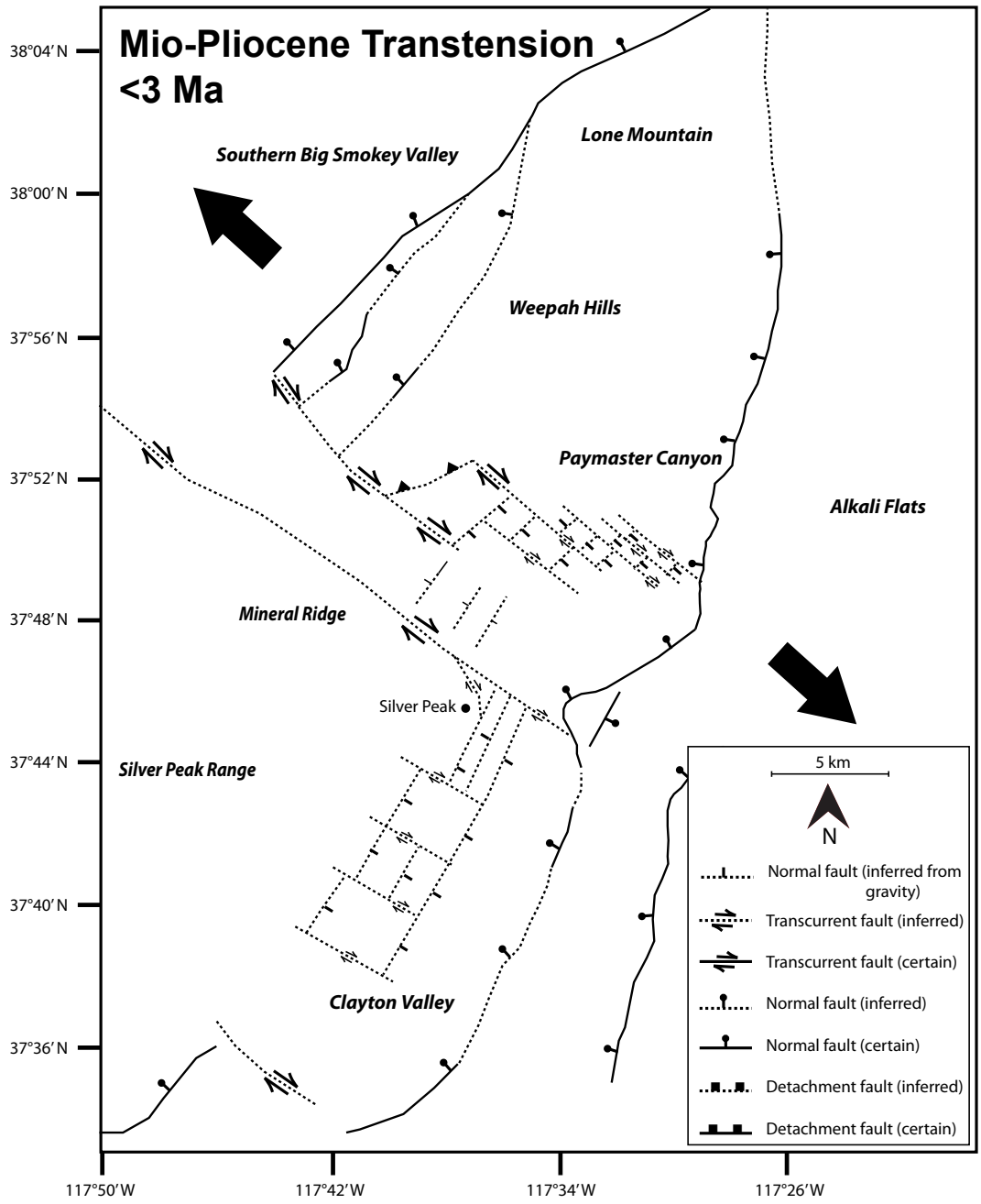

Figure 3: Diagram illustrating the progressive tectonic evolution of the Silver Peak-Lone Mountain extensional complex. The bold arrows represent the approximate maximum extension direction, resulting in oblique extension (Oldow et al., 2008). High-angle normal faults and detachment faulting active during Mio-Pliocene transtension. These serve as a releasing bend that kinematically link the eastern California shear zone (ECSZ) and Walker Lane belt. Dextral transcurrent faults and high-angle normal faults have accomodated transtension since ~3 Ma and presently kinematically link the ECSZ and Walker Lane belt..

3. METHODOLOGY

3.1 Apatite and zircon (U-Th)/He dating

(U-Th)/He thermochronometry is a dating technique utilized to constrain the time-temperature history of various geologic processes including sediment deposition and cooling of rocks moving from depth during large-magnitude extension. The technique is based on the abundance of ^{4}He, also known as an alpha particle, produced by the radioactive decay of the isotopes ^{238}U, ^{235}U, ^{232}Th and ^{147}Sm (Zeitler et al., 1987; Farley et al., 1996; Wolf et al., 1996). The alpha particles can be retained or diffuse through the crystal lattice of a mineral. The diffusive loss of alpha particles is controlled by thermally activated volume diffusion, the rate of which depends upon mineral properties (Shuster and Farley, 2005). Apatite and zircon are two accessory minerals that are commonly utilized as thermochronometers.

The characterization of helium retentivity in minerals has evolved from the early work of Dodson (1973) who defined closure temperature (Tc) for a geochronologic system as the temperature at the time corresponding to its apparent age, assuming roughly linear cooling, recording the time at which a chemical system becomes “frozen”. In the (U-Th)/He system, the closure temperature corresponds to the time at which the host mineral begins to retain ^{4}He. Closure temperature estimates are utilized in thermochronology when characterizing various minerals. Zircon has been experimentally show to have a Tc of ~180˚C (Reiners et al., 2004). The term closure temperature can be misleading because

mineral systems actually have a temperature range in which helium is both partially retained and diffused, not a discrete temperature across which helium is completely ejected or retained (Dodson, 1973). This is termed the helium partial retention zone and ranges from ~140˚-180˚C for zircon and ~40˚-80˚C for apatite (House et al., 2000; Stockli et al., 2000; Farley, 2000). Thus, utilizing both apatite helium thermochronometry (AHe) and zircon helium thermochronometry (ZHe) techniques allows for an interpretation of the thermal evolution of a sample through a temperature range spanning from ~40-180˚C. The concept of a helium partial retention zone is applicable to exhumed crustal material that resides in the partial retention zone for a resolvable period of time, while the concept of a closure temperature can be applied to rapidly cooled material (e.g. eruptive material). The ratio of the daughter product to the four radioactive parent isotopes yields an age at which the mineral cooled below the closure temperature. The (U-Th)/He uncorrected ages are calculated using the following age equation:

$$^{4}He=8^{238}U(e^{\lambda 238t}-1)+7(^{238}U/137.88)(e^{\lambda 235t}-1)+6^{232}Th(e^{\lambda 232t}-1)+^{147}Sm(e^{\lambda 147t}-1) \quad \text{(equation 1)}$$

where 238λ, 235λ, and 232λ are decay constants for their respective isotopes and ^{238}U, ^{235}U, ^{232}Th, ^{147}Sm and ^{4}He are concentrations of the various isotopes. Due to the ~20 μm travel distance of an ejected alpha particle, there is a fractional loss of alpha particles from the outer ~20 μm of the mineral grain that must be accounted for when making age determinations (Farley, 1996). Termed the alpha ejection correction, this statistical correction accounts for alpha particles produced but not retained in the mineral lattice after

the grain has cooled below the closure temperature. All grains analyzed in this study had an alpha ejection correction applied to age calculations. In order to determine a ZHe or AHe age the grains are heated with a laser, allowing for the retained helium to escape the grain and the helium concentration to be determined. The grain is then dissolved and analyzed by the inductively coupled plasma mass-spectrometer (ICP-MS) to determine the concentration of the various isotopes of uranium, thorium and samarium.

ZHe has been shown to be a reliable thermochronometer for the (U-Th)/He system and is a technique that has been broadly utilized in studies of extension in the western U.S. (Stockli, 2005). (U-Th)/He thermochronology is particularly well-suited for the Clayton Valley region due to its sensitivity to a temperature range that encompasses the scope of upper-crustal processes associated with geothermal resources (Stockli, 2005). The majority of analyses conducted for this study are cooling ages derived from utilizing the (U-Th)/He system in zircon. Due to the prevalence of mineral inclusions observed in apatites from the WHMCC, ZHe is favored over AHe for determining cooling ages on volcaniclastic tuffaceous sediments in this study. In volcanic sediments, which are the majority of those sampled in the basin sediments of this study, the (U-Th)/He age obtained in the analysis of zircon reflect the eruptive age of the mineral, and is thus a geochronologic age as opposed to a thermochronometric age. The average ZHe age for the grains analyzed from a sample is interpreted as the eruptive age of volcanic rocks and cooling age of plutonic rocks. For volcanic rocks, the average represents the age of grains that are determined not to be inherited or lost during analysis. Grains are determined to be

lost during analyses by examining the data for aliquots that lack concentrations of parent isotopes. A lack of parent isotopes suggests the grain was lost during the dissolution process before analysis on the ICP-MS, but after being degassed. Lost grains yield an age older than the true cooling age of the grain. Inherited grains are determined by analyses that yield concentrations of both daughter and parent isotopes, but produce ages older (>10 Myr) than other grains for the same sample. The inherited grains are incorporated during eruption or during reworking of the volcanics shortly after deposition.

3.2 Zircon U-Pb geochronology

As ^{238}U, ^{235}U and ^{232}Th decay to their respective stable Pb isotopes, the concentrations of the various isotopes present can be utilized in age determinations that are based on the ratio of parent-daughter isotopes (Faure, 1998). Three geochronometric ages are determined using geochronometry equations, yielding ages corresponding to ratios of $^{206}Pb/^{238}U$, $^{207}Pb/^{235}U$, and $^{208}Pb/^{232}Th$. If the three age determinations agree with one another, they are said to be concordant; if the ages for the different decay chains disagree, they are said to be discordant (Faure, 1998; Davis et al., 2003). All ages presented in this manuscript are concordant ages, with the $^{206}Pb/^{238}U$ age interpreted as the crystallization age of the zircon and the age of intrusive activity.

The concentrations of U and Pb isotopes in a mineral can be determined from several techniques. This study utilizes the laser ablation inductively coupled plasma mass spectrometry technique (LA-ICP-MS). The first experiments that realized the potential

for U-Pb analysis on zircon by means of LA-ICP-MS were conducted in the early 1990's (Feng et al., 1993; Fryer et al., 1993). Since this time, extensive work has been done to refine the technique into the high precision analytical method presently utilized to determine crystallization ages for various minerals. In this dating technique, a laser ablation microprobe ablates a crystal face or polished surface of a zircon crystal, converting the solid into an aerosol that is transported to the ICP-MS by the carrier gas helium, where the concentrations of isotopes present is measured using a magnetic sector mass spectrometer. The Helix laser apparatus connected to an Element 2 ICP-MS was used for the U-Pb age determinations presented in this manuscript.

3.3 Geological and structural mapping

Two trips to the WHMCC focused exclusively on mapping the area and collecting samples from basin strata (Figures 4 and 5). Field mapping was started from June 2-20, 2011, and completed from March 11-22, 2012. A Panasonic toughbook computer was used as a mapping tablet, with the ArcGIS program utilized for mapping directly onto the computer. Digital orthophoto quadrangles (DOQ) were downloaded from The National Map Viewer offered by the United States Geological Survey (http://nationalmap.gov/viewer.html). DOQ are aerial photographs in which the image displacement due to camera tilts and terrain relief has been removed, resulting in a photographic image with the geometric constraints of a map with 1-meter ground resolution (USGS Fact Sheet, 2001). The DOQ were georeferenced in ArcGIS, creating a mosaic of DOQ as a map. A

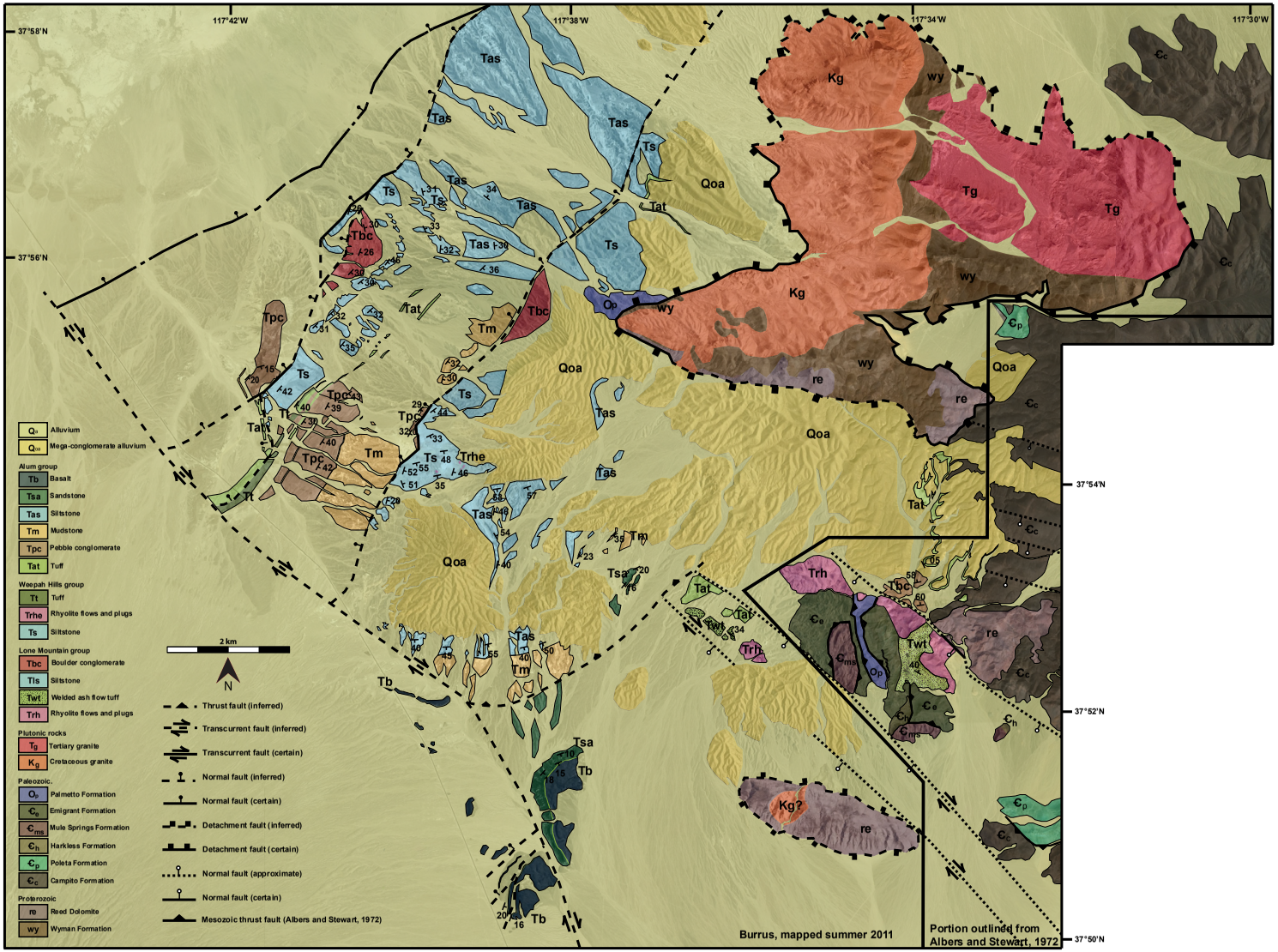

Figure 4: Geologic map of the Weepah Hills area. Detachment faulting exposes lower-plate granitic and meta-sedimentary rocks, while dextral transcurrent faults and high-angle normal faults dissect youner basin strata. Image is digital orthophoto from the U.S.G.S. National Map viewer (http://nationalmap.gov/viewer.html)

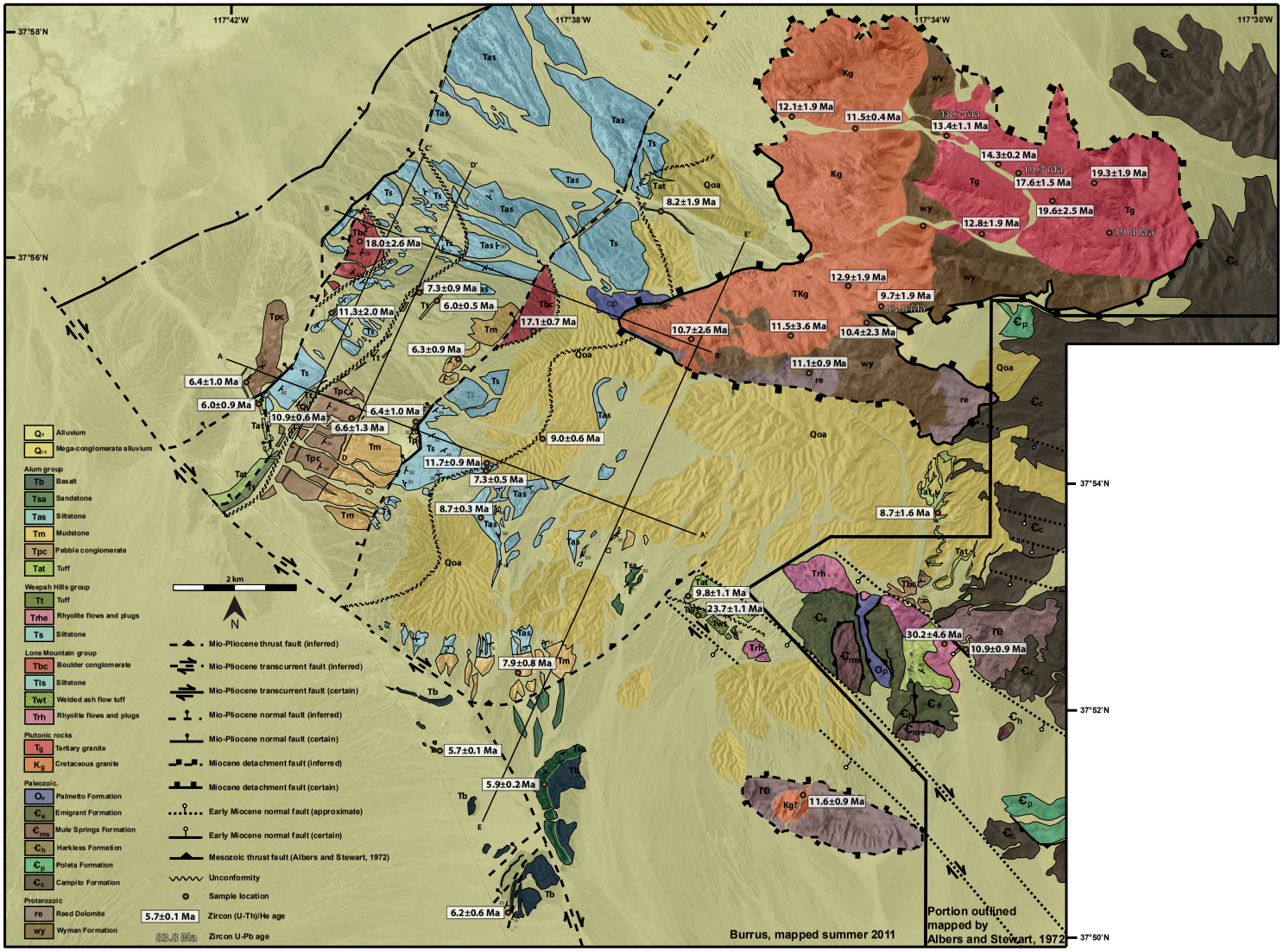

Figure 5: Interpretive geologic map of the Weepah Hills area with zircon U-Pb and zircon (U-Th)/He ages critical to interpretations displayed. Unconformities shown are interpreted based on ZHe cooling ages. Lines of cross-sections A-A', B-B', C-C', D-D' and E-E'are shown. Image is digital orthophoto from the U.S.G.S. National Map viewer (http://nationalmap.gov/viewer)

GPS built into the toughbook offered 3-meter horizontal resolution for fast and accurate coordinates for sample collection sites and field orientation.

4. RESULTS

4.1 GEOCHRONOLOGIC AND THERMOCHRONOMETRIC CONSTRAINTS ON PLUTONISM AND COOLING IN THE EXHUMED LOWER PLATE

25 samples were collected from the granitic rocks of the exhumed lower plate (Figure 6). ZHe was conducted on the entire suite of samples (Table 1), AHe was analyzed for 10 samples (Table 2), and zircon U-Pb ages were obtained for eight of the samples (Tables 3 and 4).

4.1.1 Zircon geochronology of plutonic rocks

At least 50 zircon grains were analyzed per sample using the LA-ICP-MS method to determine U-Pb crystallization ages. Zircons varying in size and compositional zoning properties were analyzed to ensure all populations were sampled. The U-Pb ages record two events of plutonism forming the granitic footwall of the WHMCC, a Late Cretaceous event at ~83 Ma and an early Miocene event at ~19 Ma (Figure 7). These ages divide the pluton, from north to south, into two temporally distinct halves. The western pluton is Late Cretaceous and the eastern pluton is Miocene. Earlier researchers speculated that the plutonism in the SPLM system may have been the product multiple magmatic events based on K-Ar ages of 67.2±3 Ma and 19.5±1 Ma on biotite from Lone Mountain (Schilling, 1965). The ages were interpreted to represent intrusive activity (Albers and Stewart, 1972), but K-Ar on biotite has since been shown to be a thermochronometer, not a geo-

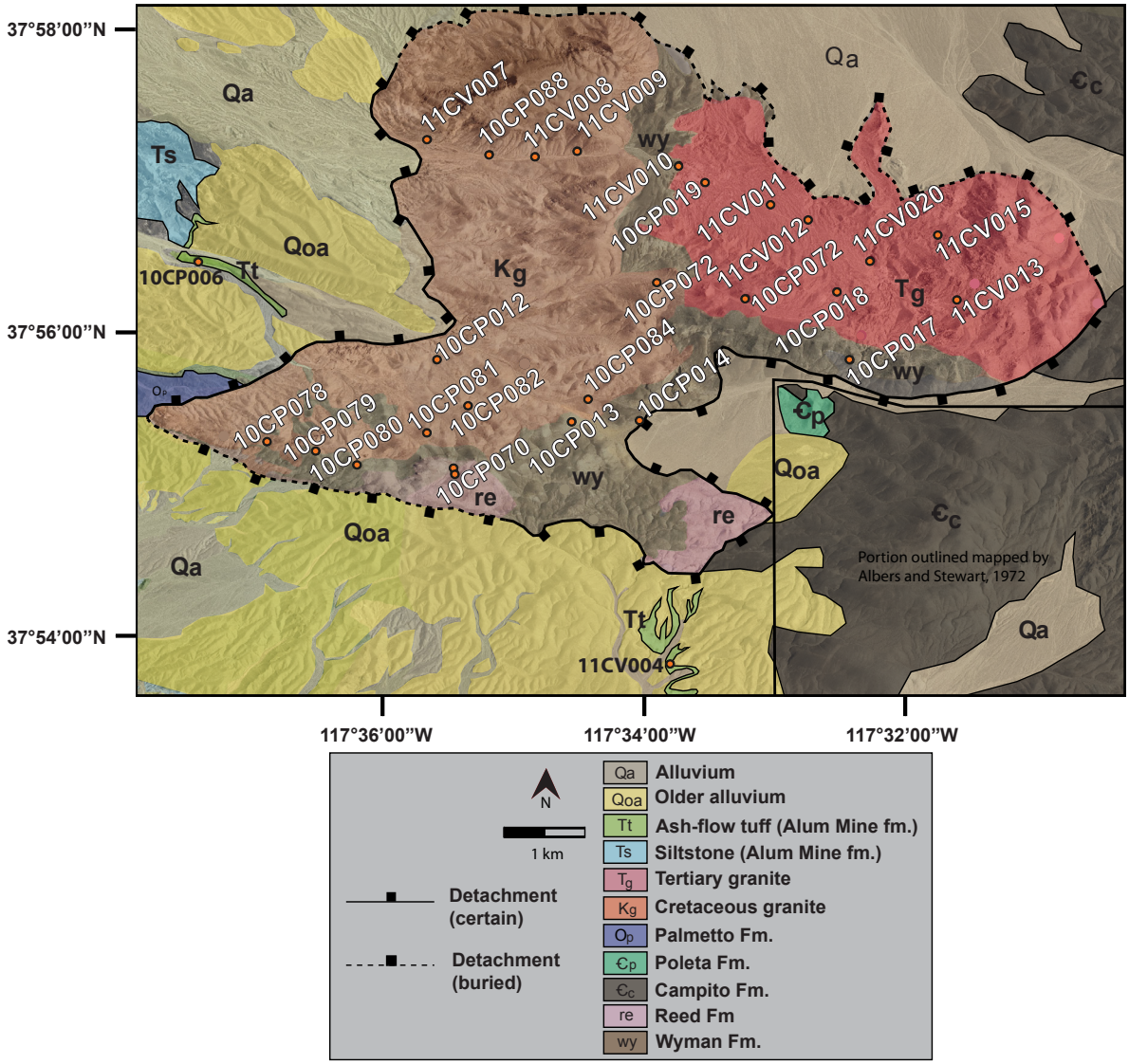

Figure 6: Sample locations from the lower plate plutonic rocks and upper plate tuffs near the detachment. Image is digital orthophoto from the U.S.G.S. National Map viewer (http://nationalmap.gov/viewer.html). The lower plate map for this figure is based on unpublished mapping done by Caleb Stroup of Ram Power Corp.

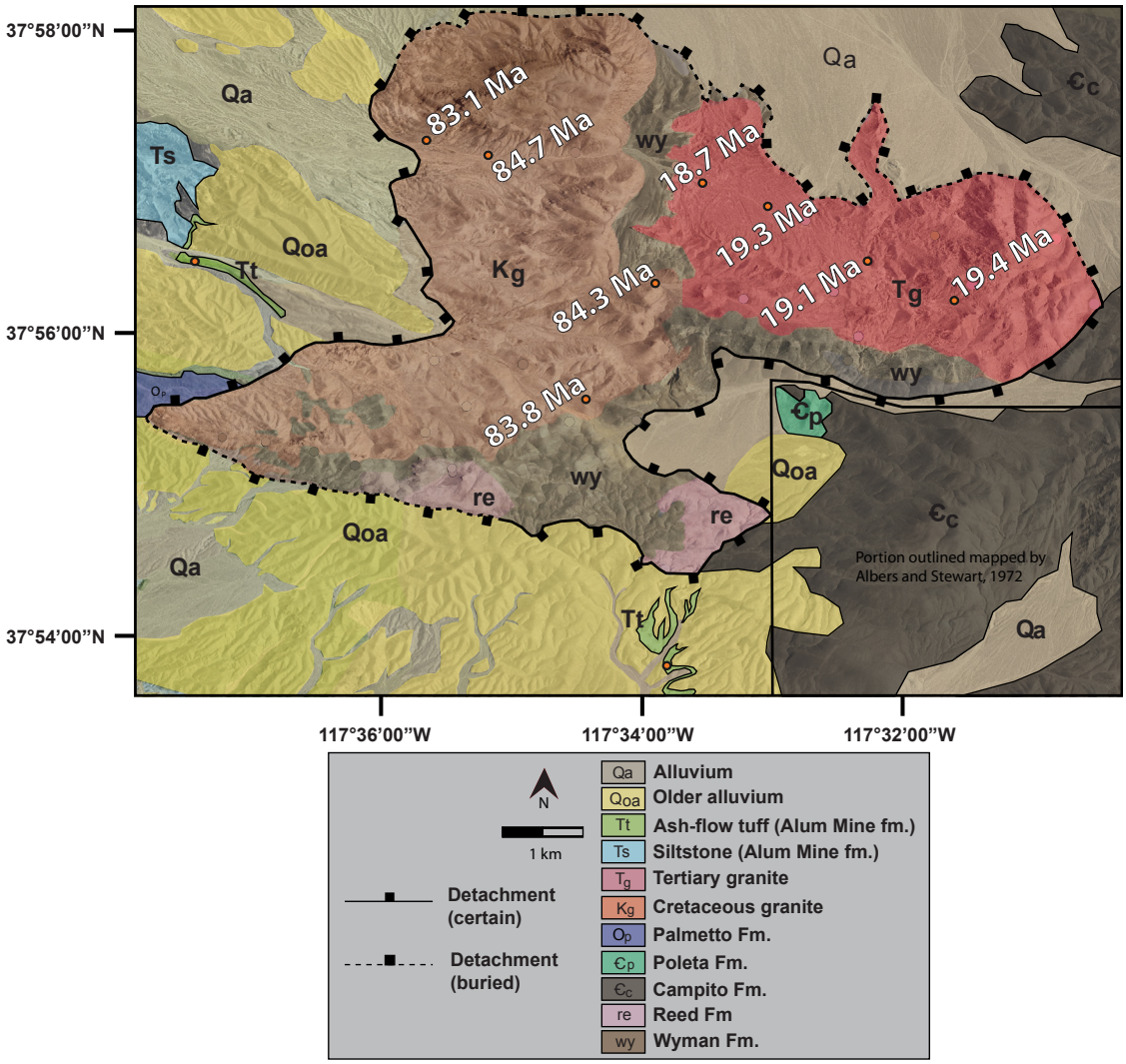

Figure 7: U-Pb data from the lower-plate of the Weepah Hills metamorphic core complex. Image is digital orthophoto from the U.S.G.S. National Map viewer (http://nationalmap.gov/viewer.html). The lower plate map for this figure is based on unpublished mapping done by Caleb Stroup of Ram Power Corp.

chronometer. Based on these facts, the U-Pb ages on zircon determined in this investigation are the first evidence of early Miocene magmatism in the SPLM extensional complex based on a widely accepted geochronometer.

Four samples from the WHMCC record Late Cretaceous plutonism, with a dominant population of ages between 83-85 Ma (Figure 7) (Table 4). The sample collected from the western-most edge of the pluton is the only sample that yielded zircons inherited from an earlier magmatic event. Concordant ages for inherited grains record zircon crystallization during Precambrian time, with three cores yielding ages of 2692±30 Ma, 2629±24 Ma, and 1866±16 Ma. These zircons are believed to have been incorporated from the partial melting of intruded meta-sedimentary rocks of Precambrian age (e.g. Wyman and Reed Formations) that are part of the lower plate of the WHMCC.

The transition between the temporally distinct halves of the WHCC is a north-south trending strip of the Wyman Formation (Figure 7). The granitic rocks east of this divide are early Miocene (~18-20 Ma). As for the western suite of samples, only one sample from the western edge of the transect records incorporation of older rock material. In this case two grains were found with U-Pb ages of 81.3±2.1 Ma and 81.5±1.2 Ma. The inherited zircons are incorporated by the partial melting of Late Cretateous pluton. Early Miocene plutonism was concurrent with the onset of large-magitude extension in the WHMCC. This discovery has implications for unraveling the tectonic evolution of the WHMCC. Tertiary extension across the western U.S. was commonly preceeded by significant igneous activity (Gans et al., 1989; Gans and Bohrson, 1998) and thus is often

Sample	206/238 Age (Ma)	error (Ma)	207/235	206/238	207/206	U (ppm)	Th (ppm)
11CV007-1	90.8	2.2	0.173	0.01418	0.0885	76.8	130
11CV007-2	1604	14	11.755	0.4812	0.1771	119.9	310
11CV007-3	654	16	0.1417	0.01427	0.0737	217	299
11CV007-4	1132	11	0.166	0.01683	0.0713	2290	180.4
11CV007-5	82.61	0.97	0.0966	0.01349	0.0527	26.4	26.29
11CV007-6	755	28	2.08	0.1893	0.07953	298	138.4
11CV007-7	866	11	2.831	0.2339	0.08805	132	86.3
11CV007-8	332.6	3.2	2.099	0.1932	0.0787	53.4	56.7
11CV007-9	2532	15	4.086	0.2826	0.1045	96.1	78.2
11CV007-10	91.3	1.3	0.0841	0.013	0.0469	122.9	78.4
11CV007-11	107.5	5.7	0.1103	0.01606	0.04977	900	242
11CV007-12	86.3	3.7	12.64	0.5038	0.1819	44.7	66
11CV007-13	1117.5	8.9	0.087	0.01315	0.0484	62.9	92
11CV007-14	1354.7	9	0.0859	0.0125	0.0507	592	342.8
11CV007-15	1138	15	12.96	0.5187	0.1816	58.9	43.5
11CV007-16	83.3	1.5	1.029	0.1069	0.0684	728	914
11CV007-17	102.7	4.7	0.1662	0.02439	0.0494	122.2	124.9
11CV007-18	2629	24	0.1087	0.01245	0.0634	447.2	700
11CV007-19	84.2	2.1	0.1655	0.01911	0.0632	131.4	103.3
11CV007-20	80	3.4	5.279	0.3346	0.1148	34.9	22.9
11CV007-21	2692	30	0.097	0.01436	0.0495	180	100.6
11CV007-22	155.3	2.6	2.073	0.1921	0.0784	45.7	18.87
11CV007-23	79.8	1.7	0.244	0.01452	0.1205	192	93
11CV007-24	122	4.6	3.499	0.2592	0.0978	63.6	40.3
11CV007-25	1862	16	0.0979	0.01369	0.0524	82.2	74.7
11CV007-26	91.9	1.9	0.079	0.01218	0.04777	760	133
11CV007-27	92.9	1.8	3.116	0.2512	0.08983	232.5	130.3
11CV007-28	1485	21	0.0861	0.0129	0.048	252.5	84.9
11CV007-29	87.6	2.1	3.403	0.2649	0.0929	113.1	106.4
11CV007-30	78	4.9	0.1114	0.01295	0.0631	81.7	110.5
11CV007-31	1444	13	14.1	0.1244	0.796	5.9	28.66
11CV007-32	1515	13	1.342	0.1439	0.06716	285	159
11CV007-33	82.9	1.9	0.3945	0.05294	0.05432	326	212

Table 1: Zircon U-Pb data from the Cretaceous granitic footwall of the WHMCC.

Sample	206/238 Age (Ma)	error (Ma)	207/235	207/206	206/238	U (ppm)	Th (ppm)
10CP088-1	83.1	1.4	0.0844	0.01298	0.0461	181	60.6
10CP088-2	87.8	1.9	0.0897	0.01371	0.0478	240	161
10CP088-3	87.8	2	0.0907	0.01372	0.0479	143	128.7
10CP088-4	81.09	0.98	0.0841	0.01266	0.04824	3604	1062
10CP088-5	86.5	2.7	0.0895	0.01352	0.048	554	41.7
10CP088-6	93.1	3	0.0936	0.01454	0.0475	151	68
10CP088-7	89.9	3.2	0.0942	0.01405	0.0492	109	89
10CP088-8	84.2	3.4	0.0908	0.01316	0.0522	39.9	32.89
10CP088-9	91.9	3.3	0.232	0.01435	0.112	145	51.6
10CP088-10	82.5	1.4	0.084	0.01288	0.04761	1430	261
10CP088-11	87.2	2.3	0.0908	0.01361	0.0496	99.8	48.3
10CP088-12	84.8	3.2	0.0884	0.01325	0.0487	470	213
10CP088-13	85	1.5	0.0848	0.01328	0.0462	205	94
10CP088-14	87.4	3.1	0.0928	0.01365	0.0501	135	54
10CP088-15	78.6	1.4	0.1009	0.01227	0.0588	584	188
10CP088-16	84.7	2.1	0.0891	0.01323	0.049	91.6	85.6
10CP088-17	84.7	1.4	0.0874	0.01323	0.0474	127.4	96.3
10CP088-18	89	3.7	0.091	0.01391	0.0478	86.3	106.4
10CP088-19	83.1	1.4	0.0855	0.01297	0.0482	155.2	93.5
10CP088-20	81.8	2.6	0.0875	0.01277	0.049	959	681
10CP088-21	76.8	1.1	0.0797	0.01199	0.0482	687	177
10CP088-22	78.8	1.2	0.081	0.0123	0.0481	404	127
10CP088-23	76.1	1	0.0781	0.01187	0.0475	753	307
10CP088-24	75.3	1.7	0.0766	0.01176	0.0475	874	291
10CP088-25	88.8	2.7	0.0897	0.01387	0.0479	328	53.2
10CP088-26	77.2	1.7	0.0808	0.01205	0.0491	714	185.6
10CP088-27	84	1.3	0.0843	0.01311	0.04756	809	595
10CP088-28	78.8	1.8	0.0867	0.01229	0.0517	115.9	75.6
10CP088-29	83.3	2.3	0.0908	0.013	0.0513	567	286
10CP088-30	83.7	1.8	0.0818	0.01307	0.0459	169	45.6
10CP088-31	90	3.5	0.193	0.01406	0.101	207	80.9
10CP088-32	84.4	1.5	0.0947	0.01318	0.052	262.8	174

Table 1 continued: Zircon U-Pb data from the Cretaceous granitic footwall of the WHMCC

Sample	206/238 Age (Ma)	error (Ma)	207/235	207/206	206/238	U (ppm)	Th (ppm)
10CP088-33	85.3	2.1	0.177	0.01332	0.104	1270	1390
10CP088-34	92	1.7	0.0971	0.01437	0.049	162	106
10CP088-35	85.6	2.2	0.0907	0.01336	0.0493	80.5	83.2
10CP088-36	79.9	2.5	0.0825	0.01247	0.0478	450	231
10CP088-37	90.9	2.4	0.144	0.01421	0.0728	202	35.2
10CP088-38	84.9	1.9	0.0871	0.01326	0.0469	204	100
10CP088-39	85.1	2	0.088	0.01329	0.0487	179	98
10CP088-40	81	1.1	0.0843	0.01264	0.0489	434	144
10CP088-41	81.9	1.9	0.084	0.01279	0.047	312.1	219
10CP088-42	82.28	0.8	0.084	0.01284	0.04795	1027	208
10CP088-43	79.9	2	0.0839	0.01247	0.0501	310	166
10CP088-44	86.3	1.6	0.088	0.01348	0.0462	85.1	27.6
10CP088-45	79.76	0.74	0.08211	0.01245	0.04834	1268	377
10CP088-46	84.4	2.3	0.0854	0.01318	0.0471	1040	151
10CP088-47	81.9	1.2	0.0838	0.01278	0.04729	590	148
10CP088-48	85	1.2	0.0869	0.01328	0.04775	224	102.7
10CP088-49	85.6	1	0.0849	0.01337	0.04611	297	116.8
10CP088-50	88.7	1.7	0.1117	0.01386	0.0586	302	168
10CP088-51	82.1	0.91	0.0849	0.01282	0.04822	712	163
10CP088-52	87.4	1.6	0.0897	0.01365	0.04798	660	261
10CP088-53	80.5	0.81	0.08198	0.01257	0.04759	2030	1160
10CP088-54	79.94	0.96	0.0818	0.01248	0.04788	1761	149.9
10CP088-55	80.33	0.96	0.0817	0.01254	0.04762	1390	452
10CP088-56	86.9	1.1	0.0889	0.01357	0.0472	339	190
10CP088-57	81.1	1.3	0.0833	0.01266	0.04827	1820	610
10CP088-58	85.1	1.3	0.0881	0.0133	0.0474	374	148
10CP088-59	83.4	1.1	0.0857	0.01303	0.04768	609	263
10CP088-60	82.4	0.71	0.08377	0.01286	0.04714	736	139
10CP088-61	88.7	2.7	0.0899	0.01386	0.0465	262	133
10CP088-62	81.24	0.69	0.0832	0.01268	0.04782	687	295
10CP088-63	88.4	1.5	0.0901	0.01381	0.04758	668	276.2

Table 1 continued: Zircon U-Pb data from the Cretaceous granitic footwall of the WHMCC

Sample	206/238 Age (Ma)	error (Ma)	207/235	207/206	206/238	U (ppm)	Th (ppm)
10CP084-1	77.8	1.4	0.0808	0.01214	0.0482	663	96.2
10CP084-2	75.9	1.5	0.0819	0.01185	0.0498	186.2	82.2
10CP084-3	77.6	1.4	0.1052	0.0121	0.0616	297	682
10CP084-4	80.3	1.4	0.0843	0.01253	0.0486	539	612
10CP084-5	79.5	2.5	0.105	0.01242	0.0591	357	227
10CP084-6	88.5	2.6	0.0959	0.01382	0.0501	459	201
10CP084-7	83.5	3.8	0.0826	0.01304	0.0473	84.8	91
10CP084-8	81	1.5	0.0852	0.01264	0.0494	380	92.4
10CP084-9	97.4	2.4	0.1024	0.01523	0.0476	307	224.8
10CP084-10	75.6	2.4	0.0769	0.01179	0.0472	760	197
10CP084-11	83.5	1.6	0.092	0.01303	0.0511	177	113.9
10CP084-12	80.9	1.7	0.0857	0.01263	0.0485	111	76.5
10CP084-13	83.8	2	0.0848	0.01309	0.0478	107	137.4
10CP084-14	94.7	2.2	0.0933	0.01479	0.0468	194	146
10CP084-15	93.7	6	0.0931	0.01465	0.0466	440	238
10CP084-16	83.2	2.8	0.157	0.01299	0.0905	94	129.8
10CP084-17	76.3	2.2	0.0834	0.01191	0.0526	200	198
10CP084-18	78.1	2.5	0.0839	0.01219	0.0502	227	374
10CP084-19	91.5	3.2	0.0942	0.0143	0.0479	211	131
10CP084-20	80.6	1.5	0.084	0.01258	0.0489	465	197
10CP084-21	80.8	2.3	0.0856	0.01262	0.0495	837	707
10CP084-22	78.4	1.6	0.0807	0.01224	0.0478	812	583
10CP084-23	89.3	1.7	0.0919	0.01395	0.0484	242	257
10CP084-24	76.7	2.2	0.0872	0.01197	0.0519	70	64
10CP084-25	78.6	1	0.084	0.01227	0.0495	336	106.2
10CP084-26	86.1	1.5	0.0885	0.01345	0.048	519	310
10CP084-27	85.9	2.2	0.1006	0.01342	0.0549	142.6	265
10CP084-28	84	1.9	0.0975	0.01312	0.0558	462	432
10CP084-29	85.9	2.2	0.0907	0.01341	0.0484	140	129
10CP084-30	82.3	2.1	0.1058	0.01286	0.0594	151.1	186
10CP084-31	85.2	1.9	0.087	0.01331	0.047	151	74.5
10CP084-32	78.72	0.94	0.087	0.01229	0.0508	514	151

Table 1 continued: Zircon U-Pb data from the Cretaceous granitic footwall of the WHMCC

Sample	206/238 Age (Ma)	error (Ma)	207/235	207/206	206/238	U (ppm)	Th (ppm)
10CP084-33	93.1	2.5	0.0965	0.01454	0.0491	192	128.2
10CP084-34	88.8	2.7	0.159	0.01388	0.0839	102.2	112.6
10CP084-35	83.7	4.4	0.159	0.01308	0.0717	677	296
10CP084-36	87.7	1.8	0.0941	0.01369	0.0504	191	250
10CP084-37	73.1	1.6	0.0939	0.01141	0.061	127	44
10CP084-38	83.3	1.6	0.0851	0.013	0.0478	260	102.6
10CP084-39	84.3	2.1	0.1017	0.01316	0.0542	218	310
10CP084-40	80.5	2.8	0.0876	0.01257	0.0507	224	190
10CP084-41	80.9	1.2	0.0844	0.01263	0.0484	309.2	474
10CP084-42	81	1.4	0.0834	0.01265	0.0479	603	286
10CP084-43	83.4	1.5	0.0909	0.01302	0.0518	165.6	272.4
10CP084-44	81	2	0.0843	0.01264	0.048	861	270
10CP084-45	84.6	1.2	0.0925	0.01322	0.0505	765	457
10CP084-46	117.8	5.2	0.117	0.01845	0.0462	118	32.1
10CP084-47	80.3	9.3	0.093	0.0125	0.0541	1310	253

Table 1 continued: Zircon U-Pb data from the Cretaceous granitic footwall of the WHMCC

Sample	206/238 Age (Ma)	error (Ma)	207/235	207/206	206/238	U (ppm)	Th (ppm)
10CP086-1	77.1	2	0.0811	0.01203	0.0484	660	111.6
10CP086-2	78.2	1.5	0.0811	0.01221	0.0485	478	149.6
10CP086-3	78.3	1.8	0.0828	0.01222	0.0503	91.1	57.7
10CP086-4	79.7	1.3	0.0825	0.01243	0.0482	594	175.7
10CP086-5	80.5	1.2	0.0842	0.01257	0.0484	404	749
10CP086-6	82.1	2.4	0.0982	0.01282	0.0549	74.1	83.7
10CP086-7	82.1	1.2	0.0852	0.01281	0.0485	412	265
10CP086-8	82.2	3.6	0.0919	0.01283	0.0511	38.7	69.9
10CP086-9	82.4	1.7	0.0852	0.01287	0.0469	448	143
10CP086-10	82.9	2.9	0.0936	0.01294	0.0519	63.8	93
10CP086-11	83.2	1.4	0.0893	0.013	0.0499	168	110
10CP086-12	83.3	2	0.0886	0.01301	0.0489	159.8	207
10CP086-13	83.4	1.5	0.0875	0.01302	0.0487	178.4	225
10CP086-14	83.4	1.7	0.0855	0.01303	0.0476	136.3	173
10CP086-15	83.9	1.4	0.0884	0.01309	0.0496	205.3	148
10CP086-16	84	1.6	0.0873	0.01312	0.0481	168	230
10CP086-17	84	2.7	0.0894	0.01311	0.0499	481	308.4
10CP086-18	84.6	1.7	0.0899	0.01321	0.0502	127.4	173
10CP086-19	84.7	2.1	0.0917	0.01323	0.0512	136.3	87.1
10CP086-20	84.9	1.6	0.0884	0.01326	0.0479	152.1	77.1
10CP086-21	85.1	2.3	0.0885	0.01329	0.0488	600	155
10CP086-22	85.3	1.4	0.0878	0.01332	0.0481	291	135
10CP086-23	85.5	2.6	0.0888	0.01335	0.0483	85.1	86
10CP086-24	85.6	2.5	0.086	0.01337	0.0476	75.1	88.2
10CP086-25	85.6	2.3	0.0939	0.01336	0.0498	153.8	191
10CP086-26	85.7	2.6	0.0963	0.01338	0.0514	404	132
10CP086-27	86	2.8	0.0929	0.01343	0.0505	160	64
10CP086-28	86.2	1.6	0.0831	0.01346	0.0457	155.1	90.9
10CP086-29	86.3	2.1	0.0888	0.01347	0.0491	98	74.9
10CP086-30	86.3	1.2	0.0868	0.01348	0.0478	391	183.5
10CP086-31	87	2.9	0.0901	0.01358	0.0482	281	99
10CP086-32	87.3	2.8	0.0889	0.01364	0.0468	412	225.2

Table 1 continued: Zircon U-Pb data from the Cretaceous granitic footwall of the WHMCC

Sample	206/238 Age (Ma)	error (Ma)	207/235	207/206	206/238	U (ppm)	Th (ppm)
10CP086-33	87.6	1.6	0.0914	0.01368	0.0484	518	185
10CP086-34	88.6	1.8	0.0926	0.01385	0.0484	549.2	296.7
10CP086-35	89.8	3	0.0888	0.01403	0.0471	107	62.3
10CP086-36	90.4	1.5	0.0967	0.01413	0.0497	223	111.8
10CP086-37	93	2.2	0.1176	0.01453	0.0594	155	166
10CP086-38	93.3	1.8	0.097	0.01459	0.0491	440	348
10CP086-39	94.3	1.6	0.098	0.01474	0.0485	393	49.1
10CP086-40	98.4	3	0.1009	0.01538	0.0486	110	114.8
10CP086-41	112.7	3.5	0.1195	0.01764	0.0494	500	395
10CP086-42	157.6	2	0.1676	0.02476	0.0494	1025	131.6

Table 1 continued: Zircon U-Pb data from the Cretaceous granitic footwall of the WHMCC

Sample	206/238 Age (Ma)	error (Ma)	207/235	207/206	206/238	U (ppm)	Th (ppm)
10CP019-1	17.28	0.45	0.01961	0.002684	0.0542	548	1030
10CP019-2	22.4	1.4	0.101	0.00348	0.189	436	330
10CP019-3	19.56	0.32	0.02152	0.003039	0.0521	405	1064
10CP019-4	19.71	0.41	0.0391	0.003062	0.0927	409	553
10CP019-5	18.21	0.43	0.01824	0.002829	0.0466	510	1313
10CP019-6	18.4	0.98	0.0187	0.00286	0.0488	770	269
10CP019-7	22.2	0.83	0.0236	0.00345	0.0516	552	3870
10CP019-8	18.62	0.36	0.0248	0.002893	0.0618	466.2	527.1
10CP019-9	18.82	0.43	0.029	0.002924	0.0721	326	757
10CP019-10	17.31	0.36	0.0206	0.002689	0.0559	575	1673
10CP019-11	19.01	0.73	0.0252	0.00295	0.0599	120.7	268
10CP019-12	18.12	0.32	0.02158	0.002815	0.0552	517.2	960
10CP019-13	18.36	0.47	0.0189	0.002852	0.0472	256.3	304.6
10CP019-14	18.76	0.35	0.0197	0.002915	0.0496	405	410.5
10CP019-15	17.43	0.68	0.01791	0.00271	0.0474	547	521
10CP019-16	19.21	0.62	0.0242	0.002985	0.0599	117.5	188.2
10CP019-17	21.78	0.61	0.0432	0.003385	0.0922	384.6	454.6
10CP019-18	21.74	0.48	0.06	0.003378	0.1288	265	397
10CP019-19	20.78	0.77	0.0215	0.00323	0.0481	156.1	331.1
10CP019-20	19.76	0.6	0.0197	0.003071	0.0468	171.5	312.5
10CP019-21	21.87	0.36	0.02622	0.003398	0.0557	536	738
10CP019-22	18.66	0.4	0.01931	0.002899	0.0479	435	593
10CP019-23	18.02	0.32	0.01858	0.002799	0.0476	678	431
10CP019-24	18.3	1.2	0.0422	0.00284	0.1087	810	5.20E+03
10CP019-25	19.56	0.47	0.0197	0.003039	0.0472	437	498
10CP019-26	18.66	0.32	0.02053	0.002898	0.0518	960	1200
10CP019-27	17.82	0.35	0.01954	0.002768	0.0518	986	1920
10CP019-28	19.08	0.39	0.02006	0.002964	0.05	619	752
10CP019-29	17.57	0.31	0.01765	0.002729	0.0471	1404	2430
10CP019-30	18.73	0.37	0.01889	0.00291	0.0473	632	452
10CP019-31	75.7	0.8	0.07914	0.01179	0.04868	1327	606
10CP019-32	81.3	2.1	0.0843	0.0127	0.0483	750	259

Table 2: Zircon U-Pb data from the Miocene granitic footwall of the WHMCC

Sample	206/238 Age (Ma)	error (Ma)	207/235	207/206	206/238	U (ppm)	Th (ppm)
10CP019-33	17.65	0.28	0.01888	0.002741	0.0502	1847	4260
10CP019-34	18.63	0.46	0.01986	0.002894	0.0498	887	1110
10CP019-35	25.06	0.59	0.0543	0.003895	0.1014	246	243
10CP019-36	19.18	0.44	0.0316	0.00298	0.0764	636	1300
10CP019-37	18.84	0.35	0.0189	0.002927	0.0469	304	407
10CP019-38	18.23	0.41	0.02164	0.002832	0.0537	1186	3320
10CP019-39	20.84	0.57	0.0318	0.003239	0.0691	499	789
10CP019-40	19.43	0.43	0.02	0.003019	0.0478	342	269
10CP019-41	20.9	1.1	0.061	0.00325	0.113	708	760
10CP019-42	17.62	0.22	0.01902	0.002738	0.0505	1999	524
10CP019-43	17.24	0.2	0.01766	0.002678	0.0478	1290	2215
10CP019-44	18.67	0.29	0.01988	0.0029	0.0492	1100	920
10CP019-45	19.72	0.39	0.01985	0.003064	0.0466	338	454
10CP019-46	20.02	0.51	0.0282	0.00311	0.0645	231	206
10CP019-47	81.5	1.2	0.0933	0.01272	0.053	226	156.3
10CP019-48	19.44	0.5	0.0249	0.003019	0.0589	479	243
10CP019-49	19.94	0.57	0.0245	0.003098	0.0553	583	624
10CP019-50	18.96	0.44	0.0234	0.002945	0.0573	456	358
10CP019-51	18.14	0.34	0.01876	0.002817	0.0486	842	686
10CP019-52	18.77	0.42	0.0194	0.002915	0.0487	880	1180
10CP019-53	19.9	0.63	0.0264	0.003092	0.0599	880	1310
10CP019-54	17.27	0.28	0.01754	0.002683	0.0471	1263	1510
10CP019-55	22.7	0.81	0.0981	0.00353	0.199	237	315

Table 2 continued: Zircon U-Pb data from the Miocene granitic footwall of the WHMCC.

Sample	206/238 Age (Ma)	error (Ma)	207/235	207/206	206/238	U (ppm)	Th (ppm)
11CV020-1	18.37	0.48	0.02107	0.002855	0.0543	369	364
11CV020-2	18.48	0.48	0.0193	0.002871	0.049	525	422
11CV020-3	20.12	0.53	0.0196	0.003126	0.0458	257	323
11CV020-4	18.34	0.5	0.0199	0.002848	0.0515	237.3	412
11CV020-5	16.48	0.76	0.01605	0.00256	0.0473	751	526
11CV020-6	18.35	0.55	0.01977	0.00285	0.0513	550	497
11CV020-7	19.21	0.51	0.01837	0.002985	0.0458	452	369
11CV020-8	18.57	0.33	0.01834	0.002885	0.047	560	440
11CV020-9	19.48	0.54	0.0189	0.003027	0.045	248	280
11CV020-10	19.2	0.56	0.01858	0.002983	0.0456	494	348
11CV020-11	19.44	0.54	0.0275	0.00302	0.0653	387.5	461
11CV020-12	19.16	0.48	0.01884	0.002977	0.0467	459	354
11CV020-13	18.82	0.43	0.02003	0.002924	0.0501	415	644
11CV020-14	19.47	0.62	0.0219	0.003024	0.0528	285	322
11CV020-15	19.31	0.42	0.0192	0.003	0.0458	236	383
11CV020-16	19.28	0.36	0.01995	0.002995	0.0489	542	700
11CV020-17	18.66	0.33	0.01866	0.002899	0.0476	479	429
11CV020-18	17.6	0.53	0.01821	0.002734	0.0497	641	598
11CV020-19	19.36	0.41	0.0206	0.003008	0.05	669	1230
11CV020-20	19.15	0.5	0.01915	0.002976	0.0476	450	572
11CV020-21	19.89	0.45	0.0222	0.003091	0.0524	440	394
11CV020-22	19.06	0.45	0.01955	0.002961	0.0476	393	412
11CV020-23	20.15	0.37	0.0273	0.003131	0.0615	596	1140
11CV020-24	18.73	0.25	0.0316	0.002909	0.0795	1220	2140
11CV020-25	19.01	0.55	0.0197	0.002953	0.0491	352	255.3
11CV020-26	18.9	0.32	0.0195	0.002936	0.0483	816	642
11CV020-27	18.2	0.61	0.0232	0.002827	0.0568	761	753
11CV020-28	21	1.4	0.0211	0.00327	0.0452	50.8	68
11CV020-29	16.44	0.5	0.0191	0.002554	0.0539	352	257
11CV020-30	20.07	0.65	0.042	0.00312	0.1	123	157
11CV020-31	18.88	0.44	0.0232	0.002932	0.0579	622	740
11CV020-32	18.25	0.44	0.01863	0.002835	0.0481	586	972

Table 2 continued: Zircon U-Pb data from the Miocene granitic footwall of the WHMCC.

Sample	206/238 Age (Ma)	error (Ma)	207/235	207/206	206/238	U (ppm)	Th (ppm)
11CV020-33	19.06	0.48	0.0191	0.002961	0.0493	690	172
11CV020-34	17.04	0.53	0.0197	0.002647	0.0552	626	698
11CV020-35	19.15	0.41	0.0211	0.002975	0.0514	398	297
11CV020-36	18.02	0.43	0.01819	0.002799	0.0469	731	1200
11CV020-37	20.12	0.45	0.0288	0.003126	0.067	499	725
11CV020-38	19.45	0.67	0.0199	0.00302	0.0484	264	346
11CV020-39	18.13	0.2	0.01878	0.002816	0.0484	1132	1120
11CV020-40	18.55	0.42	0.02048	0.002882	0.0512	634	1022
11CV020-41	18.47	0.22	0.02168	0.002869	0.0546	3390	4000
11CV020-42	20.66	0.76	0.0373	0.00321	0.082	513	588
11CV020-43	19.47	0.77	0.0214	0.00303	0.0523	327.1	489
11CV020-44	17.53	0.23	0.0221	0.002722	0.0585	1891	2390
11CV020-45	17.87	0.32	0.0251	0.002777	0.0649	1663	2510
11CV020-46	18.15	0.34	0.01876	0.00282	0.0487	684	870
11CV020-47	17.32	0.22	0.0188	0.002691	0.0509	1187	1036
11CV020-48	18.72	0.49	0.02	0.002909	0.0498	473	522
11CV020-49	18.5	0.31	0.0199	0.002874	0.0499	1194	1218
11CV020-50	19.36	0.49	0.0354	0.003008	0.0837	707	1880
11CV020-51	18.41	0.31	0.01885	0.002861	0.0482	750	506
11CV020-52	18.95	0.65	0.0193	0.00294	0.0475	325	432
11CV020-53	19.83	0.65	0.0277	0.00308	0.0643	447	337
11CV020-54	18.7	0.37	0.01849	0.002905	0.0468	384	352
11CV020-55	17.81	0.17	0.01796	0.002767	0.04682		1.08E+04
11CV020-56	19.78	0.62	0.0259	0.003074	0.0619	264	224
11CV020-57	20.87	0.49	0.0254	0.003243	0.0575	171	172
11CV020-58	18.53	0.21	0.01864	0.002879	0.04732		5100
11CV020-59	18.84	0.47	0.01845	0.002927	0.0469	556	1001
11CV020-60	18.61	0.5	0.01835	0.002891	0.0465	321	332
11CV020-61	18.95	0.43	0.02016	0.002945	0.0502	471	400

Table 2 continued: Zircon U-Pb data from the Miocene granitic footwall of the WHMCC.

Sample	206/238 Age (Ma)	error (Ma)	207/235	207/206	206/238	U (ppm)	Th (ppm)
11CV11-1	19.74	0.48	0.0204	0.003066	0.0483	202	219
11CV11-2	19.33	0.38	0.02043	0.003004	0.0488	523	350
11CV11-3	18.37	0.35	0.02014	0.002854	0.0498	1480	1560
11CV11-4	19.63	0.5	0.01922	0.00305	0.0461	427	347
11CV11-5	20.1	0.57	0.0217	0.003123	0.0508	251	179
11CV11-6	19.95	0.31	0.02201	0.0031	0.0518	731	1590
11CV11-7	18.75	0.38	0.0263	0.002912	0.0642	711	938
11CV11-8	20.4	0.43	0.0219	0.003169	0.0508	576	620
11CV11-9	20	0.47	0.02067	0.003097	0.0483	325	274
11CV11-10	20.78	0.4	0.02041	0.003229	0.0458	432	406
11CV11-11	19.88	0.29	0.01997	0.003089	0.0468	770	890
11CV11-12	19.91	0.33	0.0262	0.003094	0.0618	770	496
11CV11-13	20.76	0.56	0.0263	0.003225	0.0588	358	224.3
11CV11-14	19.38	0.39	0.01926	0.003011	0.0463	481	392
11CV11-15	19.1	0.34	0.01931	0.002968	0.0483	521	365
11CV11-16	19.32	0.3	0.02104	0.003001	0.0509	754	539
11CV11-17	20.86	0.46	0.0221	0.003241	0.0506	284	627
11CV11-18	20.27	0.49	0.0258	0.003149	0.0603	362	434
11CV11-19	19.25	0.3	0.01946	0.00299	0.0471	1000	835
11CV11-20	19.16	0.39	0.01884	0.002977	0.0463	485	472
11CV11-21	20.11	0.37	0.0232	0.003124	0.0535	574	611
11CV11-22	19.59	0.32	0.01973	0.003043	0.0472	608	427
11CV11-23	19.16	0.4	0.02086	0.002977	0.0508	674	618
11CV11-24	19.39	0.29	0.0239	0.003013	0.0583	641	581
11CV11-25	19.92	0.43	0.02058	0.003095	0.049	670	664
11CV11-26	19.72	0.32	0.02044	0.003064	0.0481	687	471
11CV11-27	21.18	0.59	0.0216	0.003292	0.0511	191	264
11CV11-28	19.38	0.56	0.0229	0.003011	0.0541	229	145
11CV11-29	19.85	0.38	0.0216	0.003084	0.0494	1570	1590
11CV11-30	19.25	0.55	0.019	0.003093081	0.0466	178	280

Table 2 continued: Zircon U-Pb data from the Miocene granitic footwall of the WHMCC.

Sample	206/238 Age (Ma)	error (Ma)	207/235	207/206	206/238	U (ppm)	Th (ppm)
11CV13-1	20.4	0.6	0.0193	0.00317	0.0439	237	414
11CV13-2	19.29	0.4	0.02046	0.002996	0.05	382	281
11CV13-3	20.46	0.53	0.02129	0.003179	0.048	503	620
11CV13-4	20.2	0.47	0.02066	0.003139	0.048	416	389
11CV13-5	19.13	0.5	0.0226	0.002972	0.0544	930	680
11CV13-6	19.84	0.57	0.0196	0.003083	0.0466	186	128.5
11CV13-7	19.11	0.43	0.01891	0.002969	0.0465	452	396
11CV13-8	19.51	0.44	0.02104	0.003031	0.0495	314	476
11CV13-9	19.51	0.36	0.01908	0.003031	0.0455	505	352
11CV13-10	19.06	0.46	0.01867	0.002961	0.0459	281	247
11CV13-11	20.41	0.52	0.0325	0.003172	0.0703	299	355
11CV13-12	19.45	0.34	0.01959	0.003022	0.0461	567	646
11CV13-13	19.31	0.62	0.02	0.003	0.0475	196.1	267
11CV13-14	19.55	0.57	0.0199	0.003038	0.0473	271	249
11CV13-15	20.24	0.58	0.021	0.003145	0.0479	229	393
11CV13-16	18.84	0.36	0.01882	0.002927	0.0472	415	325
11CV13-17	21.14	0.71	0.039	0.00328	0.0854	430	342
11CV13-18	18.94	0.4	0.02008	0.002942	0.0497	937	843
11CV13-19	18.97	0.4	0.01963	0.002947	0.0475	419	441
11CV13-20	19.66	0.73	0.0213	0.00305	0.051	209	382
11CV13-21	19.59	0.46	0.022	0.003044	0.0516	330	325
11CV13-22	19.81	0.59	0.0195	0.003077	0.0466	297	349
11CV13-23	17.02	0.27	0.01975	0.002643	0.054	1640	4620
11CV13-24	21.04	0.53	0.0214	0.003269	0.0474	298	223
11CV13-25	18.98	0.41	0.01944	0.002949	0.0474	294	257
11CV13-26	19.56	0.43	0.01946	0.003038	0.0458	386	347
11CV13-27	19.63	0.62	0.0195	0.00305	0.0472	164	258
11CV13-28	19.41	0.37	0.0204	0.003016	0.0489	345	419
11CV13-29	20.27	0.48	0.0204	0.00315	0.0474	394	466
11CV13-30	20.36	0.51	0.0239	0.003164	0.0552	299	191

Table 2 continued: Zircon U-Pb data from the Miocene granitic footwall of the WHMCC.

spatially and temporally linked to the development of accommodation zones between extended terrains (Axen et al., 1998; Faulds and Varga, 1998; Stewart, 1998). The relationship between extension and Miocene arc volcanism (e.g., Christiansen et al., 1992) immediately preceded middle Miocene extension (e.g., Dilles and Gans, 1995; Stockli et al., 2002; Surpless et al., 2002), and spatially overlaps strike- and oblique slip transfer zones (Stewart, 1998).

4.1.2 Zircon and apatite thermochronology of plutonic rocks

The ZHe ages for 25 granitic samples of the Weepah Hills range from 22.5±0.9 Ma to 9.1±0.1 Ma (Figure 8). The ZHe ages are based on the average of 2-4 aliquots (depending on sample), with 1σ error calculated (Table 1). ZHe cooling ages represent the cooling of the plutonic rocks below ~180˚C, correlating to exhumation above ~6 km. In the northern-most transect, ages progressive increase from west to east, from 12.1±1.9 Ma to 19.3±1.9 Ma (Figure 8). To the south, no discernable trend can be identified in the ZHe data. Adjacent samples have ages that vary by as much as 10 Ma, and single samples have the reported error much higher than for the northern transect. The varied ages reported between aliquots from a single sample may be a result of complex zoning identified by CL imaging of three samples. During U-Pb analysis, high ^{238}U rims were detected from concentration depth profiles. The standard deviation is high for some of the ZHe ages, but the upper and lower age limits for cooling of the pluton are well determined.

Ten AHe ages range from 8.1±1.5 to 12.4±1.1 Ma (Figure 9; Table 2), with an

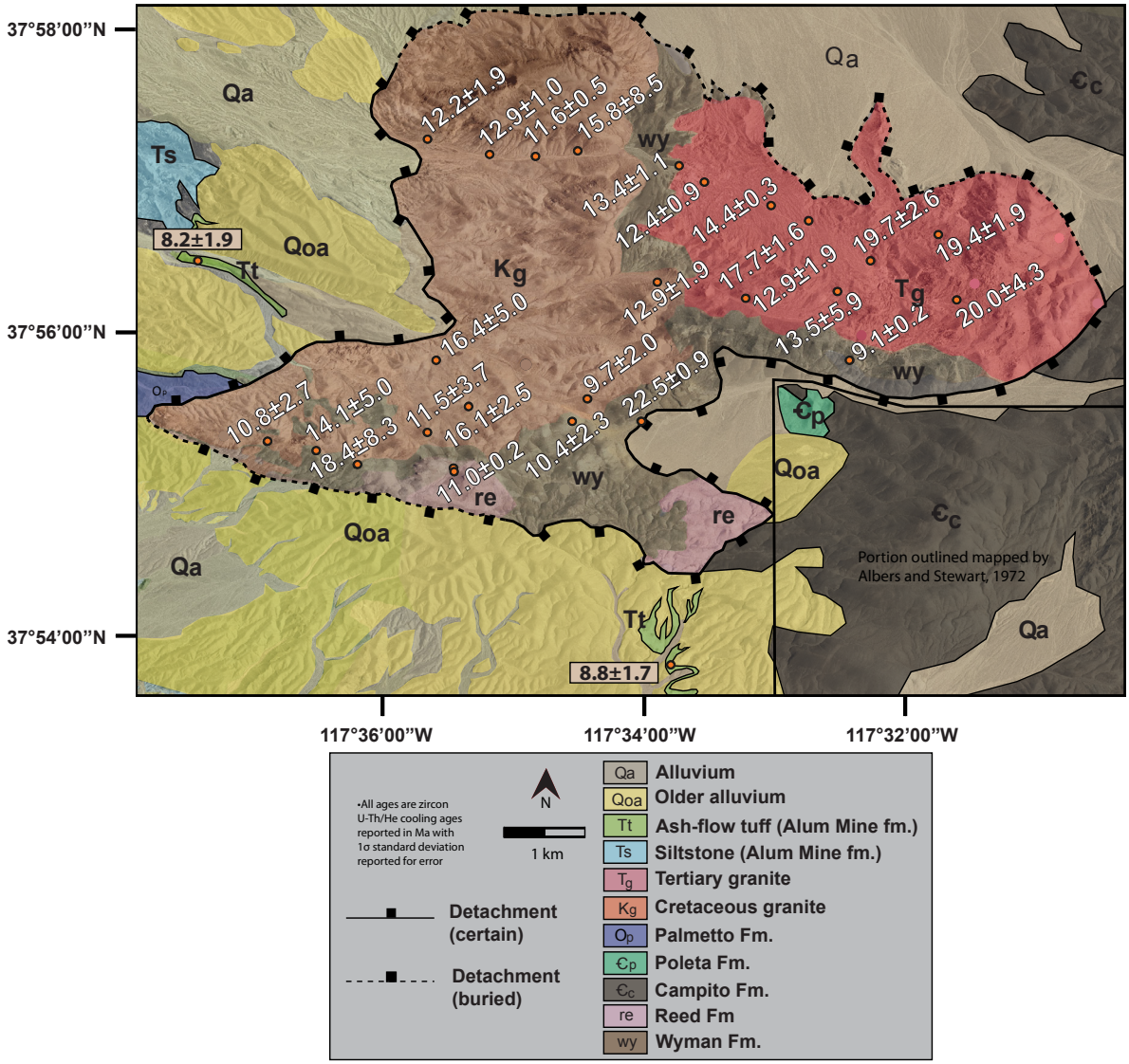

Figure 8: Zircon (U-Th)/He ages from the lower plate of the Weepah Hills metamorphic core complex. Image is digital orthophoto from the U.S.G.S. National Map viewer (http://national-map.gov/viewer.html). The lower plate map for this figure is based on unpublished mapping done by Caleb Stroup of Ram Power Corp.

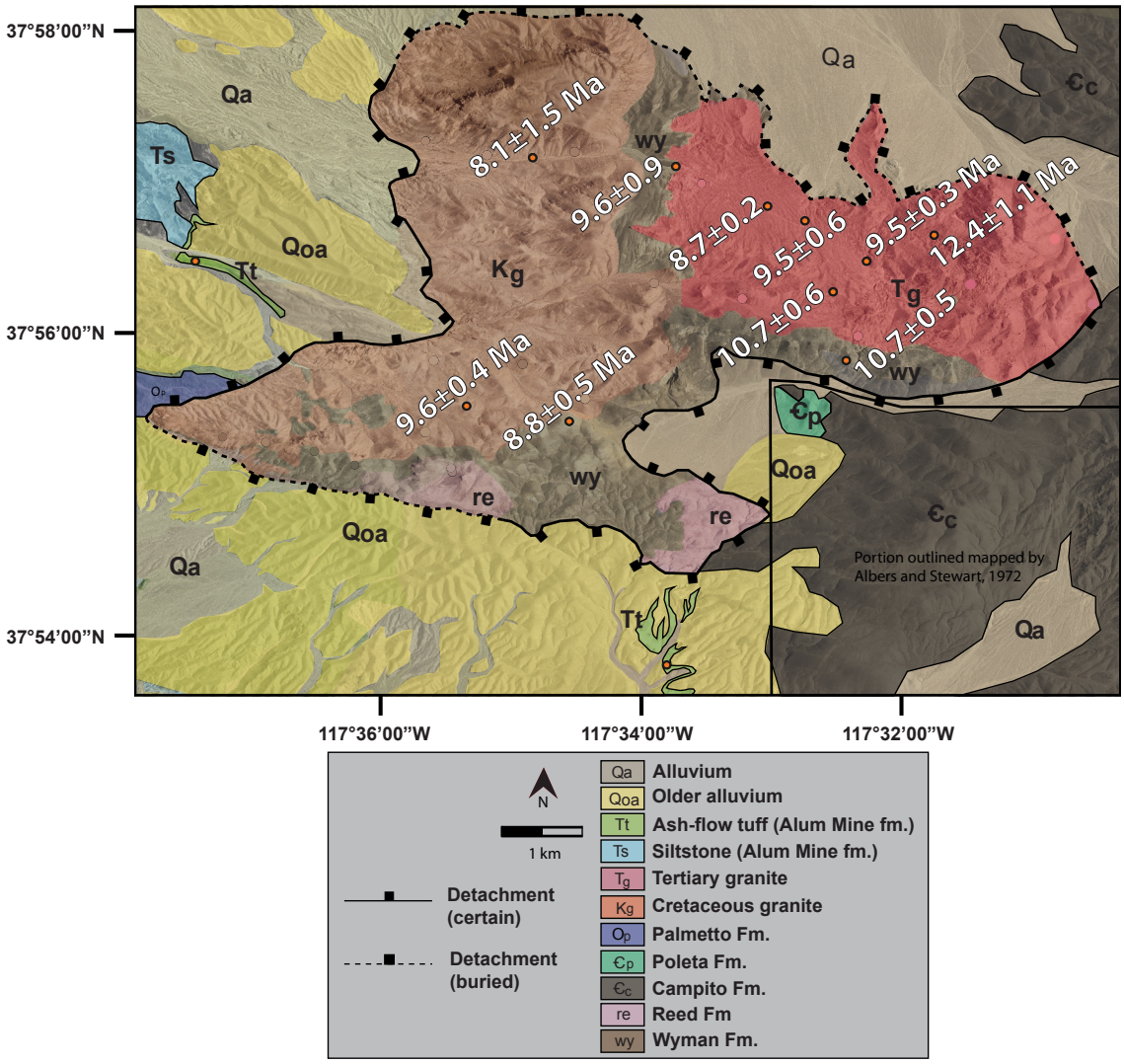

Figure 9: Apatite (U-Th)-He ages from the lower-plate of the Weepah Hills metamorphic core complex. Image is digital orthophoto from the U.S.G.S. National Map viewer (http://national-map.gov/viewer.html). The lower plate map for this figure is based on unpublished mapping done by Caleb Stroup of Ram Power Corp.

Sample	Age, Ma	err., Ma	U (ppm)	Th (ppm)	147Sm (ppm)	He (nmol/g)	Ft	ESR	Latitude	Longitude
z10CP012-1	17.1	1.4	1253.3	198.8	0.9	91.1	0.76	48.09	37.934	-117.588
z10CP012-2	11.1	0.9	485.1	81.7	0.5	22.1	0.73	41.88		
z10CP012-3	21.0	1.7	301.6	53.4	0.6	26.5	0.75	44.94		
Average age	16.4	5.0								
z10CP013-1	13.0	0.8	940.3	132.4	1.4	48.9	0.72	39.53	37.927	-117.572
z10CP013-2	9.5	0.6	500.4	86.8	1.6	20.6	0.78	52.06		
z10CP013-3	8.8	0.5	657.1	128.9	1.0	27.1	0.84	71.85		
Average age	10.4	2.3								
z10CP014-1	21.5	1.7	117.4	136.0	3.0	13.5	0.78	53.99	37.927	-117.564
z10CP014-2	23.1	1.8	338.7	502.7	5.7	41.8	0.73	44.51		
z10CP014-3	23.0	1.8	304.7	391.9	3.6	35.8	0.73	43.40		
Average age	22.5	0.9								
z10CP017-1	9.1	0.5	5.1	6.7	4.1	0.3	0.75	48.78	37.934	-117.539
z10CP017-2	9.3	0.6	8.7	14.2	21.9	0.4	0.69	38.01		
z10CP017-3	8.9	0.5	11.4	19.4	24.9	0.5	0.69	38.57		
Average age	9.1	0.2								
z10CP018-1	9.5	0.6	376.4	363.2	2.4	18.7	0.79	56.33	37.942	-117.541
z10CP018-2	20.3	1.2	239.5	228.5	0.7	26.4	0.82	68.24		
z10CP018-3	10.6	0.6	40.0	32.2	0.4	2.3	0.83	73.23		
Average age	13.5	5.9								
z10CP019-1	13.0	1.0	1005.8	676.1	1.0	64.7	0.79	57.61	37.955	-117.556
z10CP019-2	11.8	0.9	609.3	590.8	1.3	38.7	0.81	65.30		
Average age	12.4	0.9								
z10CP072-1	11.9	1.0	573.6	471.4	2.2	32.1	0.73	43.44	37.941	-117.551
z10CP072-2	10.9	0.9	959.4	511.9	1.3	51.8	0.81	64.67		
z10CP072-3	13.2	1.1	396.2	482.6	1.2	29.2	0.80	61.49		
z10CP072-4	15.4	1.2	1282.0	1463.1	1.7	113.5	0.84	75.93		
Average age	12.9	1.9								
z10CP078-1	11.5	0.9	123.3	33.4	0.4	6.2	0.76	47.79	37.924	-117.608
z10CP078-2	9.9	0.8	1754.8	437.7	1.4	72.5	0.73	42.65		
z10CP078-3	7.7	0.6	686.4	172.6	1.4	21.4	0.71	39.33		
z10CP078-4	14.0	1.1	1965.0	264.3	2.6	117.1	0.77	48.85		
Average age	10.8	2.7								

Table 3: Zircon (U-Th)/He ages from the footwall of the WHMCC. Samples marked with an asterisk were omitted in average age calculations due to the grain fracturing whenever it was unpacked from platinum after being heated by a laser. The loss of grain fragments after determining the helium concentration result in only a fraction of the parent isotopes of the complete grain being accounted for by analysis on the ICP-MS, resulting in an older age than the true ZHe age.

Sample	Age, Ma	err., Ma	U (ppm)	Th (ppm)	147Sm (ppm)	He (nmol/g)	Ft	ESR	Latitude	Longitude
z10CP079-1	16.4	1.3	467.2	129.3	0.6	34.9	0.79	56.81	37.923	-117.603
z10CP079-2	17.4	1.4	563.9	158.0	0.6	44.2	0.78	53.50		
z10CP079-3	8.3	0.7	1301.8	290.2	0.8	45.7	0.74	44.48		
Average age	14.1	5.0								
z10CP080-1	27.9	2.2	290.1	209.8	1.7	44.0	0.86	86.85	37.929	-117.598
z10CP080-2	13.9	1.1	2538.6	614.2	20.3	151.3	0.75	46.53		
z10CP080-3	13.4	1.1	98.3	62.5	3.1	6.3	0.77	52.20		
Average age	18.4	8.3								
z10CP081-1	9.0	0.7	469.2	111.7	0.7	18.9	0.78	54.09	37.926	-117.589
z10CP081-2	17.0	1.4	292.7	55.2	0.5	22.5	0.80	59.50		
z10CP081-3	9.9	0.8	682.9	181.6	0.5	31.1	0.80	59.34		
z10CP081-4	10.2	0.8	278.7	62.5	0.9	12.8	0.80	57.19		
Average age	11.5	3.7								
z10CP070b-1	9.4	0.8	272.0	216.3	2.4	12.1	0.74	45.72	37.921	-117.586
z10CP070b-2	12.6	1.0	433.1	71.7	0.6	18.8	0.61	27.94		
z10CP070b-3	-14.2	-1.1	0.2	0.4	0.0	0.0	0.78	54.72		
Average age	11.0	0.2								
z10CP082-1	13.5	1.1	1696.0	249.1	2.2	100.2	0.78	53.36	37.929	-117.584
z10CP082-2	16.3	1.3	1048.6	198.8	0.9	83.1	0.86	87.24		
z10CP082-3	18.5	1.5	779.7	63.5	2.2	62.3	0.78	53.31		
Average age	16.1	2.5								
z10CP084-1	12.6	1.0	1502.6	220.8	1.2	84.5	0.80	57.74	37.930	-117.570
z10CP084-2	9.1	0.7	911.6	97.3	1.4	35.7	0.78	51.59		
z10CP084-3	8.7	0.7	993.5	146.1	1.9	38.0	0.79	55.07		
z10CP084-4	8.4	0.7	1551.9	230.6	3.8	54.8	0.75	46.20		
Average age	9.7	2.0								
z10CP086-1	10.4	0.8	864.9	113.2	1.0	38.5	0.77	49.97	37.943	-117.562
z10CP086-2	14.7	1.2	1354.4	166.1	0.6	87.8	0.80	56.58		
z10CP086-3	14.0	1.1	752.9	158.8	0.3	48.2	0.81	60.48		
z10CP086-4	12.6	1.0	131.0	38.0	0.3	7.6	0.80	57.96		
Average age	12.9	1.9								
z10CP088-1	12.3	1.0	480.1	149.0	1.4	27.2	0.79	56.92	37.958	-117.582
z10CP088-2	12.4	1.0	492.2	129.4	0.6	28.4	0.81	62.76		
z10CP088-3	12.5	1.0	1188.7	341.2	1.6	66.1	0.77	50.72		
z10CP088-4	14.3	1.1	341.1	77.5	0.5	22.8	0.82	65.57		
Average age	12.9	1.0								

Table 3 continued: Zircon (U-Th)/He ages from the footwall of the WHMCC. Samples marked with an asterisk were omitted in average age calculations due to the grain fracturing whenever it was unpacked from platinum after being heated by a laser. The loss of grain fragments after determining the helium concentration result in only a fraction of the parent isotopes of the complete grain being accounted for by analysis on the ICP-MS, resulting in an older age than the true ZHe age.

Sample	Age, Ma	err., Ma	U (ppm)	Th (ppm)	147Sm (ppm)	He (nmol/g)	Ft	ESR	Latitude	Longitude
z11CV007-1	11.0	0.9	1276.5	299.9	2.8	58.4	0.73	42.70	37.961	-117.590
z11CV007-2	14.4	1.2	450.3	84.8	0.7	27.6	0.76	47.41		
z11CV007-3	11.2	0.9	924.1	115.3	1.3	45.2	0.79	53.81		
Average age	12.2	1.9								
z11CV008-1	12.0	1.0	829.6	164.2	0.8	45.4	0.81	60.71	37.958	-117.577
z11CV008-2	11.6	0.9	866.2	137.3	1.1	45.9	0.81	62.92		
z11CV008-3	11.1	0.9	872.7	155.0	0.8	39.3	0.72	41.14		
Average age	11.6	0.5								
z11CV009-2	13.1	1.1	248.8	49.9	0.4	14.5	0.78	53.91	37.359	-117.572
z11CV009-3	25.3	2.0	184.2	50.6	0.4	21.3	0.79	57.00		
z11CV009-4	8.9	0.7	865.1	152.4	0.9	33.6	0.77	51.03		
Average age	15.8	8.5								
z11CV010-1	12.3	1.0	923.5	448.7	1.9	53.4	0.78	54.08	37.957	-117.559
z11CV010-2	14.6	1.2	296.5	330.8	1.0	23.8	0.81	64.43		
z11CV010-3	13.3	1.1	352.5	434.0	1.3	25.1	0.77	51.57		
Average age	13.4	1.1								
z11CV011-1	14.2	1.1	277.7	222.1	1.0	21.2	0.84	77.25	37.953	-117.549
z11CV011-2	14.7	1.2	472.5	367.5	0.9	36.1	0.82	65.57		
z11CV011-3	14.3	1.1	513.9	532.3	1.0	40.5	0.82	67.58		
Average age	14.4	0.3								
z11CV012-1	19.4	1.6	589.7	392.8	0.7	57.6	0.80	61.48	37.951	-117.544
z11CV012-2	16.4	1.3	355.3	260.7	1.2	30.4	0.82	67.95		
z11CV012-3	17.2	1.4	394.4	230.2	0.7	35.0	0.84	77.53		
Average age	17.7	1.6								
z11CV013-1	18.1	1.5	483.0	294.0	0.7	42.5	0.79	55.90	37.942	-117.526
z11CV013-2	25.0	2.0	340.9	254.6	0.6	44.3	0.82	67.24		
z11CV013-4	17.0	1.4	476.9	279.1	0.5	38.1	0.76	49.99		
Average age	20.0	4.3								
z11CV015-1	0.2	0.0	858.5	599.3	1.0	0.8	0.80	59.99	37.949	-117.529
z11CV015-2	19.6	1.6	372.9	573.8	1.5	41.9	0.78	55.28		
z11CV015-3	21.2	1.7	261.5	240.4	0.6	29.1	0.80	60.69		
z11CV015-4	17.3	1.4	742.7	589.8	0.8	66.0	0.80	60.07		
Average age	19.4	1.9								

Table 3 continued: Zircon (U-Th)/He ages from the footwall of the WHMCC. Samples marked with an asterisk were omitted in average age calculations due to the grain fracturing whenever it was unpacked from platinum after being heated by a laser. The loss of grain fragments after determining the helium concentration result in only a fraction of the parent isotopes of the complete grain being accounted for by analysis on the ICP-MS, resulting in an older age than the true ZHe age.

Sample	Age, Ma	err., Ma	U (ppm)	Th (ppm)	147Sm (ppm)	He (nmol/g)	Ft	ESR	Latitude	Longitude
z10CV020-1	17.8	1.4	536.7	319.4	0.7	44.1	0.75	47.17	37.946	-117.537
z10CV020-2	22.6	1.8	717.1	508.8	0.8	80.0	0.78	54.82		
z10CV020-3	18.7	1.5	535.3	430.2	0.8	49.7	0.78	53.17		
Average age	19.7	2.6								

Table 3 continued: Zircon (U-Th)/He ages from the footwall of the WHMCC. Samples marked with an asterisk were omitted in average age calculations due to the grain fracturing whenever it was unpacked from platinum after being heated by a laser. The loss of grain fragments after determining the helium concentration result in only a fraction of the parent isotopes of the complete grain being accounted for by analysis on the ICP-MS, resulting in an older age than the true ZHe age.

Sample	Age, Ma	err., Ma	U (ppm)	Th (ppm)	147Sm (ppm)	He (nmol/g)	Ft	ESR	Latitude	Longitude
10CP013-1	8.8	0.53	4.7	7.0	35.4	0.2	0.73	57.97	37.927	-117.572
10CP013-2*	0.5	0.03	2.3	0.1	0.0	0.0	0.63	37.76		
10CP013-3*	-4.7	-0.28	0.4	-0.2	-0.1	0.0	0.66	32.59		
Average age	8.8	0.5								
10CP017-1	10.9	0.65	19.6	23.6	82.0	1.0	0.68	47.06	37.934	-117.539
10CP017-2	11.2	0.67	31.4	56.6	35.8	1.9	0.69	49.19		
10CP017-3	10.2	0.61	10.8	21.2	13.7	0.6	0.66	44.30		
Average age	10.7	0.5								
10CP018-1	9.6	0.58	17.3	68.0	32.1	1.4	0.81	84.36	37.942	-117.541
10CP018-2	9.6	0.57	15.4	66.9	30.5	1.3	0.77	71.08		
10CP018-3	10.7	0.6	22.6	72.8	34.0	1.9	0.81	83.64		
Average age	10.0	0.61								
10CP082-1	10.1	0.60	3.1	5.6	68.1	0.2	0.60	36.94	37.929	-117.584
10CP082-2	9.2	0.55	2.4	6.5	57.5	0.2	0.74	60.39		
10CP082-3	9.6	0.58	2.3	3.9	53.3	0.2	0.82	86.87		
Average age	9.6	0.4								
11CV008-1	9.2	0.55	7.6	17.2	52.8	0.4	0.72	56.41	37.958	-117.577
11CV008-2*	17.4	1.04	3.9	12.4	88.2	0.6	0.82	91.50		
11CV008-3	7.0	0.42	4.0	19.3	68.0	0.2	0.65	44.17		
11CV008-4*	15.2	0.91	17.0	29.7	108.4	1.4	0.69	49.55		
Average age	8.1	1.5								
11CV010-1	9.3	0.56	77.8	6.8	30.8	2.9	0.72	50.64	37.957	-117.559
11CV010-2	10.6	0.64	262.7	71.4	112.1	10.4	0.64	40.09		
11CV010-3	10.0	0.60	77.9	25.4	62.3	3.2	0.71	49.85		
11CV010-4	8.4	0.50	10.4	29.5	64.8	0.5	0.57	34.87		
Average age	9.6	0.9								
11CV011-1*	1675.1	100.51	14.5	55.8	38.9	180.2	0.65	44.83	37.953	-117.549
11CV011-2	8.8	0.53	11.3	38.1	17.6	0.6	0.62	39.97		
11CV011-3	8.3	0.50	8.8	34.4	17.3	0.5	0.61	38.88		
11CV011-4	8.8	0.53	12.5	48.7	20.2	0.7	0.60	38.52		
Average age	8.7	0.2								
11CV012-1*	20.2	1.21	13.3	109.3	41.7	2.9	0.68	48.93	37.951	-117.544
11CV012-2	9.1	0.54	18.8	66.4	35.1	1.3	0.75	64.15		
11CV012-3*	13.2	0.79	11.7	57.8	31.8	1.5	0.80	81.77		
11CV012-4	10.0	0.60	17.5	91.5	45.7	1.4	0.66	46.42		
Average age	9.5	0.6								

Table 4: Apatite (U-Th)/He ages from the footwall of the WHMCC. Samples marked with an asterisk were omitted in average age calculations due to the grain fracturing whenever it was unpacked from platinum after being heated by a laser. The loss of grain fragments after determining the helium concentration result in only a fraction of the parent isotopes of the complete grain being accounted for by analysis on the ICP-MS, resulting in an older age than the true AHe age.

Sample	Age, Ma	err., Ma	U (ppm)	Th (ppm)	147Sm (ppm)	He (nmol/g)	Ft	ESR	Latitude	Longitude
11CV015-1	13.2	0.79	11.1	44.9	35.9	1.0	0.65	45.02	37.949	-117.529
11CV015-2*	127.1	7.63	13.5	58.4	32.4	11.5	0.61	38.72		
11CV015-3	11.6	0.70	13.1	49.9	32.7	0.9	0.59	36.96		
Average age	12.4	1.1								
11CV020-1	9.1	0.55	14.7	61.4	33.1	1.1	0.76	67.33	37.946	-117.537
11CV020-2	9.6	0.58	13.0	56.2	30.9	1.0	0.74	60.89		
11CV020-3	9.9	0.59	11.5	47.3	28.2	0.8	0.62	40.06		
11CV020-4*	11.2	0.67	15.1	60.3	35.4	1.2	0.70	51.86		
Average age	9.5	0.3								

Table 4 continued: Apatite (U-Th)/He ages from the footwall of the WHMCC. Samples marked with an asterisk were omitted in average age calculations due to the grain fracturing whenever it was unpacked from platinum after being heated by a laser. The loss of grain fragments after determining the helium concentration result in only a fraction of the parent isotopes of the complete grain being accounted for by analysis on the ICP-MS, resulting in an older age than the true AHe age.

average age across the footwall of ~9 Ma. AHe ages record rapid cooling of the entire footwall below ~60˚C during exhumation. The consistent AHe ages compared to the varied ZHe ages conclude that the entire footwall is bounded by the detachment that caused unroofing to depths of less than 2 km by ~9 Ma.

4.2 THERMOCHRONOMETRIC CONSTRAINTS ON TERTIARY STRATIGRAPHY

Thirty-five samples were collected from outcrops of volcanic and volcano-clastic deposits from the Tertiary stratigraphy of the Weepah Hills basin sediments (Figure 10). The strata of the WHMCC are separated into five localities; the Alum Mine Flats, the Turtleback Badlands, the Contour Tuff Canyon, the Weepah Road Canyon and the Monocline Ridge area (Figure 11). The stratigraphy of sedimentary packages and the units bounding contacts varies across the different domains, reflecting complex lateral variations in thickness and lithologies along strike that are associated with complex depositional and deformational histories (Figure 12). The stratigraphy is primarily comprised of siliciclastic rocks, interbedded with thin epiclastic volcanic units and volcanic rocks of variable composition including ash-fall tuffs, siliceous tuff and basaltic flows (Figures 3, 4 and 12). The stratigraphy can be divided into three unconformity-bounded depositional packages (Figure 13). These packages are disrupted by two generations of high-angle normal faults formed during detachment faulting. The basin sediments of the WHMCC record synextensional deposition that spans the kinematic transition from early Miocene

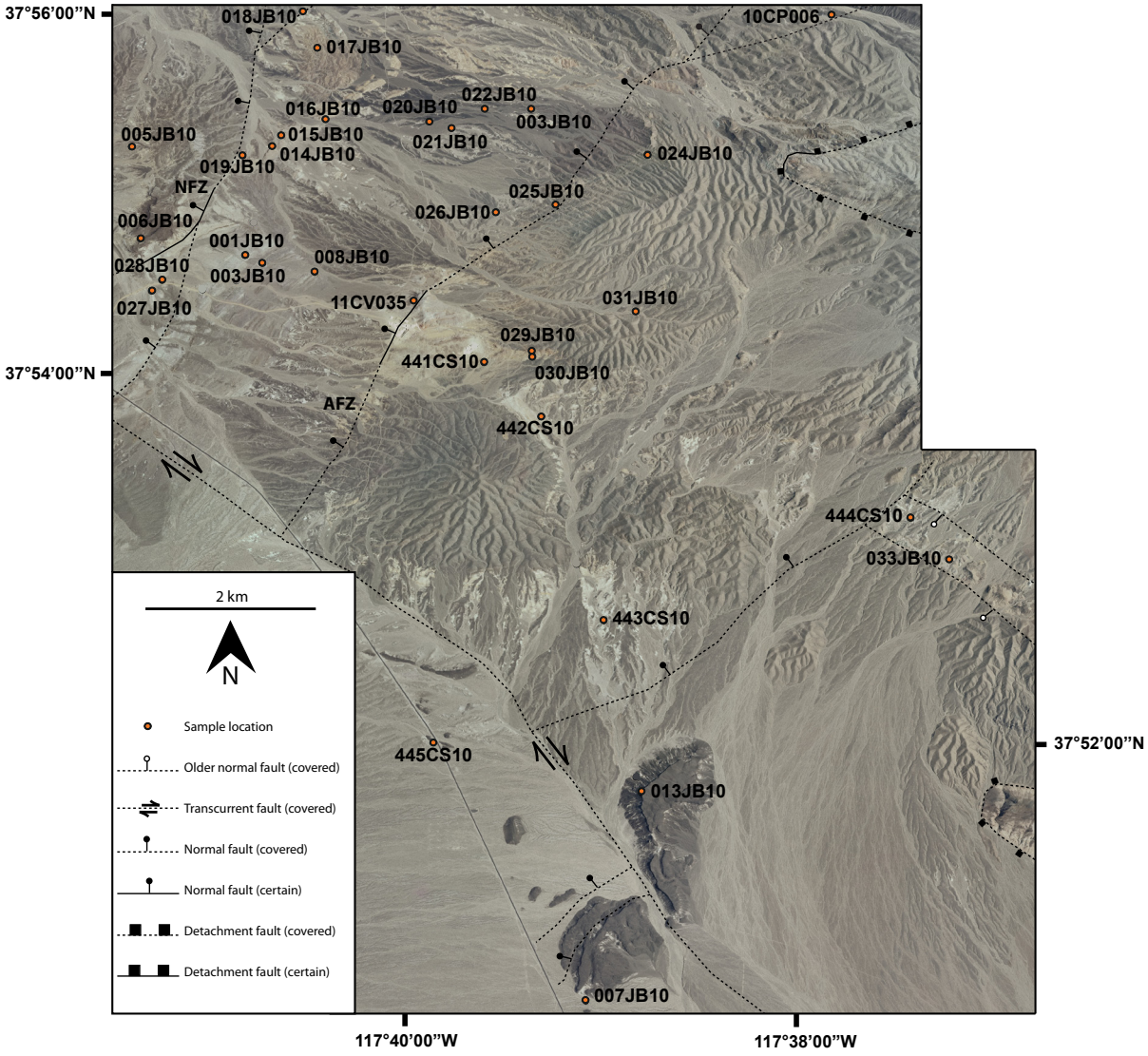

Figure 10: Sample locations for basin sediments from the upper plate of the Weepah Hills metamorphic core complex. AFZ-Alum fault zone; NFZ-Northern fault zone. Image is digital orthophoto downloaded from the U.S.G.S. National Map viewer (http://nationalmap.gov/viewer.html).

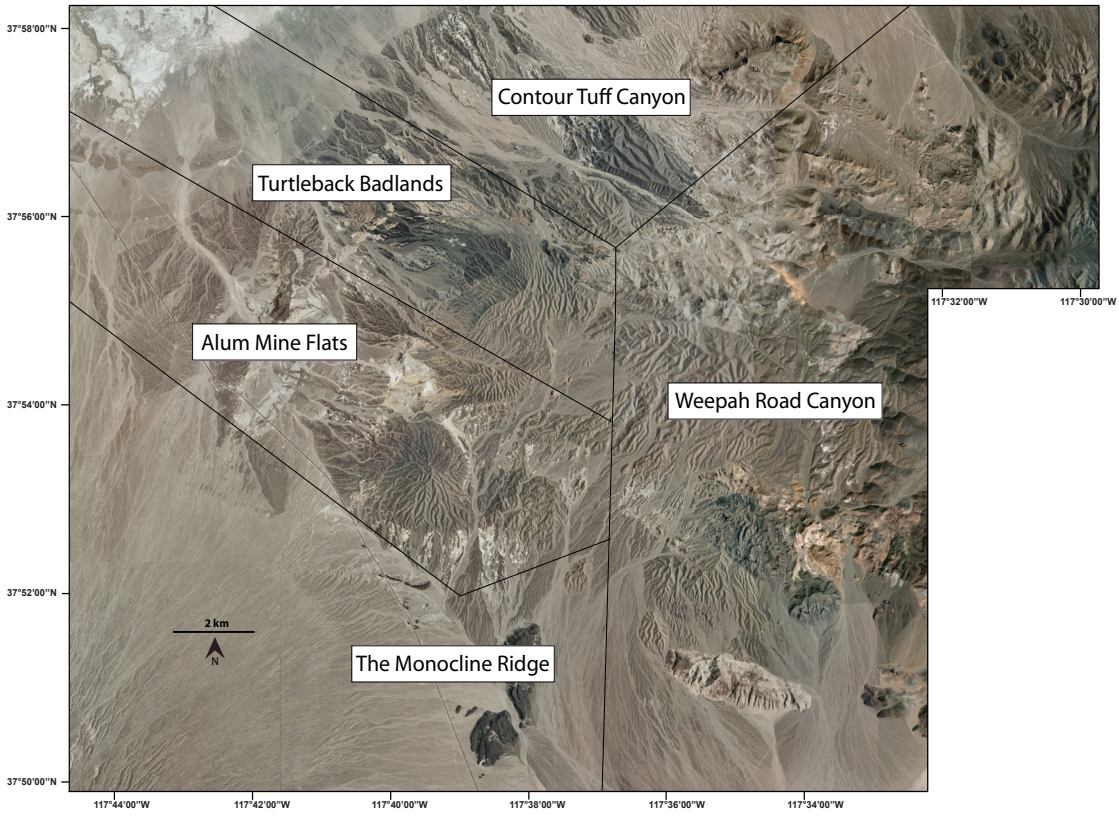

Figure 11: Five domains of the upper plate strata for the Weepah Hills area. The five domains represent the multi-stage depositional history of the basin. The domains are differentiated based on the strata that is exposed and the style of deformation experienced by upper plate units. Each domain records a unique aspect of the tectonic evolution of the Weepah Hills area. Image is digital orthophoto from the U.S.G.S. National Map viewer (http://nationalmap.gov/viewer.html).

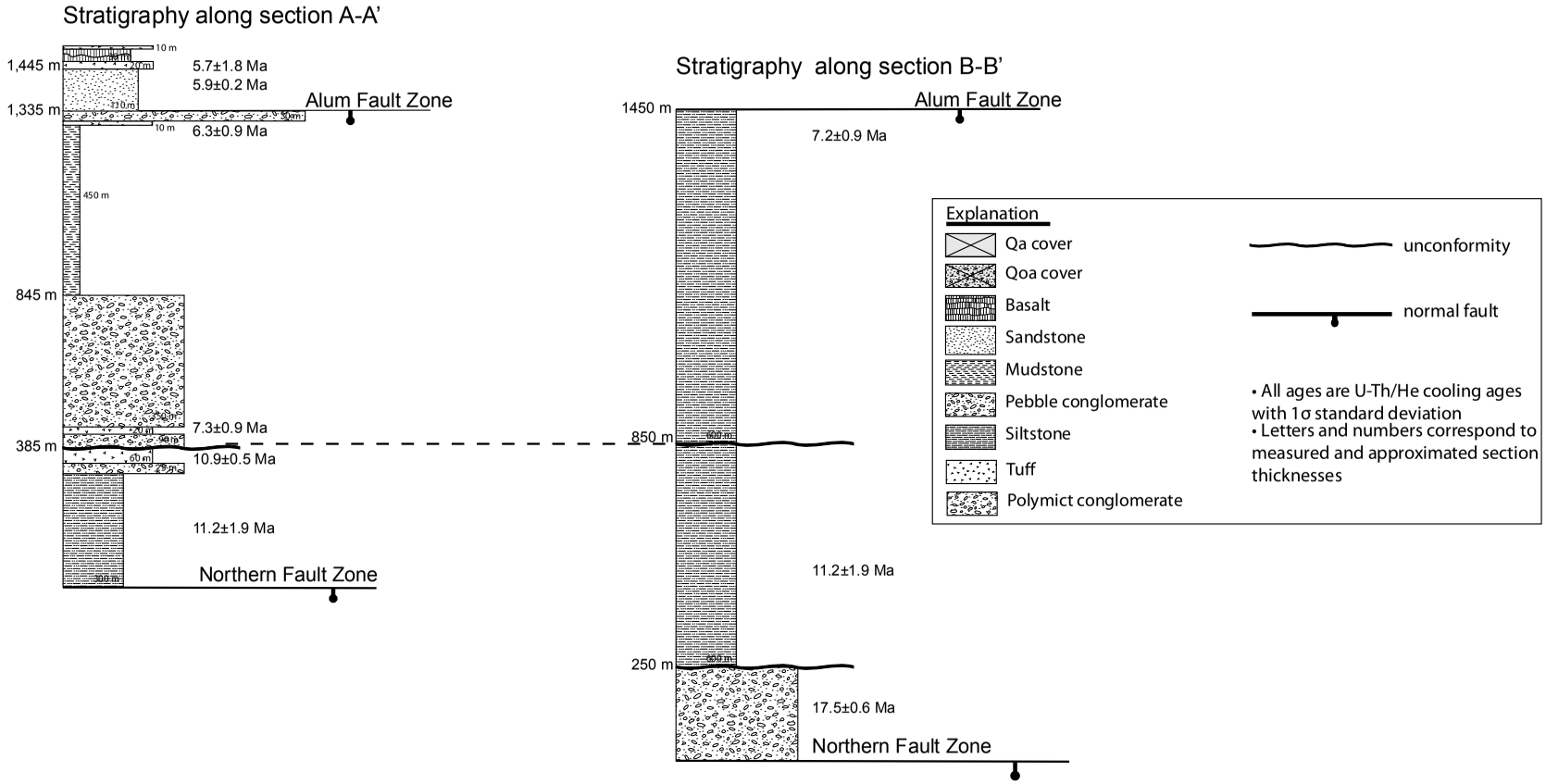

Figure 12: Composite measured section of the upper plate sediments along cross-sections A-A' and B-B'. A-A' represents stratigraphy in the Alum Mine Flats domain; B-B' is representative of the stratigraphy of the Turtleback Badlands domain.

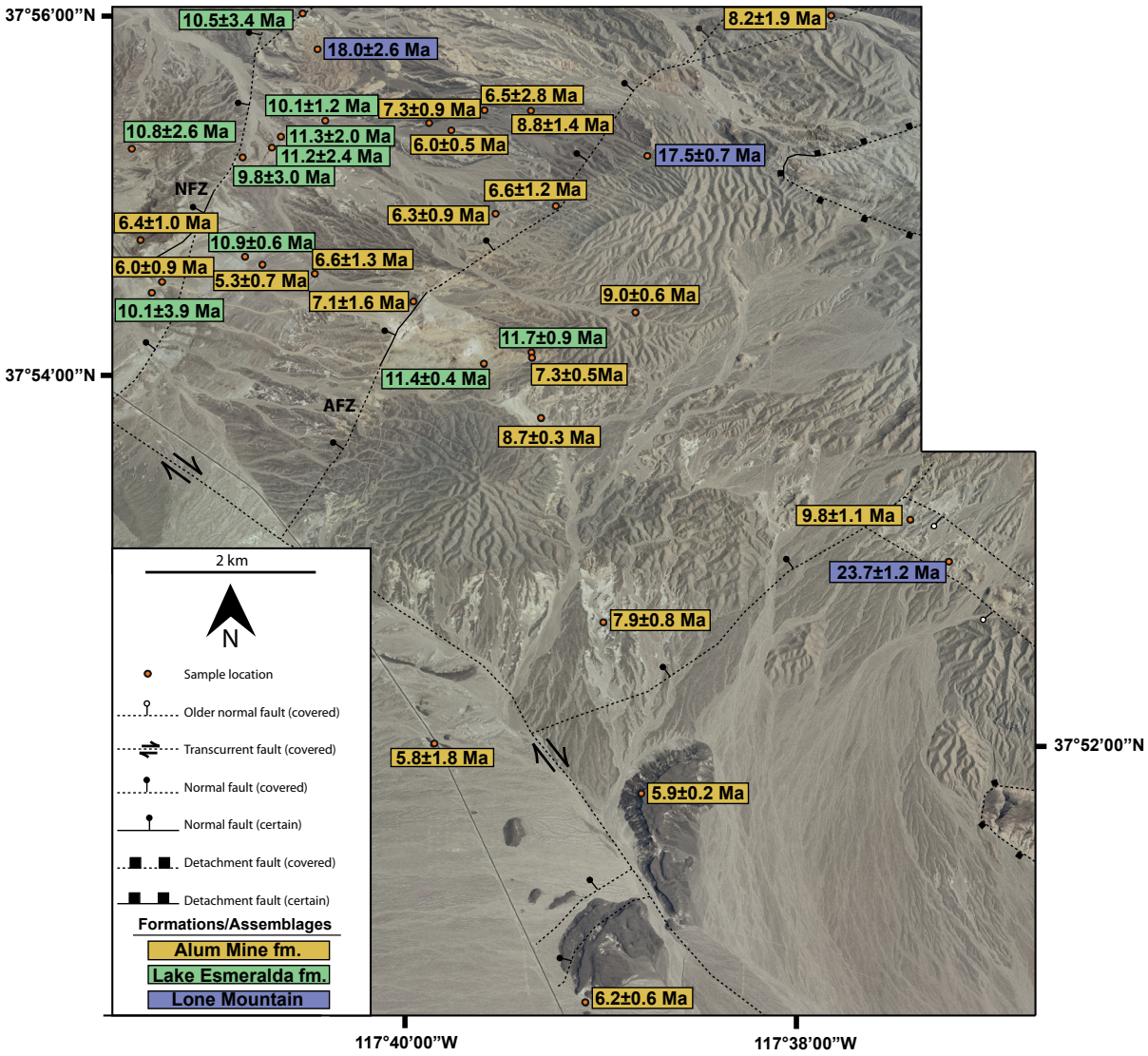

Figure 13: Samples collected from the basin sediments of the Weepah Hills metamorphic core complex. Zircon He ages represent an eruptive age for the upper plate volcano-sedimentary strata. The ages record three depositional packages in the basin, differentiated by three colors on the figure. Ages in blue boxes are late Oligocene to early Miocene, ages in green boxes are middle Miocene, and ages in orange are early Miocene strata. These three depositional packages are interpreted to be bounded by unconformities, and record a multi-stage basin evolution that records the kinematic transition from extension to transtension across the Miocene. Older high-angle normal faults shown are interpreted to be associated with Miocene E-W Basin-and Range extension, and cut the early Miocene strata. Miocene detachment faults and Mio-Pliocene dextral transcurrent and high-angle normal faults are associated with transtension. Image is digital ortho-photo from the U.S.G.S. National Map viewer (http://nationalmap.gov/viewer.html).

Basin and Range style extension to transtension associated with detachment faulting in the SPLM extensional system.

4.2.1 Lower-Paleozoic section

Lower-Paleozic miogeoclinal rocks form the pre-Tertiary stratigraphy of the WHMCC (Figure 4). Proterozoic to lower Paleozoic rocks are interpreted were deposited in a basin along the continental margin of the western United States (Oldow et al., 1984). These rocks crop out extensively across west-central Nevada. The Proterozoic to lower Paleozoic section is comprised of dolomite, quartzite and limestone of the Proterozoic Wyman, Reed and Deep Springs Formations and the Cambrian Campito, Poleta, Harkless, Mule Springs, and Emigrant Formations, with a total thickness greater than 15 km (Albers and Stewart, 1972). In this region of Nevada, the Ordovician rocks constitute the overriding plate of the Roberts Mountains thrust fault system, during mid-Paleozoic deformation (Oldow et al., 1984; Burchfiel et al., 1992). Plutons across the region were emplaced during the Jurassic and Cretaceous, but no remnant of the Mesozoic deposition is preserved in the stratigraphic column (Albers and Stewart, 1972).

4.2.2 Early Miocene strata

The lower Tertiary strata lies unconformably on the lower-Paleozoic meta-sedimentary rocks, and is informally referred to as the Lone Mountain group in this manuscript. The Lone Mountain group is comprised of a basal rhyolitic flow, a welded

ash-flow tuff, and a polymict conglomerate containing Paleozoic-derived clasts that hosts interbedded lithic-rich epiclastic tuffs. These units are interpreted, based on field relationships and ZHe data, to be bounded by late Oligocene and early Miocene unconformities (Figure 5). The Lone Mountain group has limited exposure in the WHMCC, due to burial by alluvium. The lower two units of the Lone Mountain group only crop out in Weepah Road Canyon and are absent in the other domains of the WHMCC. The upper conglomerate is limited to the Turtleback Badlands area (Figure 11).

Weepah Road Canyon

The lower extent of the Tertiary section is marked by a basal rhyolitic flow that was dated in this study by ZHe at 30.1±4.6 Ma (Figure 5) (Table 3; sample z11CV018). The rhyolitic flow lies unconformably on a folded and imbricated segment of the lower-Paleozoic strata. The upper and lower contacts are poorly exposed, but the rhyolite that caps the meta-sedimentary rocks appears to be less than a 60 m flow. The upper contact of the lower rhyolite is not exposed in the WHMCC, but it is interpreted to be an unconformity based on its up-dip proximity to the overlying welded ash-flow tuff. The welded ash-flow tuff of the Lone Mountain group dips 34° to the northeast, and was dated in this study at 23.7±1.1 Ma by ZHe (Figure 13). At this locality, the upper polymict conglomerate is absent and the welded tuff is unconformably overlain by a shallowly dipping un-welded ash flow tuff of the Weepah Hills group. The late Oligocene welded tuff does not crop out in the other four upper plate domains of the WHMCC, and is never documented in well logs from hydrothermal drilling in the area. This suggests the welded tuff

Sample	Age, Ma	err., Ma	U (ppm)	Th (ppm)	147Sm (ppm)	He (nmol/g)	Ft	ESR	Latitude	Longitude
z10CP006-1	10.7	0.9	1.3	8.8	13.0	0.2	0.77	53.37	37.946	-117.617
z10CP006-2	8.5	0.7	2.5	14.7	39.4	0.2	0.69	39.76		
z10CP006-3	7.3	0.6	1.7	11.7	32.8	0.1	0.77	54.79		
z10CP006-4	6.3	0.5	57.8	86.0	2.0	2.1	0.77	53.25		
Average age	8.2	1.9								
z10CP015-1	10.9	0.9	218.6	208.8	13.1	12.0	0.76	50.46	37.877	-117.557
z10CP015-2	11.8	0.9	68.1	57.1	0.9	3.8	0.72	42.33		
z10CP015-3	10.0	0.8	67.6	27.5	0.6	2.9	0.72	41.08		
Average age	10.9	0.9								
z11CV004-1	7.3	0.6	361.5	446.5	2.3	11.8	0.64	31.95	37.901	-117.562
z11CV004-2*	567.2	45.4	59.6	27.6	1.8	130.2	0.62	29.39		
z11CV004-3	10.6	0.8	1142.1	1079.5	1.2	48.8	0.61	29.15		
z11CV004-4	8.4	0.7	58.5	88.8	1.7	2.0	0.57	25.94		
Average age	8.8	1.7								
z11CV018-1	29.7	2.4	121.5	89.6	0.8	17.1	0.75	46.71	37.877	-117.556
z11CV018-2	23.9	1.9	342.9	256.3	1.0	39.7	0.76	49.90		
z11CV018-3	32.7	2.6	51.6	56.1	1.1	8.8	0.77	52.30		
z11CV018-4	34.4	2.8	101.5	146.9	1.8	20.4	0.81	63.58		
Average age	30.2	4.6								
z11CV035-1*	48.0	3.8	311.1	212.1	1.1	65.2	0.70	38.02	37.912	-117.665
z11CV035-2	5.6	0.5	212.2	311.8	1.6	6.8	0.78	54.95		
z11CV035-3	7.0	0.6	1549.2	2463.7	2.6	61.2	0.76	49.34		
z11CV035-4	8.7	0.7	233.6	121.7	1.2	9.5	0.77	50.29		
Average age	7.1	1.6								
z441CS10-1	11.0	0.9	229.9	303.7	2.6	13.5	0.75	48.68	37.904	-117.657
z441CS10-2	11.1	0.9	335.1	450.1	2.5	20.7	0.78	56.37		
z441CS10-3	11.1	0.9	220.8	215.2	1.3	12.4	0.76	50.37		
z441CS10-4*	9.6	0.8	392.2	506.3	3.3	20.5	0.77	53.43		
z441CS10-5	11.6	0.9	184.1	191.8	1.0	11.9	0.82	69.19		
z441CS10-6	11.9	1.0	337.7	360.6	1.7	20.5	0.75	48.47		
Average age	11.4	0.4								

Table 5: Zircon (U-Th)/He ages from the upper plate of the WHMCC. Samples marked with an asterisk were omitted in average age calculations due to the grain fracturing whenever it was unpacked from platinum after being heated by a laser. The loss of grain fragments after determining the helium concentration result in only a fraction of the parent isotopes of the complete grain being accounted for by analysis on the ICP-MS, resulting in an older age than the true ZHe age. Aliquots that represent inheritance from an older source are also omitted from average ZHe ages.

Sample	Age, Ma	err., Ma	U (ppm)	Th (ppm)	147Sm (ppm)	He (nmol/g)	Ft	ESR	Latitude	Longitude
z442CS10-1*	52.0	4.2	1.3	3.0	8.5	0.4	0.71	41.16	37.898	-117.650
z442CS10-2*	11.5	0.9	3.0	9.9	25.1	0.3	0.73	45.41		
z442CS10-3	8.9	0.7	4.2	12.3	30.6	0.2	0.69	39.26		
z442CS10-4*	4.0	0.3	10.4	20.6	38.5	0.2	0.72	42.50		
z442CS10-5	8.5	0.7	6.3	23.1	30.0	0.4	0.72	42.82		
z442CS10-6*	15.8	1.3	1.8	5.4	10.3	0.2	0.79	60.01		
Average age	8.7	0.3								
z443CS10-1	7.7	0.6	138.4	110.3	6.3	5.0	0.74	45.24	37.874	-117.643
z443CS10-2	8.4	0.7	43.7	53.6	10.8	2.1	0.83	70.28		
z443CS10-3	6.5	0.5	48.4	58.6	2.0	1.6	0.75	48.66		
z443CS10-4	8.9	0.7	102.0	128.1	18.7	4.6	0.73	43.74		
z443CS10-5	8.1	0.6	33.2	42.4	4.5	1.4	0.74	45.60		
z443CS10-6	8.0	0.6	174.7	159.6	46.6	6.9	0.75	47.79		
Average age	7.9	0.8								
z444CS10-1	8.6	0.7	792.3	1019.3	34.9	34.8	0.73	43.34	37.886	-117.608
z444CS10-2*	16.9	1.4	94.5	104.8	7.1	8.2	0.75	48.20		
z444CS10-3	8.7	0.7	144.5	105.4	24.2	5.9	0.75	47.03		
z444CS10-4	9.4	0.8	159.4	166.9	27.1	7.6	0.75	47.41		
z444CS10-5	8.8	0.7	182.9	164.9	8.7	7.9	0.75	47.03		
z444CS10-6*	4.0	0.3	196.6	171.9	22.7	3.9	0.76	50.52		
z444CS10-7	9.7	0.8	65.3	53.1	6.1	3.3	0.82	68.13		
z444CS10-8	10.6	0.8	104.0	127.5	4.6	5.9	0.77	52.28		
z444CS10-9	11.2	0.9	223.1	175.0	25.6	10.9	0.68	36.59		
z444CS10-10	11.1	0.9	189.1	163.4	20.0	9.4	0.69	37.78		
Average age	9.8	1.1								
z445CS10-1	7.9	0.6	0.5	0.2	0.6	0.0	0.82	65.98	37.861	-117.663
z445CS10-2	4.6	0.4	0.2	0.2	1.0	0.0	0.84	74.77		
z445CS10-3*	169.4	13.6	0.1	0.0	0.0	0.1	0.81	58.25		
z445CS10-4*	59.8	4.8	0.3	0.2	0.4	0.1	0.80	61.32		
z445CS10-5	4.9	0.4	0.8	1.2	0.7	0.0	0.78	56.14		
z445CS10-6*	53.7	4.3	0.2	0.6	3.1	0.1	0.85	84.17		
Average age	5.8	1.8								

Table 5 continued: Zircon (U-Th)/He ages from the upper plate of the WHMCC. Samples marked with an asterisk were omitted in average age calculations due to the grain fracturing whenever it was unpacked from platinum after being heated by a laser. The loss of grain fragments after determining the helium concentration result in only a fraction of the parent isotopes of the complete grain being accounted for by analysis on the ICP-MS, resulting in an older age than the true ZHe age. Aliquots that represent inheritance from an older source are also omitted from average ZHe ages.

Sample	Age, Ma	err., Ma	U (ppm)	Th (ppm)	147Sm (ppm)	He (nmol/g)	Ft	ESR	Latitude	Longitude
z001JB10-1	10.4	0.8	646.9	861.0	1.7	39.0	0.81	66.29	37.917	-117.684
z001JB10-2	10.4	0.8	899.0	1286.5	1.3	49.4	0.73	44.59		
z001JB10-3	11.5	0.9	613.2	532.2	0.8	35.8	0.78	54.14		
z001JB10-4	11.5	0.9	1067.7	1530.4	1.8	64.1	0.72	42.47		
z001JB10-5	10.5	0.8	541.8	592.4	1.0	30.4	0.78	55.70		
z001JB10-6*	8.4	0.7	245.2	234.3	3.6	10.9	0.81	62.39		
Average age	10.9	0.6								
z003JB10-1*	71.9	4.3	412.2	2.6	1024.7	303.94	0.76	48.66	37.914	-117.685
z003JB10-2	4.7	0.3	126.9	0.8	179.6	3.88	0.85	81.31		
z003JB10-3	6.2	0.4	267.4	1.0	259.0	6.25	0.72	42.69		
z003JB10-4	4.5	0.3	74.3	0.6	112.5	2.28	0.83	69.39		
z003JB10-5	6.0	0.4	301.6	0.9	277.6	6.77	0.75	48.56		
z003JB10-6	5.3	0.3	141.4	0.4	204.5	4.56	0.78	53.45		
Average age	5.3	0.7								
z005JB10-1	13.4	0.8	213.9	191.8	1.3	13.8	0.74	45.38	37.930	-117.697
z005JB10-2	11.8	0.7	1040.4	162.9	0.4	49.6	0.72	40.95		
z005JB10-3*	94.5	5.7	569.3	160.5	0.5	231.2	0.74	44.81		
z005JB10-4	11.9	0.7	211.0	130.7	0.6	10.9	0.70	38.28		
z005JB10-5	6.6	0.4	49.3	54.6	0.9	1.7	0.75	47.49		
z005JB10-6	10.4	0.6	297.6	174.1	0.8	14.5	0.77	50.64		
Average age	10.8	2.6								
z006JB10-1	7.9	0.5	174.8	130.4	0.7	7.3	0.83	69.67	37.918	-117.697
z006JB10-2	5.8	0.3	315.3	346.8	1.8	8.7	0.70	39.46		
z006JB10-3	6.1	0.4	91.6	74.0	1.3	3.0	0.85	81.96		
z006JB10-4*	71.5	4.3	825.8	252.6	2.9	265.0	0.77	51.41		
z006JB10-5*			0.5	0.9	0.2	150.9	0.78	54.61		
z006JB10-6	5.9	0.4	211.3	219.5	0.9	6.2	0.75	47.37		
Average age	6.4	1.0								
z007JB10-1	6.5	0.4	175.4	212.3	2.2	6.0	0.77	52.28	37.834	-117.645
z007JB10-2	6.1	0.4	92.2	103.0	1.2	3.0	0.77	52.91		
z007JB10-3	7.1	0.4	265.2	185.2	1.2	10.1	0.86	85.17		
z007JB10-4	6.5	0.4	197.7	195.0	1.3	7.1	0.83	72.78		
z007JB10-5	6.1	0.4	76.8	72.9	0.9	2.6	0.84	75.96		
z007JB10-6	5.2	0.3	135.8	123.5	0.6	3.7	0.80	61.97		
Average age	6.2	0.6								

Table 5 continued: Zircon (U-Th)/He ages from the upper plate of the WHMCC. Samples marked with an asterisk were omitted in average age calculations due to the grain fracturing whenever it was unpacked from platinum after being heated by a laser. The loss of grain fragments after determining the helium concentration result in only a fraction of the parent isotopes of the complete grain being accounted for by analysis on the ICP-MS, resulting in an older age than the true ZHe age. Aliquots that represent inheritance from an older source are also omitted from average ZHe ages.

Sample	Age, Ma	err., Ma	U (ppm)	Th (ppm)	147Sm (ppm)	He (nmol/g)	Ft	ESR	Latitude	Longitude
z008JB10-1*	329.5	19.8	89.7	34.1	0.1	140.0	0.79	55.30	37.915	-117.676
z008JB10-2	6.3	0.4	160.1	92.4	0.8	4.8	0.79	56.06		
z008JB10-3*	77.8	4.7	624.7	165.4	0.9	223.6	0.80	58.49		
z008JB10-4	5.5	0.3	55.1	69.8	2.1	1.6	0.75	48.69		
z008JB10-5*	99.6	6.0	686.5	292.2	1.0	292.1	0.72	40.51		
z008JB10-6	8.1	0.5	189.6	102.3	1.3	7.3	0.78	53.03		
Average age	6.6	1.3								
z013JB10-1*	0.0	0.0	443.8	562.2	1.0	13.8	0.78	53.76	37.856	-117.639
z013JB10-2	5.7	0.5	53.2	67.2	1.7	1.8	0.80	59.44		
z013JB10-3	5.7	0.5	151.3	130.6	0.4	5.3	0.85	84.52		
z013JB10-4	5.9	0.5			1376.7	11.2	0.77	66.91		
z013JB10-5	6.0	0.5	343.7	463.7	0.8	10.2	0.71	40.34		
z013JB10-6	6.3	0.5	234.1	247.1	1.7	7.1	0.79	58.08		
Average age	5.9	0.2								
z014JB10-1	10.2	0.8	286.2	170.0	1.4	14.0	0.78	53.47	37.930	-117.681
z014JB10-2	13.9	1.1	93.1	153.3	15.2	7.4	0.76	50.87		
z014JB10-3	9.3	0.7	1434.6	1122.7	2.3	62.7	0.73	43.90		
z014JB10-4*	70.3	5.6	0.9	1.7	0.2	0.4	0.72	43.65		
Average age	11.2	2.4								
z015JB10-1	9.3	0.7	1122.8	710.5	1.4	50.1	0.78	53.52	37.931	-117.680
z015JB10-2	9.9	0.8	344.8	189.4	1.7	15.8	0.76	48.84		
z015JB10-3	12.9	1.0	101.2	89.1	1.0	12.1	0.85	80.18		
z015JB10-4	13.1	1.0	150.1	103.6	1.6	45.3	0.76	48.77		
z015JB10-5*	21.7	1.7	499.7	394.9	3.3	31.6	0.77	51.51		
z015JB10-6*	63.3	5.1	447.0	289.9	1.5	28.9	0.79	57.83		
Average age	11.3	2.0								
z016JB10-1	8.9	0.7	733.3	674.1	2.3	32.2	0.75	47.80	37.933	-117.675
z016JB10-2	9.2	0.7	254.2	237.4	1.6	16.3	0.79	58.42		
z016JB10-3	9.9	0.8	333.7	232.7	1.0	16.8	0.78	55.18		
z016JB10-4	10.0	0.8	839.7	582.0	1.4	35.9	0.74	45.55		
z016JB10-5	10.2	0.8	1220.1	1590.3	2.1	59.7	0.70	39.54		
z016JB10-6	12.3	1.0	1127.3	906.3	1.5	51.1	0.71	40.05		
Average age	10.1	1.2								

Table 5 continued: Zircon (U-Th)/He ages from the upper plate of the WHMCC. Samples marked with an asterisk were omitted in average age calculations due to the grain fracturing whenever it was unpacked from platinum after being heated by a laser. The loss of grain fragments after determining the helium concentration result in only a fraction of the parent isotopes of the complete grain being accounted for by analysis on the ICP-MS, resulting in an older age than the true ZHe age. Aliquots that represent inheritance from an older source are also omitted from average ZHe ages.

Sample	Age, Ma	err., Ma	U (ppm)	Th (ppm)	147Sm (ppm)	He (nmol/g)	Ft	ESR	Latitude	Longitude
z017JB10-1	16.6	1.0	480.7	346.7	1.9	39.1	0.78	53.10	37.942	-117.676
z017JB10-2*	28.2	1.7	336.0	188.7	0.8	40.5	0.70	38.04		
z017JB10-3*	75.2	4.5	260.9	194.9	0.8	84.8	0.68	35.80		
z017JB10-4	16.4	1.0	231.5	163.7	2.6	15.6	0.65	32.84		
z017JB10-5	21.0	1.3	150.3	328.3	2.2	17.2	0.67	35.42		
z017JB10-6*	11.3	0.7	276.1	202.3	1.4	13.1	0.66	33.85		
Average age	18.0	2.6								
z018JB10-1	8.1	0.5	443.5	393.4	1.3	18.2	0.78	53.72	37.946	-117.677
z018JB10-2*	72.6	4.4	469.2	175.1	0.9	143.5	0.72	40.23		
z018JB10-3*	83.5	5.0	733.4	377.2	1.4	281.9	0.76	48.47		
z018JB10-4*	135.6	8.1	446.4	139.2	0.7	276.9	0.78	53.98		
z018JB10-5	12.9	0.8	376.1	154.6	0.4	23.0	0.80	60.03		
z018JB10-6*	69.7	4.2	525.4	255.6	0.8	174.4	0.79	55.95		
Average age	10.5	3.4								
z019JB10-1	70.4	4.2	358.0	200.4	1.6	112.1	0.73	42.46	37.929	-117.684
z019JB10-2	10.7	0.6	276.2	312.2	2.2	15.0	0.74	46.28		
z019JB10-3	10.4	0.6	253.4	116.1	0.7	12.7	0.80	60.47		
z019JB10-4	8.3	0.5	134.7	70.8	0.6	5.4	0.80	59.09		
z019JB10-5	9.8	0.6	711.8	551.6	0.8	33.7	0.76	49.16		
z019JB10-6	16.2	1.0	617.0	360.5	1.2	46.4	0.76	48.78		
Average age	9.8	3.0								
z020JB10-1	6.7	0.5	158.1	60.7	0.4	6.3	0.81	61.95	37.933	-117.663
z020JB10-2	6.8	0.5	234.2	345.1	1.4	41.1	0.84	79.89		
z020JB10-3	8.4	0.7	270.4	197.2	2.1	24.5	0.84	77.41		
z020JB10-4*	17.0	1.4	0.5	0.4	0.0	8.9	0.81	62.30		
z020JB10-5*	28.5	2.3	258.2	347.4	1.2	9.8	0.80	60.15		
z020JB10-6*	2190.1	175.2	129.9	72.0	0.7	4.3	0.80	58.51		
Average age	7.3	0.9								
z021JB10-1	5.5	0.3	470.0	697.7	2.0	14.9	0.79	56.94	37.932	-117.660
z021JB10-2	9.2	0.6	312.7	412.0	1.8	15.2	0.75	47.26		
z021JB10-3	6.0	0.4	108.8	175.3	8.1	3.6	0.74	46.49		
z021JB10-4	6.3	0.4	62.5	127.1	2.8	2.1	0.68	37.54		
z021JB10-5	6.7	0.4	96.3	64.8	0.9	2.9	0.72	41.43		
z021JB10-6	5.4	0.3	75.6	101.3	3.8	2.0	0.68	36.85		
Average age	6.0	0.5								

Table 5 continued: Zircon (U-Th)/He ages from the upper plate of the WHMCC. Samples marked with an asterisk were omitted in average age calculations due to the grain fracturing whenever it was unpacked from platinum after being heated by a laser. The loss of grain fragments after determining the helium concentration result in only a fraction of the parent isotopes of the complete grain being accounted for by analysis on the ICP-MS, resulting in an older age than the true ZHe age. Aliquots that represent inheritance from an older source are also omitted from average ZHe ages.

Sample	Age, Ma	err., Ma	U (ppm)	Th (ppm)	147Sm (ppm)	He (nmol/g)	Ft	ESR	Latitude	Longitude
z022JB10-1	6.6	0.5	248.0	243.6	0.7	7.9	0.73	43.56	37.935	-117.656
z022JB10-2	11.7	0.9	390.9	233.3	0.9	20.9	0.74	45.90		
z022JB10-3*	41.9	3.4	402.5	317.4	1.2	79.3	0.73	43.96		
z022JB10-4	8.9	0.7	665.0	197.6	1.1	25.9	0.76	48.74		
z022JB10-5	4.9	0.3	112.2	140.0	0.9	3.0	0.79	56.52		
z022JB10-6	5.5	0.3	269.5	147.7	0.8	6.9	0.76	49.08		
Average age	7.5	2.8								
z023JB10-1*	34.6	2.1	198.0	156.3	1.8	35.3	0.80	61.51	37.935	-117.651
z023JB10-2	9.2	0.5	260.8	149.2	0.9	10.8	0.74	45.23		
z023JB10-3	7.3	0.4	252.7	155.2	0.6	8.2	0.73	42.45		
z023JB10-4	10.0	0.6	200.7	143.3	1.0	9.4	0.74	45.57		
z023JB10-5*	42.5	2.5	1284.5	285.5	1.5	223.2	0.72	40.51		
z023JB10-6*	12.5	0.8	181.0	115.8	0.5	10.3	0.73	43.57		
Average age	8.8	1.4								
z024JB10-1	17.2	1.4	392.8	385.1	1.4	34.0	0.76	49.14	37.929	-117.638
z024JB10-2	18.0	1.4	807.6	1508.5	2.5	86.3	0.76	51.72		
z024JB10-3	17.4	1.4	652.8	568.8	1.4	59.1	0.80	60.48		
z024JB10-4	16.6	1.3	369.8	372.0	1.6	30.9	0.75	48.53		
z024JB10-5	18.4	1.1	742.0	630.3	1.2	69.2	0.78	55.48		
z024JB10-6*			0.3	0.4	0.0	39.4	0.74	46.14		
Average age	17.5	0.7								
z025JB10-1	5.8	0.5	6.5	26.1	28.9	0.3	0.83	72.46	37.923	-117.648
z025JB10-2	5.9	0.5	4.5	16.2	25.3	0.2	0.86	93.34		
z025JB10-3	5.5	0.4	5.4	20.2	31.1	0.2	0.78	57.77		
z025JB10-4	6.0	0.5	5.3	19.3	23.5	0.3	0.83	76.01		
z025JB10-5	7.7	0.6	3.6	15.8	20.1	0.2	0.74	46.62		
z025JB10-6	8.5	0.7	65.7	29.5	0.5	2.3	0.70	38.42		
Average age	6.6	1.2								
z026JB10-1	6.9	0.6	201.7	120.9	0.9	6.3	0.73	43.20	37.922	-117.655
z026JB10-2	5.3	0.4	278.6	301.1	1.1	7.5	0.76	49.99		
z026JB10-3	6.3	0.5	1439.2	2040.1	3.6	47.5	0.73	43.43		
z026JB10-4	6.4	0.5	616.7	632.9	1.6	19.2	0.72	42.49		
z026JB10-5	5.4	0.4	309.2	282.2	0.7	8.2	0.74	45.76		
z026JB10-6	7.5	0.6	994.9	1278.9	1.0	36.1	0.68	37.10		
Average age	6.3	0.9								

Table 5 continued: Zircon (U-Th)/He ages from the upper plate of the WHMCC. Samples marked with an asterisk were omitted in average age calculations due to the grain fracturing whenever it was unpacked from platinum after being heated by a laser. The loss of grain fragments after determining the helium concentration result in only a fraction of the parent isotopes of the complete grain being accounted for by analysis on the ICP-MS, resulting in an older age than the true ZHe age. Aliquots that represent inheritance from an older source are also omitted from average ZHe ages.

Sample	Age, Ma	err., Ma	U (ppm)	Th (ppm)	147Sm (ppm)	He (nmol/g)	Ft	ESR	Latitude	Longitude
z027JB10-1*	82.2	6.6	315.2	148.1	0.7	107.0	0.69	36.32	37.913	-117.695
z027JB10-2	7.3	0.6	87.3	54.8	0.6	2.7	0.69	36.42		
z027JB10-3	12.9	1.0	224.6	299.3	2.0	16.0	0.78	55.71		
Average age	10.1	3.9								
z028JB10-1	6.6	0.5	1116.5	1447.0	1.0	37.7	0.73	44.46	37.914	-117.694
z028JB10-2	6.2	0.5	886.5	1005.5	1.0	29.0	0.77	51.58		
z028JB10-3	4.6	0.4	921.0	828.3	0.9	20.9	0.75	47.68		
z028JB10-4	5.2	0.4	590.9	641.4	7.5	15.9	0.76	50.02		
z028JB10-5	6.4	0.5	1112.6	1338.1	2.8	38.0	0.77	52.96		
z028JB10-6	7.0	0.6	1042.1	1375.3	3.0	41.4	0.80	60.96		
Average age	6.0	0.9								
z029JB10-1	11.6	0.7	182.0	198.5	2.0	10.3	0.72	42.47	37.906	-117.651
z029JB10-2	10.5	0.6	171.3	189.4	1.6	9.8	0.81	62.79		
z029JB10-3	12.8	0.8	156.9	187.6	1.6	10.0	0.72	42.19		
z029JB10-4	12.1	0.7	216.3	263.0	2.6	14.0	0.77	52.81		
z029JB10-5*	8.4	0.5	80.0	54.6	0.9	3.3	0.78	54.43		
z029JB10-6	11.4	0.7	523.5	370.4	2.4	29.1	0.77	52.50		
Average age	11.7	0.9								
z030JB10-1	6.6	0.5	106.0	211.6	2.3	4.2	0.75	48.44	37.905	-117.651
z030JB10-2	8.0	0.6	72.1	196.1	2.4	3.5	0.69	38.74		
z030JB10-3*	10.4	0.8	73.1	244.4	7.1	5.6	0.75	49.81		
z030JB10-4	7.7	0.6	75.6	192.7	2.0	3.7	0.73	45.33		
z030JB10-5	7.3	0.6	77.1	159.7	2.6	3.5	0.77	52.31		
z030JB10-6	6.9	0.6	81.7	202.9	1.8	3.5	0.72	43.08		
Average age	7.3	0.5								
z031JB10-1	8.1	0.6	438.0	323.1	2.3	18.9	0.71	39.98	37.910	-117.639
z031JB10-2	8.7	0.7	450.0	270.4	1.8	18.0	0.72	41.36		
z031JB10-3	9.0	0.7	314.6	215.4	2.2	11.7	0.73	43.95		
z031JB10-4	9.5	0.8	300.1	207.5	1.5	15.7	0.80	60.63		
z031JB10-5	9.6	0.8	449.0	710.5	5.1	22.2	0.70	39.47		
z031JB10-6	10.4	0.8	343.9	266.3	2.3	14.5	0.76	50.14		
Average age	9.0	0.6								

Table 5 continued: Zircon (U-Th)/He ages from the upper-platel of the WHMCC. Samples marked with an asterisk were omitted in average age calculations due to the grain fracturing whenever it was unpacked from platinum after being heated by a laser. The loss of grain fragments after determining the helium concentration result in only a fraction of the parent isotopes of the complete grain being accounted for by analysis on the ICP-MS, resulting in an older age than the true ZHe age. Aliquots that represent inheritance from an older source are also omitted from average ZHe ages.

Sample	Age, Ma	err., Ma	U (ppm)	Th (ppm)	147Sm (ppm)	He (nmol/g)	Ft	ESR	Latitude	Longitude
z033JB10-1	22.3	1.3	493.6	418.3	2.4	54.6	0.76	50.46	37.880	-117.603
z033JB10-2	23.3	1.4	436.2	408.3	2.9	47.8	0.71	40.76		
z033JB10-3	23.7	1.4	512.9	561.1	1.6	64.0	0.78	53.85		
z033JB10-4	25.4	1.5	463.2	403.8	0.9	54.8	0.72	41.38		
z033JB10-5	24.8	1.5	616.9	543.6	7.1	73.9	0.74	45.82		
z033JB10-6	22.7	1.4	348.4	283.8	2.1	40.1	0.79	56.48		
Average age	23.7	1.2								

Table 5 continued: Zircon (U-Th)/He ages from the upper plate of the WHMCC. Samples marked with an asterisk were omitted in average age calculations due to the grain fracturing whenever it was unpacked from platinum after being heated by a laser. The loss of grain fragments after determining the helium concentration result in only a fraction of the parent isotopes of the complete grain being accounted for by analysis on the ICP-MS, resulting in an older age than the true ZHe age. Aliquots that represent inheritance from an older source are also omitted from average ZHe ages.

is restricted to the Weepah Road Canyon locality.

Turtleback Badlands

In the Turtleback Badlands area, only the upper unit of the Lone Mountain group is exposed. Both outcrops of the polymict conglomerate in this area are bounded at the base by high-angle normal faults that dissect and repeat the Tertiary stratigraphy in the western domains of the WHMCC (Figure 14). Interbedded lithic-rich epiclastic tuffs were collected from both high-angle fault bounded outcrops of the folded polymict conglomerate. The interbedded tuff bounded by the northern fault zone (NFZ) yielded a ZHe age of 18.7±6.3 Ma; the interbedded tuff bounded by the Alum fault zone (AFZ) yielded an age of 17.5±0.6 Ma (Figure 13). The polymict conglomerate is red with angular clasts primarily derived from carbonate rocks of the lower-Paleozoic stratigraphy. At the tip of the exposed detachment corrugation, the conglomerate appears to rest directly on the Ordovician Palmetto unit; similar to the Weepah Road Canyon, the contact between the Paleozoic section and the Lone Mountain group is everywhere covered by alluvium. Traction structures in the conglomerate and the lack of lateral continuity suggests the conglomerate was deposited in a paleo-canyon cut into lacustrine siltstone deposits. The upper contact of the red conglomerate of the Lone Mountain group is overlain by siltstone of the Weepah Hills group, indicating an unconformity with an ~7 My duration.

4.2.3 Middle to late Miocene strata

The basin sediments deposited from the middle to late Miocene are primar-

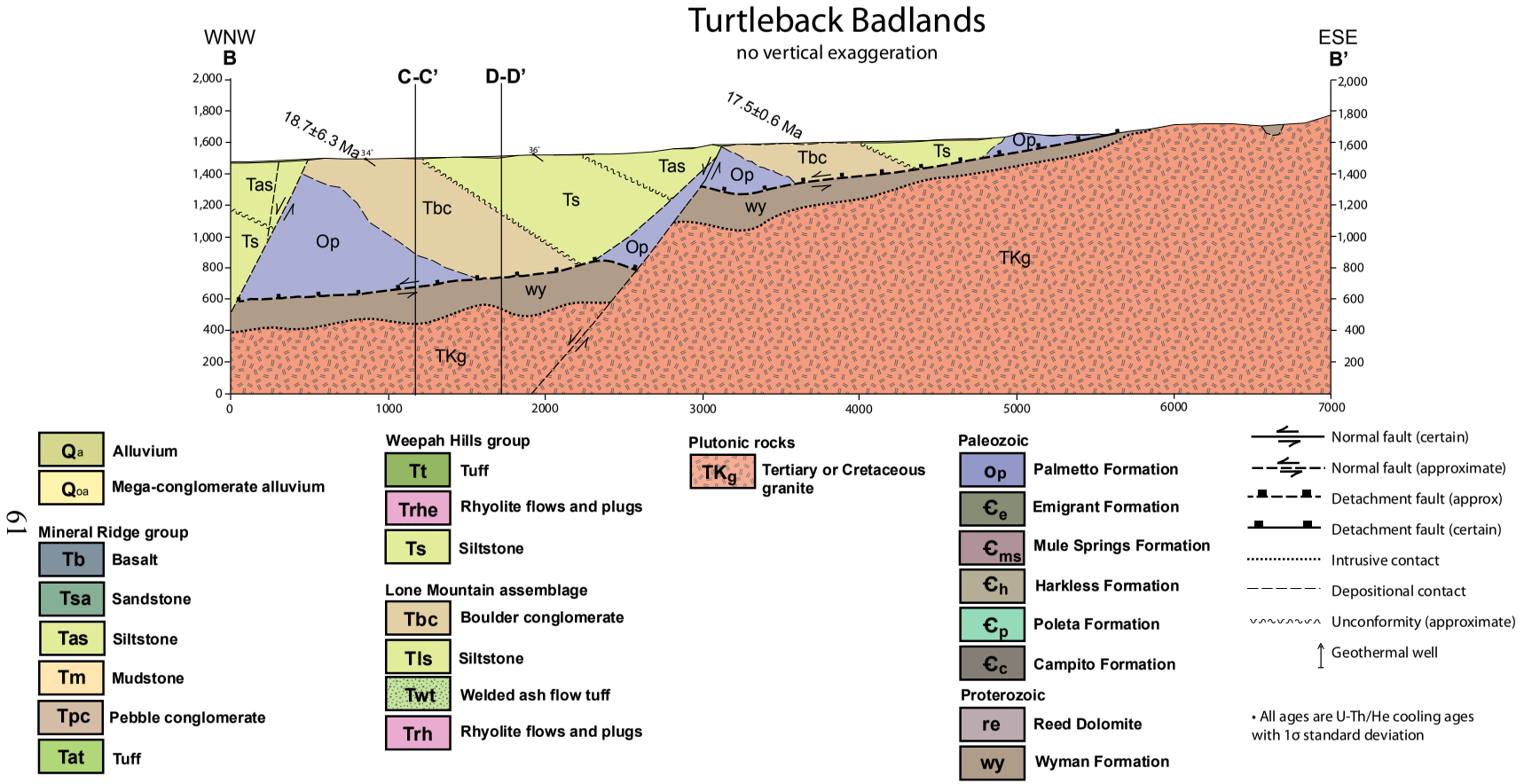

Figure 14: Schematic cross-section B-B' oriented parallel to the extension direction.

ily composed of siliciclastic lacustrine deposits that range in age from 11.3±2.0 Ma to 10.9±0.5 Ma based on ZHe ages from tuffaceous deposits (Figure 13). This package is informally referred to as the Weepah Hills group in this manuscript. The group can be divided into two lithologically distinct members. The lower member is comprised primarily of white, siliciclastic lacustrine deposits, with an interbedded vitric tuff that lies directly on the conglomerate of the Lone Mountain group. The upper member is a felsic ash-flow tuff in depositional contact with the underlying siltstone. The lower member varies from ~300-600 m of exposed section and the upper member pinches out from ~60 m in the Alum Mine Flats to zero in the Turtleback Badlands. The rocks of the Weepah Hills group are bounded at their base by high-angle normal faults, placing the sediments in fault contact with the overlying Weepah Hills group in many localities. In other areas, the Weepah Hills group rests unconformably on the upper members, both siltstone and conglomerate, of the Lone Mountain group. In both the Turtleback Badlands and the Alum Mine Flats areas, the Weepah Hills group crops out in two fault bounded segments of the Tertiary section.

Turtleback Badlands

The siliciclastic lacustrine deposits form the base of the Weepah Hills group in the Turtleback Badlands in unconformable contact on the conglomerate of the Lone Mountain group. In the section between the NFZ and AFZ, a vitric tuff is interstatified in the basal siltstone. The tuff was dated in this study at several localities by ZHe, yielding ages of 11.0±2.9 Ma, 11.1±2.4 Ma, 11.2±1.9 Ma, and 10.0±1.1 Ma (Figure 13). The vitric tuff

pinches out along strike to the northeast, with the Lone Mountain group being directly onlapped by siltstone that varies in thickness from ~600-450 m. Further east in the Tertiary section between the AFZ and the detachment, the vitric tuff does not crop out, due to burial by older alluvium (Qoa). Older alluvium also buries the lower and upper contact of the Weepah Hills group in this section. The white siltstone is the upper member of the group in this domain, that is inferred to be capped by an unconformity based on a discrete break in ZHe data (Figures 5 and 12).

Alum Mine Flats

In the Alum Mine Flats, both segments of the repeated Tertiary section yield important thermochronologic data. The section exposed between the NFZ and AFZ is the southern, along-strike continuation of the siltstone exposed in the Turtleback Badlands domain. The exposed siltstone is ~300 m thick in the Alum Mine Flats section, and is depositionally overlain by a thin bedded sequence of pebble conglomerate and siltstone ~25 m thick (Figure 12). The intercalated section of conglomerate and siltstone is capped by a felsic ash-flow tuff, dated with ZHe at 10.9±0.5 Ma. The ash-flow tuff pinches from ~60 m to 0 m along strike to the northeast in the Turtleback Badlands. The felsic ash-flow tuff is the upper member of the Weepah Hills group, forming the youngest unit of the Weepah Hills group.

The section exposed to the southeast in Alum Mine Flats, in the footwall of the AFZ, is also composed primarily of siltstone. The felsic ash-flow tuff forming the top of the section exposed between the NFZ and AFZ is absent in this section. Felsic vitric ig-

nimbrites interbedded in the siltstone were sampled and dated, yielding ages of 11.6±0.6 Ma and 11.3±0.2 Ma, the same age as the vitric tuff forming the base of the Weepah Hills group in the Turtleback Badlands (Figure 13). The upper stratigraphy of the Weepah Hills group in the southeastern block of the Alum Mine Flats is dominated by siltstone, with thin (~0.5 m) intercalated beds of mudstone and fine-grained sandstone. Alluvium in the southeast Alum Mine Flats domain covers a majority of the folded Tertiary section. Lateral thickness variations are large and thermochronologic data enhance stratigraphic correlation. Nonetheless, the unconformity bounding the top of the Weepah Hills group is poorly constrained due to the lack of tuffaceous deposits cropping out in the southeastern Alum Mine Flats.

4.2.4 Late Miocene strata

The late Miocene basin sediments comprise the upper-most unconformity bounded sequence of the WHMCC stratigraphy. This package is informally referred to as the Alum group in this manuscript. The group can be divided into two lithologically distinct members. The Alum group is comprised of a diverse succession of interbedded upper Miocene volcanic, clastic, and epiclastic tuffaceous deposits, with along-strike variations in thickness. The ZHe ages range from 5.7±0.1-7.3±0.9 Ma, with a younging trend up-section for both epiclastic and volcaniclastic sediments (Figure 13). The Alum group can be divided into two formations, the Alum Mine formation and the Monocline formation. The Alum Mine formation is the only portion of the Tertiary section that crops out in all

five domains of the WHMCC. The Monocline formation is limited to one domain and records the youngest volcanic deposits of the WHMCC. The two formations do not record a distinct temporal break, but rather are differentiated based on the folding in the Alum Mine formation and the undeformed beds in the Monocline formation.

4.2.4.1 9 Ma to 6 Ma sedimentary package

Alum Mine Flats

In the Alum Mine Flats domain, the stratigraphy of the Alum Mine formation is disrupted by northwest-dipping high-angle normal faults. The formation crops out in three tilted fault blocks with beds dipping to the southeast (Figure 15). In the block northwest of the NFZ, only the top of the Alum Mine formation is exposed. Thin beds of quartzofeldspathic arenite in a moderately-sorted pebble conglomerate constitute the upper units of the Alum group. The conglomerate has a sand matrix, identical to the interbedded sandstone, which supports clasts of primarily chert and volcanic constituents. An interbedded tuffaceous siltstone was sampled from the base of the section, and yielded a ZHe age of 7.4±1.6 Ma (Figure 13). This serves as a marker bed, and in the top of the section between the Alum and Northern fault zones.

This section of the Alum Mine formation bounded by the AFZ and NFZ is comprised of white to yellow siltstone at its base, displaying variable tilting across the section ranging from 30-45 degrees. A depositional contact separates the basal siltstone from the overlying matrix-supported pebble conglomerate. The conglomerate has a matrix of fine-

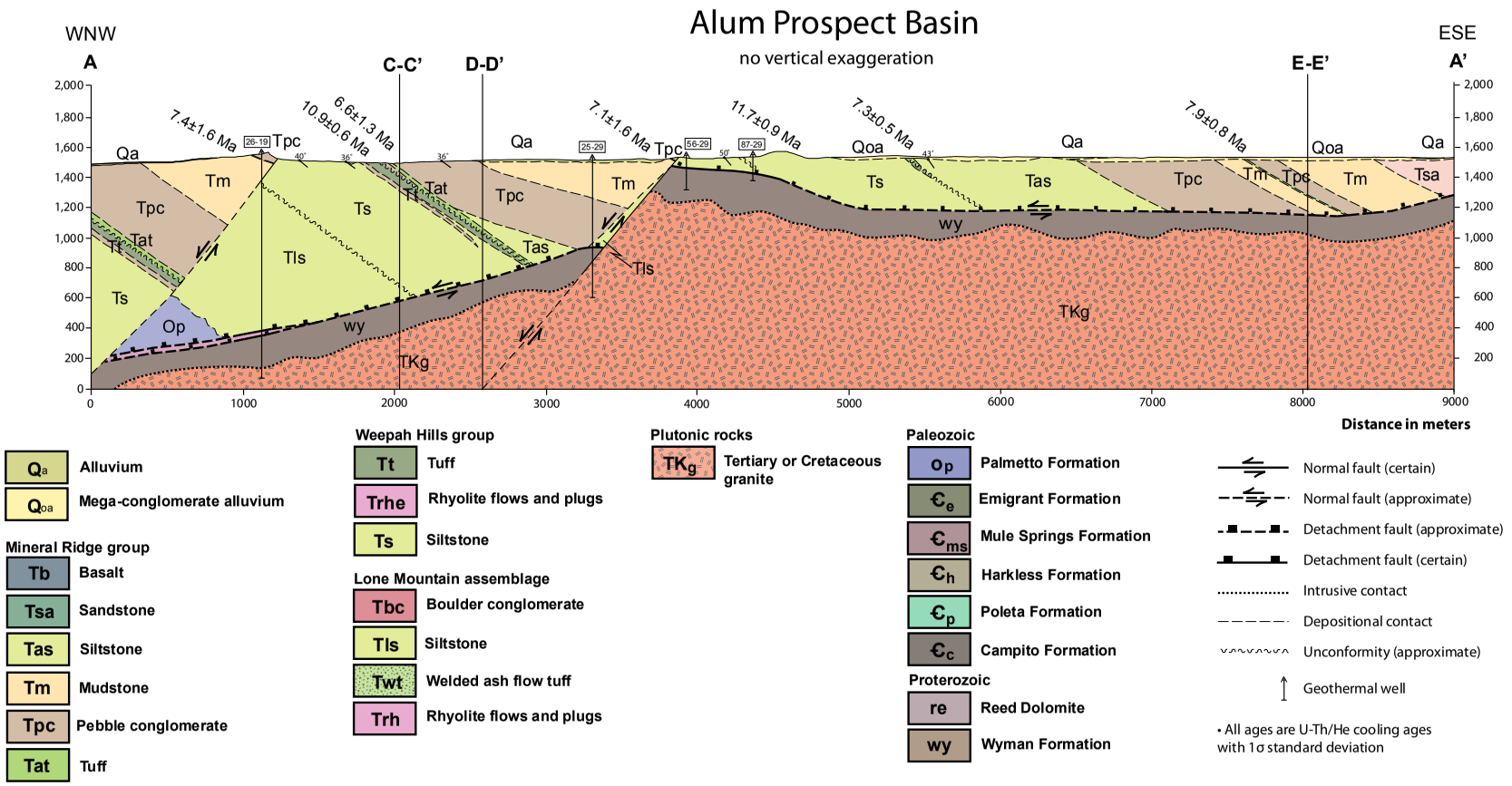

Figure 15: Schematic cross-section A-A' oriented in the direction of extension.

grained quartzofeldspathic wacke and clasts primarily of volcanic origin. Thin beds of tuffaceous siltstone, with volcanic clasts of varying composition, are present throughout the conglomerate sediments. A thin intercalated lithic-rich tuff, dated by ZHe at 6.6±1.3 Ma, forms the boundary with the upper segment of the wacke supported conglomerate. The conglomerate has a depositional contact with an overlying mudstone that is marked by laterally discontinuous thin interbeds of conglomerate similar in composition to the unit below.

The mudstone is temporally constrained by ZHe ages from units conformably bounding above and below. The mudstone, similar to the lower Alum group, pinches out toward the northeast while transitioning into the type of slightly coarser-grained siltstone that dominates the stratigraphic column of the Alum Mine formation in the Turtleback Badlands area. The mudstone is capped by a 7.1±1.5 Ma tuffaceous siltstone that correlates to the unit sampled at the base of the section in the fault block northwest of the NFZ (Figures 16 and 17). As near the northwestern fault block, the tuffaceous siltstone is overlain by the pebble conglomerate, forming the top of the Alum group in the Alum Mine Flats domain.

Turtleback Badlands

The Turtleback Badlands record the transition of the Alum Mine formation from a lithologically diverse section to a stratigraphy comprised solely of siltstone. Three units crop out in the southeastern Turtleback Badlands area that temporally and compositionally correlate with the better exposed Alum Mine formation in the Alum Mine Flats. The

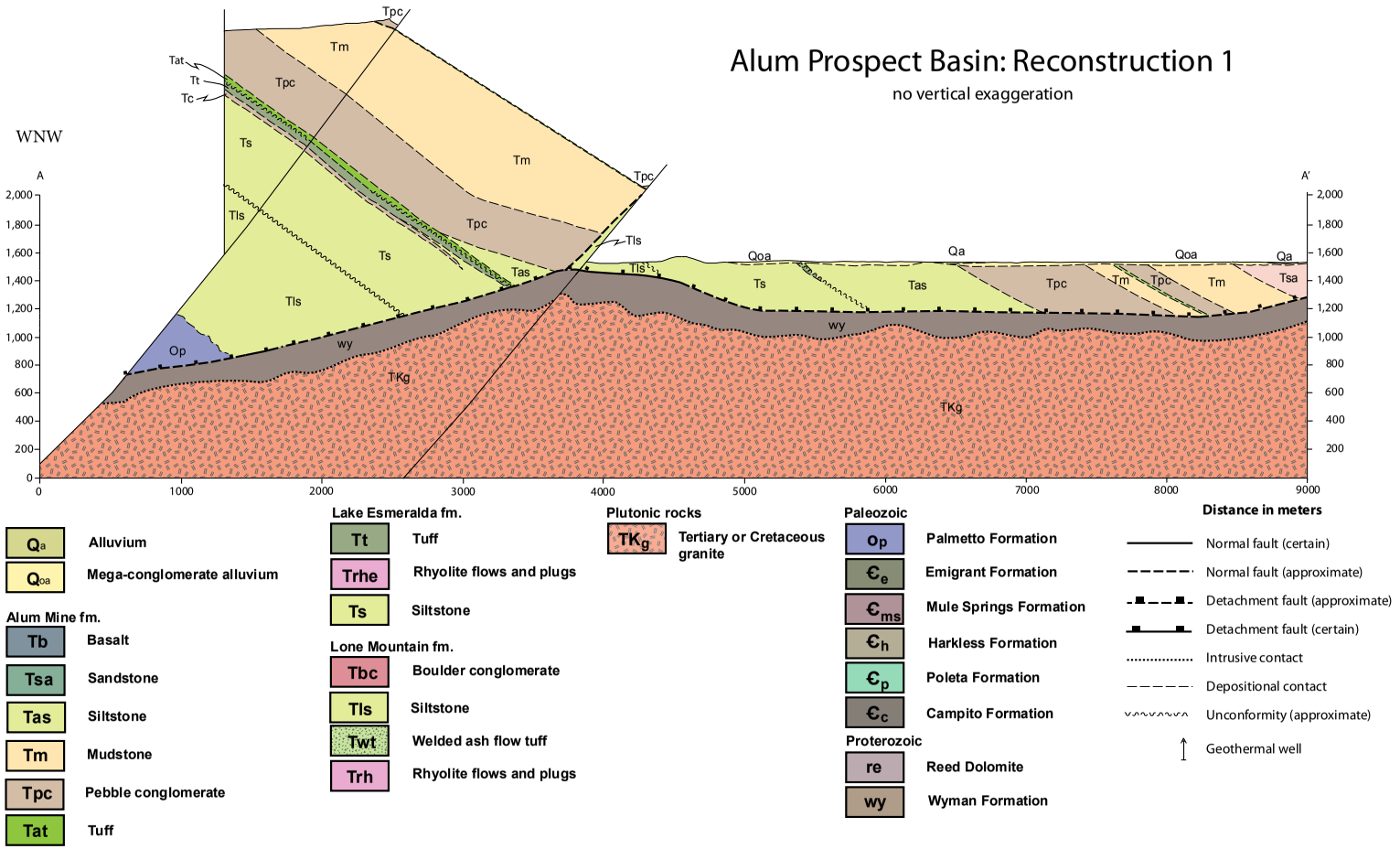

Figure 16: Reconstruction of ~1 km of slip along Mio-Pliocene high-angle normal faults.

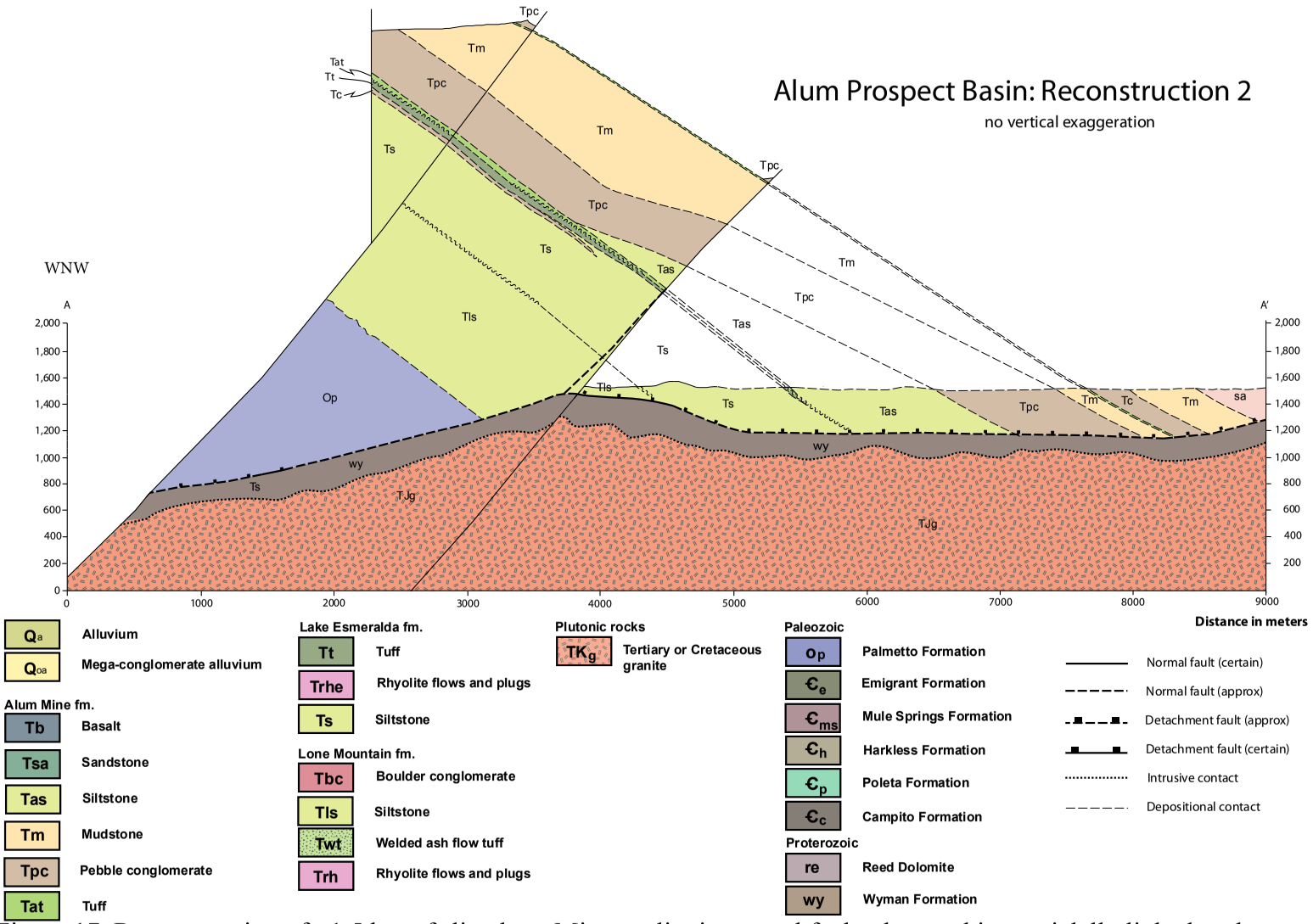

Figure 17: Reconstruction of ~1.5 km of slip along Miocene listric normal faults that are kinematiclally linked to the detachment.

basal ash-flow tuff is dated at 7.2±0.9 Ma, 7.5±2.7 Ma and 7.2±0.4 Ma (Figure 13). The tuff unconformably overlies the siltstone of the Alum group. A single outcropping tuff was dated from the middle of the section, yielded an age of 6.5±0.3 Ma. The stratigraphy at the top of the section is dominated by mudstone, with a thin bed of tuffaceous siltstone dated at 6.3±0.8 Ma. The mudstone is bounded at the top by the AFZ. The two tuffaceous deposits and the mudstone pinch out to the northeast, where the stratigraphy in the north-east Turtleback Badland area is entirely comprised of siltstone that unconformably overlies the siltstone of the Alum group and is in fault contact with the same unit at its upper bounds.

Contour Tuff Canyon and Weepah Road Canyon

The oldest ZHe ages for the Alum Mine formation from the five domains were obtained for samples from the Contour Tuff Canyon and Weepah Road Canyon areas. In these two areas, a near-flat-lying ash-flow tuff, herein referred to as the contour tuff, crops out in the corrugation troughs of the lower plate to the west and directly south of the larger lower plate corrugation in the Weepah Hills. The tuff correlates in age to the base of the Alum Mine formation, but differs from the rest of the stratigraphy because it is not tilted by the high-angle normal faults that offset the rest of the exposed Alum Mine formation. In the contour tuff canyon, the tuff is dipping at 5° toward the detachment, and yielded a ZHe age at 8.2±1.9 Ma (Figure 5) (Table 3; sample 10CP006). The tuff is bounded at its base by an angular unconformity underlain by siltstone believed to be part of the Weepah Hills group, and is overlain by older Quaternary alluvium (Qoa). In the

Weepah Road Canyon, the contour tuff caps exposures of Cambrian and Paleogene rocks that have been offset by the older generation of high-angle normal faults. Similar to the western locale, the gently dipping bed is buried by Qoa. The lower contact is also buried, but a ZHe age of 8.7±1.6 Ma temporally correlates the two outcrops (Figure 5).

4.2.4.2 6 Ma TO 5 Ma SEDIMENTARY PACKAGE

Monocline Ridge

The Alum group is capped by the Monocline formation exposed in the Monocline Ridge domain of the southern map area. The lower 110 m of the monocline consists predominately of sandstone, with thin beds of sand sized matrix-supported conglomerate with beds of siltstone. The conglomerate is composed of fine-grained wacke matrix and clasts primarily of volcanic origin, with a small percentage of chert clasts. The interbedded sandstone is composed of thin-bedded, well-sorted quartzofeldspathic arenite. These units correlate to the upper units of the Alum Mine formation. A porphyritic basalt caps the stratigraphy of the monocline and is bounded on both sides by felsic ash-flow tuffs dated at 5.9±0.2 Ma and 5.7±1.8 Ma by ZHe (Figure 13).

4.3 KEY STRUCTURES OF BASIN SEDIMENTS

Miocene rocks comprising the basin sediments of the Weepah Hills preserve a record of deformation and sedimentary structures that can be tied both spatially and

temporally to the detachment corrugation. Nearly all of the Tertiary section exhibits folding (Figure 18, 19 and 20), with packages of folded strata subsequently cut by high-angle normal faults and dextral transurrent faults active since the latest Miocene (Figures 14 and 15). Evidence of a progressive unconformity and onlap surfaces aid in the Alum Mine formation constraining the timing of folding and deposition of basin sediments (Figure 21). The preserved structure and sedimentological relationships of basin sediments spanning the transition from various extensional faulting regimes provides critical insight to complex basin evolution and the bounding structures active during deposition of sediment packages.

4.3.1 Generations of Cenozoic Faulting

The rocks exposed in the WHMCC record three generations of Cenozoic normal faulting (Figure 2). The earliest episode of normal faulting was related to Basin and Range style extension. This period is followed by transtension that initiated during the late Miocene, derived from strike-slip faults of the eastern California shear zone. This strain is associated with both late Miocene detachment faulting and Mio-Pliocene high-angle normal faulting linked to transcurrent faults accommodating strain across the SPLM extensional system. Temporal constraints on these structures are primarily based on sedimentological and stratigraphic relationships due to the burial of direct cross-cutting relationships between fault systems (Figure 5).

The earlier extension in the WHMCC was accommodated by slip along normal

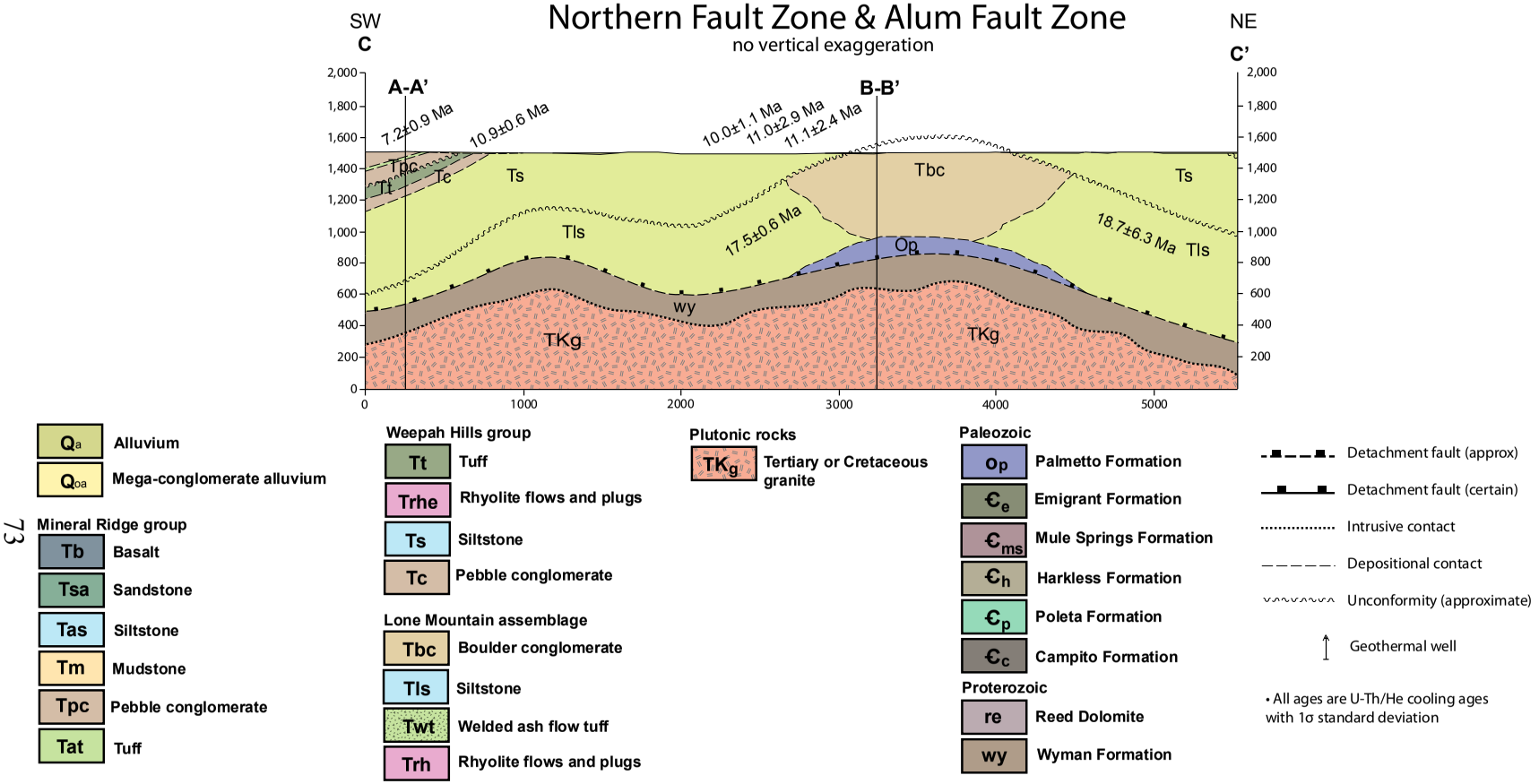

Figure 18: Schematic cross-section C-C' oriented perpendicular to the direction of extension.

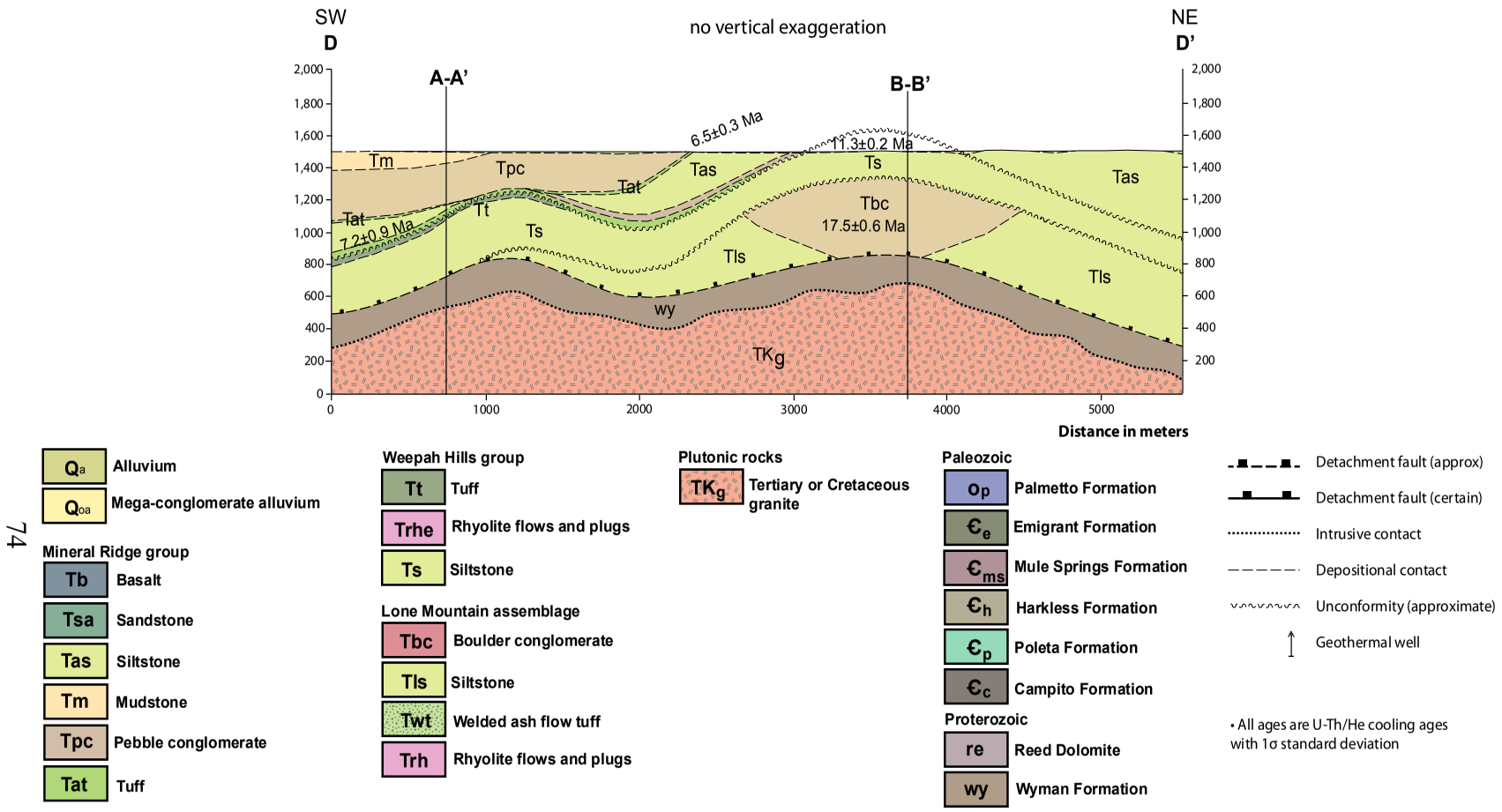

Figure 19: Schematic cross-section D-D' oriented perpendicular to the direction of extension.

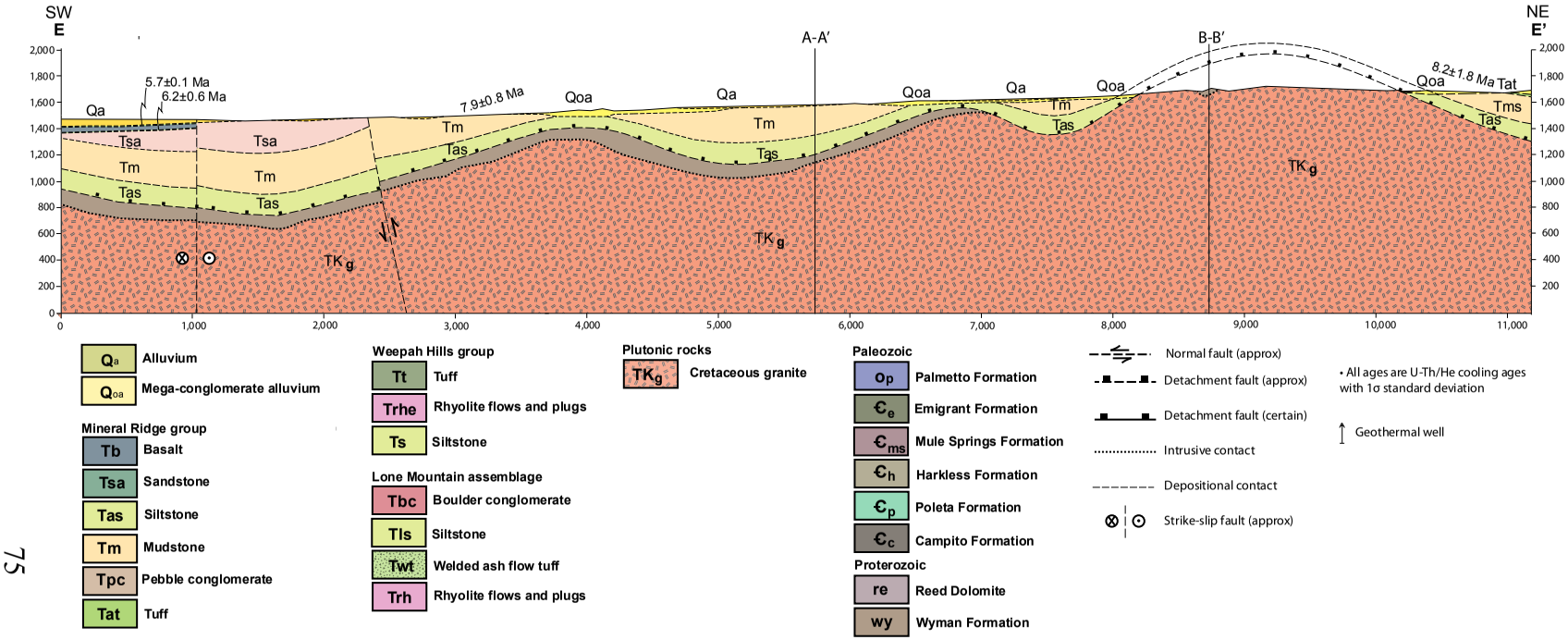

Figure 20: Schematic cross-section E-E', oriented perpendicular to the extension direction.

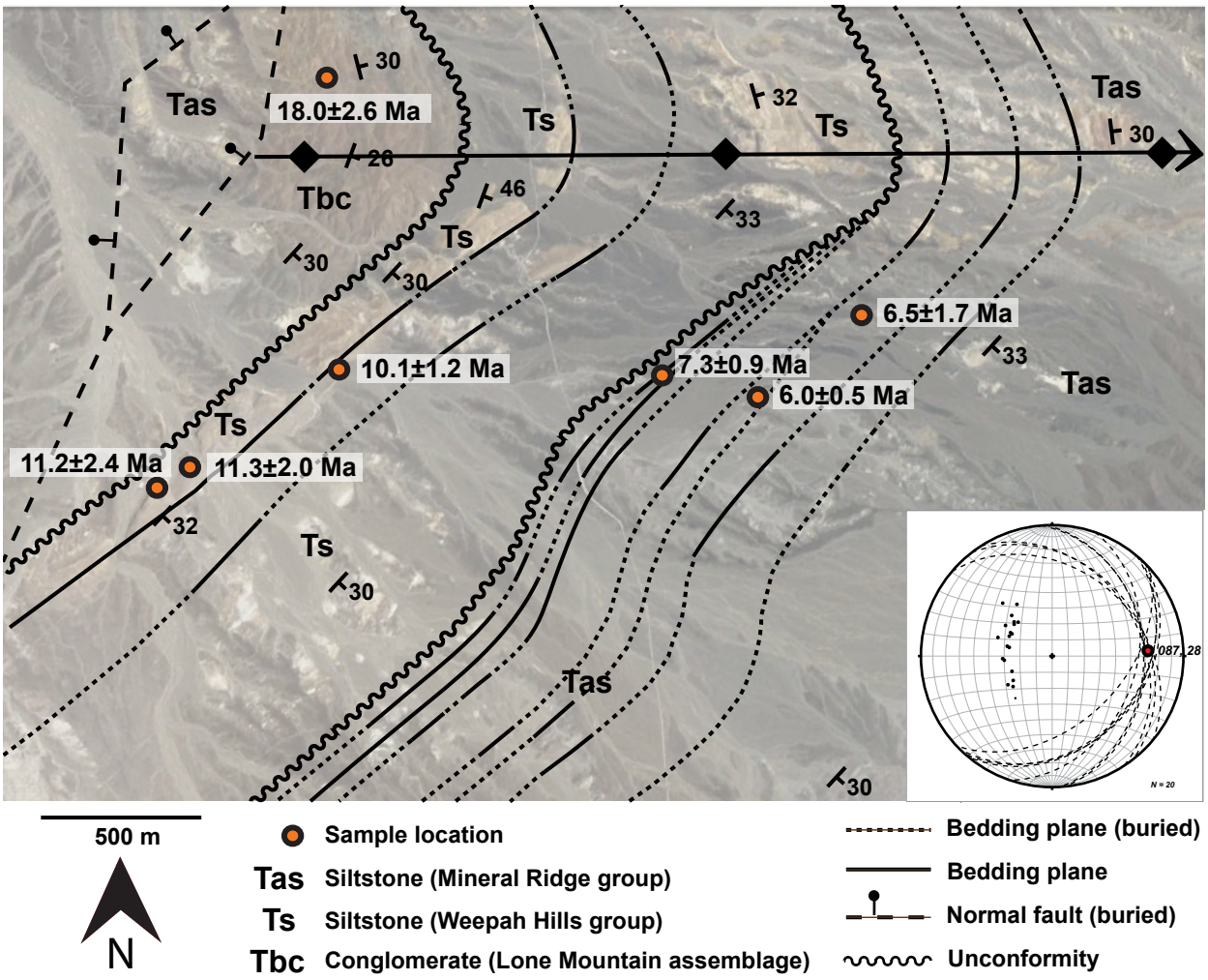

Figure 21: Outlined onlap surfaces defining a progressive unconformity in the basin sediments of the upper plate of the detachment. Bedding plane orientations from basin sediments are plotted ont the inset stereonet plot. Bedding and the progressive unconformity are anticlinally folded, with a fold axial plane trending 087. Unconformities are interpreted based on zircon (U-Th)/He ages shown with 1σ standard deviation. Image is digital orthophoto from the U.S.G.S. National Map viewer (http://nationalmap.gov/viewer.html). Stereonet made using Stereonet 8 software (Allmendinger et al., 2012).

faults active during the early to middle Miocene. This normal fault system is associated with Basin and Range extension well documented across western Nevada. Normal faults accommodate extension and exhibit ~25˚ rotation in the uplifted blocks (Dilles and Gans, 1995; Stewart, 1998; Surpless et al., 2002 Stockli et al., 2003). The kinematics of the earlier normal faults is poorly constrained in the WHMCC due to the burial of the fault planes by alluvium. The geometric constraints on these structures are based on the outcropping pre-Miocene stratigraphy in the WHMCC. The older normal faults are only exposed in the Weepah Road Canyon area of the WHMCC, where disarticulation by later faulting is minimal (Figure 4). In this area, the older normal fault systems of the WHMCC dip to the southwest, dissecting the lower Paleozoic miogeocline section and overlying Oligocene tuffs forming a half-graben geometry. The amount of uplift and slip rates along the older normal faults in the WHMCC is unknown due to a lack of chronologic or structural data resulting from burial by Quaternary alluvium. The normal faults that dissect the pre-Miocene stratigraphy are capped by an angular unconformity with the contour tuff unit of the Alum group, interpreted on the basis of ZHe ages to be deposited above the detachment.

The type-locality of the detachment fault bounding the Weepah Hills pluton is in the Turtleback Badlands area of the WHMCC. At this locality, the detachment places Ordovician Palmetto on the Wyman Formation, at a dip of 15° NW. The corrugated detachment fault at this latitude defines an antiform that trends N85W and plunges northwest. A smaller anticline of lower plate tectonites is exposed due east of the Monocline,

and is suggested to be a lesser corrugation of the detachment based on analogous lithologies and ZHe dating. This exposure, termed the “whaleback”, defines a doubly plunging antiform that trends N80W. Assuming a geothermal gradient of 25˚C/km, thermochronometric constraints from the plutonic rocks of the lower plate suggest a rate of exhumation between 0.5-1.6 mm/yr based depth constraints from ZHe and AHe ages . There is also evidence of high-angle listric normal faults that are kinematically linked to the detachment fault (Figures 14, 15 and 17). These faults attenuate the upper plate as the basin sediments are extended during exhumation along the detachment. Several observations suggest these structures although they are not presently exposed. Various amounts of tilting in lower section of supradetachment sediments (~8 Ma) suggest the sediments were rotated along later syndetachment faults or later Mio-Pliocene faults. Well constraints on the dip of the detachment suggest that minimal (<5˚) horizontal axis rotation has occured along the Mio-Pliocene structures, suggesting that the difference in tilt is due to rotation along syndetachment structures. Reconstructing the A-A’ section line concludes that these faults had ~1.5 km of offset (Figure 17). Syndetachment listric faults are commonly seen in the upper plate of detachment faults as a result of extension causing exhumation of the lower plate along the detachment (e.g. Friedman et al., 1996; Dorsey and Becker, 2005; Davis and Friedman, 2005). The transtension linking the ECSZ and Walker Lane is also responsible for driving transcurrent and high-angle normal faulting of Mio-Pliocene age.

The younger episode of high-angle normal faulting, following detachment faulting, is driven by transtension derived from major dextral strike-slip fault systems of the

ECSZ. The high-angle normal faults currently serve as the major range bounding faults of the SPLM extensional system, and are kinematically paired with dextral transcurrent faults. These two faulting regimes work in tandem to accommodate strain across the WHMCC and SPLM from the latest Miocene through the Holocene. The kinematic relationship between the detachment and younger high-angle normal faults is unclear because of a lack of age control. The detachment has been proposed by previous researchers to be kinematically linked to the younger episode of high-angle faulting, with high-angle faults soling into the detachment at depth (Oldow, 2003). This study proposes that detachment faulting was active in a late Miocene hiatus between the episodes of high-angle faulting, temporally bracketed by accommodation of extension and transtension along faults of higher angles that offset the detachment by ~1 km (Figure 16). This hypothesis is supported by depth constraints on the detachment fault obtained from drilling log records from geothermal exploration wells in the hanging and footwall blocks of the high-angle Alum Fault Zone (AFZ). With the applied subsurface data on detachment depth, an unrealistic geometry of detachment faulting is necessary to kinematically tie the low and high-angle systems. It is a more reasonable geometry if the detachment is structurally elevated in the footwall block of the AFZ due to offset along a high-angle fault of the AFZ (Figure 22). Collaborators from the University of Oklahoma are currently working to image the subsurface in the Alum Mine Flats area of the WHMCC using geophysical techniques to resolve the relationship between high-angle and the detachment.

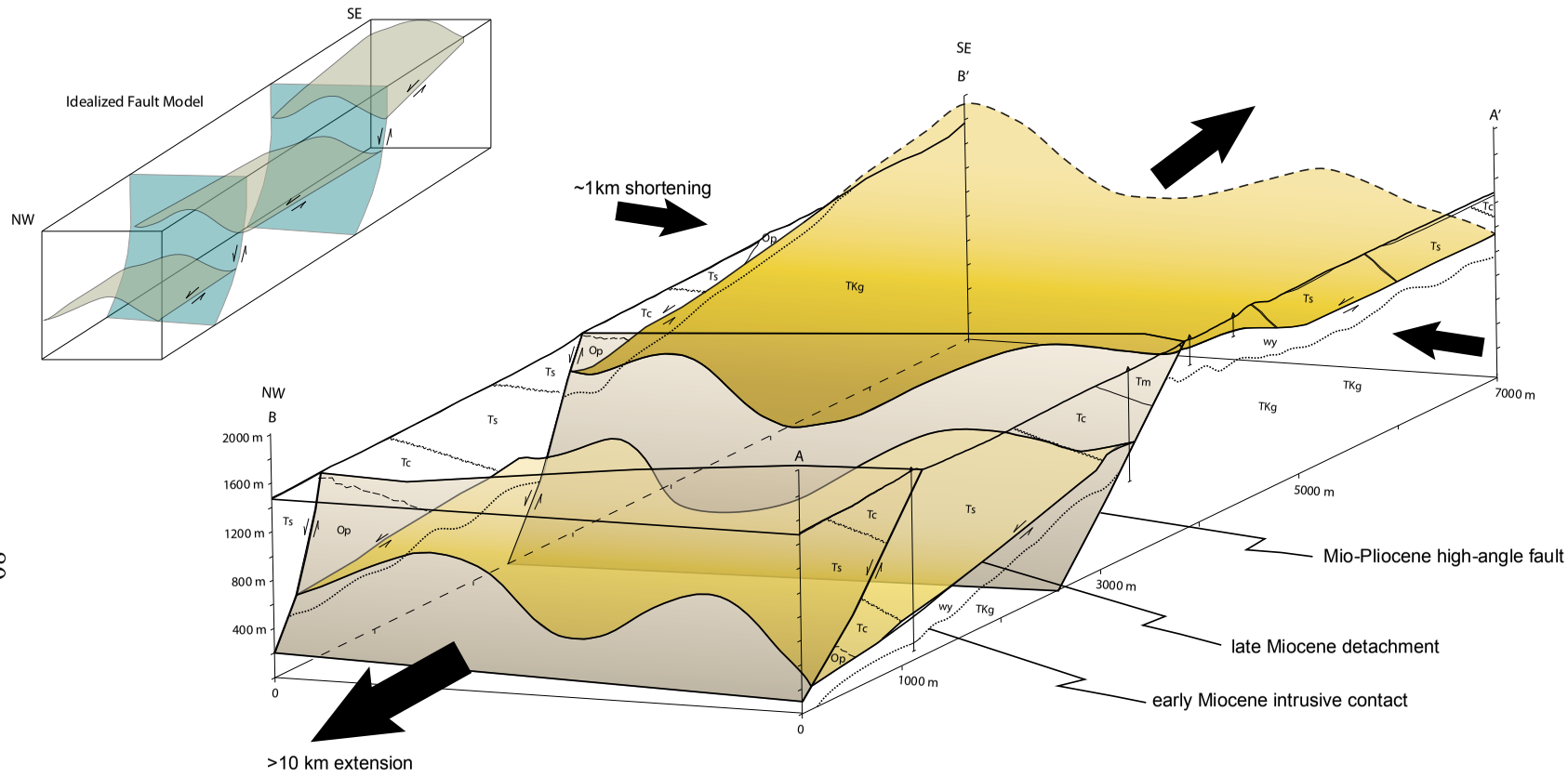

Figure 22: Diagram of the relationship between detachment faulting and later Mio-Pliocene high-angle faulting. Simplified cross-sections in the direction of extension constrain the sides of the diagram.

4.3.2 Generations of Folding

At least two generations of folds altered the rocks of the WHMCC. The older generation of folding best exposed in the lower Paleozoic section outcropping in the Weepah Road Canyon. Folding of the lower Paleozoic strata is attributed to shortening during the mid-Paleozoic and early Mesozoic (Oldow, 1984). The later generation of folding is associated with the antiformal corrugations that define the geometry of low-angle normal faults. The development of these extension parallel features is highly debated (e.g. Davis and Lister, 1988; Spencer and Reynolds, 1991; Mancktelow and Pavlis, 1994). Most recently, Singleton (2011) concluded the corrugations are folds generated during extension perpendicular shortening during the waning stages of detachment activity. The evidence for this conclusion was folded lineations on the detachment plane and normal faults suggesting outer-arc extension in the hinge of the corrugations (Singleton, 2011). Folding of the upper plate rocks of the WHMCC suggests the corrugations are in fact folds that develop during active detachment faulting.

The younger generation of folding in the Tertiary rocks exposed in the basin sediments cropping out in the Alum Mine Flats and the Turtleback Badlands. The folds are characterized by shallowly plunging, northwest-trending fold axes. Folds are open and have half-wavelengths measuring ~2 km and amplitudes on the order of ~1 km (Figures 21 and 22). Due to the thermochronometric constraints detecting unconformities throughout the Miocene stratigraphy, it is inferred that the unconformities are folded in the same geometry as the upper plate sediments they bound (Figure 21). The Tertiary folding event

is attributed to the corrugated geometry of detachment faulting, active in the late Miocene. This is supported by spatial and temporal constraints on folding expounded upon in the discussion section. The Monocline formation of the Mineral Ridge assemblage, outcropping in the Monocline Ridge domain, is the youngest Tertiary outcrop and does not display evidence of folding. The basalt and ash flow tuff capping the section are dated at ~6 Ma, recording an upper limit for the timing of folding of strata in the upper plate. The onlap surfaces in the upper plate of the WHMCC also suggests that the corrugations are folds generated during detachment faulting, and are not solely a primary feature of detachment faults.

4.3.3 Progressive Unconformities

Progressive unconformities form in growth strata related to progressive limb rotation and record the development of folds (Verges and Burbank, 1992). Folding, growth strata and unconformities in the Lone Mountain group, the Weepah Hills group and the Alum Mine formation of the Alum group can be utilized to constrain the development of lower plate corrugations. Units composing both the Lone Mountain group and the Weepah Hills group are continuous along strike, suggesting these units were deposited prior to the initiation of folding. Further up-section, the contact between the Alum group and the Alum Mine formation is defined by a progressive unconformity, characterized by a series of onlap surfaces (Figure 21). The ash-flow tuff marking the base of the Alum Mine formation can be tracked laterally based on ZHe ages to reveal that the tuff onlaps

the underlying Weepah Hills group as it deflects along the limb of the fold until its termination prior to reaching the fold hinge. The strike of the growth strata up-section of the basal tuff reveal that towards the hinge of the unconformity, units progressively onlap the fold limb (Figure 21). The exact nature of the growth strata contacts, whether onlap or offlap surfaces, is difficult to determine due to burial of the progressive unconformity by Quaternary alluvium. This makes interpretations of variations in uplift rates based on modeled results from fold related growth strata difficult to determine (Hardy and Poblet, 1994). Regardless, the progressive unconformity, determined by the variable orientations of folded tuffaceous deposits, adds further evidence constraining the portion of stratigraphy that was deposited in a supradetachment setting.

5. DISCUSSION

By pairing the U-Pb, ZHe and AHe data for the lower and upper plates of the detachment with structural and depositional relationships in the basin sediments, a complex yet coherent account of the tectonic evolution can be extrapolated to correlate the various data sets. The Weepah Hills area records the transition from Middle Miocene Basin and Range extension to Walker Lane transtension both in the terms of the tectono-thermal evolution of exhumed middle to upper crustal rocks as well as the upper plate stratigraphic record. In light of nearly continuous magmatism (plutonic and volcanic) the area offers a very rich record for the reconstruction of the timing of faulting and syn-tectonic sedimentation and thus the temporal record of the transition from both Basin and Range to Walker Lane deformation and the transition from core-complex formation to late-stage dismemberment of the lower and upper plate by high-angle normal faulting and right-lateral strike-slip faults.

5.1 Geo- and thermochronometric constraints on footwall exhumation

U-Pb ages from the Weepah Hills distinguish two episodes of magmatism emplaced granitic intrusives (Figure 7). The Late Cretaceous event correlates to previously documented crystallization ages for plutons in the region, while the early Miocene event was previously undocumented. Tertiary igneous activity in the Walker Lane has been shown to spatially correlate with accommodation zones that kinematically link extended terrains (Axen, 1998; Faulds and Varga, 1998; Stewart, 1998), and temporally precede

major Cenezoic extension (Gans et al., 1989). The regional correlation between extension and magmatism can be applied to the WHMCC to suggest that east-west extension initiated by the early Miocene, and is associated with the younger granitic intrusion of the turtleback. ZHe ages from the granitic rocks also support early Miocene extension in the Weepah Hills.

The majority of ZHe ages from the detachment footwall yield ages older than 10 Ma, ranging from ~19-11 Ma (Figure 8). Younger ZHe ages are only recorded by two samples from the granitic footwall, documenting cooling at ~9 Ma. This suggests a progressive, two-stage thermal history experienced by the granitic rocks of the WHMCC. The granitic rocks were uplifted to ~5 km and cooled below the zircon helium retention window (~180°C) throughout the Miocene (~9-19 Ma). The temporally variable range of ZHe ages are either the result of an arched intrusive contact marking the upper bounds of the pluton, or due to tilted uplift of the pluton during Basin and Range style extension. The AHe data from the lower plate records only a single cooling event at ~8-9 Ma across the entire footwall exposure (Figure 9). The relationship between ZHe and AHe ages across the footwall can yield insight to the tectonic history and relative rates of exhumation for the granitic rocks. The ZHe ages vary across the footwall, recording late Miocene cooling associated with both steady uplift along the older generation of high-angle normal faults during early to middle Miocene east-west extension and exhumation along the detachment. AHe ages record cooling restricted to the late Miocene (~9 Ma) associated with exhumation of the exposed footwall along the detachment. Based on the

variation between ZHe and AHe ages and assuming a geothermal gradient of 25°C/km, the rate of exhumation can be estimated between 0.5-1.6 mm/year. The thermochronologic constraints on the tectonic evolution of the WHMCC can be linked to ZHe data and deformation preserved in the overlying extensional allochthon. Based on the interpreted exhumation history of the lower plate rocks and preserved upper plate deformation, the three unconformity bounded packages of basin sediments can be correlated to structures active during their deposition and that exhibit a major control on basin evolution.

5.2 Muti-stage Basin Evolution of the Weepah Hills

The depositional setting for the unconformity-bracketed Lone Mountain group and Weepah Hills group can be inferred from the temporal correlation of early to middle Miocene ZHe ages across the detachment fault. ZHe ages from the Lone Mountain group (~18 Ma) and the Weepah Hills group (~11 Ma) correlate to ZHe cooling ages related to exhumation of the granitic rocks along the older generation of high-angle normal faults during the early to middle Miocene. Folding of these units accompanied by a lack of onlap or offlap surfaces indicates deposition of the sediment before folding of the basin sediments by the corrugated geometry of detachment faulting. Based on the ZHe data and preserved depositional structures, the Lone Mountain group is interpreted to have accumulated in a paleo-canyon, while the Weepah Hills group is interpreted to represent deposition in a lacustrine system bounded by southwest-dipping normal faults active during early to middle Miocene east-west extension.

The ZHe ages for the Alum Mine formation of the Alum group correlate to granitic cooling ages, both ZHe and AHe, record exhumation by slip along the detachment. This suggests the Alum Mine formation represents sedimentation in a supradetachment setting. The contact between the Alum Mine formation and the underlying Weepah Hills group is defined by a progressive unconformity, determined by correlating beds by ZHe ages and the relative orientation of units up-section (Figure 21). The progressive unconformity in the supradetachment sediments suggest that the units of the formatin were being deposited during Tertiary folding, and that the lower plate of the detachment was actively folding as late as 6 Ma.

The ZHe ages for the Monocline formation, dated at ~6 Ma, of the Alum group post-date cooling ages in the footwall of the detachment (Table 3; samples 007JB10, 013JB10 and 445CS10). These sediments also lack evidence of folding associated with extension perpendicular shortening, but the basalt and ash flow tuffs capping the section are offset by the youngest generation of transcurrent and high-angle normal faults. The Monocline formation is thus interpreted as sedimentation immediately after the cessation of detachment faulting and the initiation of the high-angle normal faults that offset the detachment by ~1 km (Figure 16). The age constraints from the Monocline formation constrain the upper limit of detachment faulting at ~6 Ma.

5.3 Regional correlation of Miocene stratigraphy

Clastic and volcanic rocks of Miocene and Pliocene age have long been studied

in west-central Nevada, but a lack of detailed age control has led to poorly constrained regional stratigraphy. Previous regional work that encompassed the WHMCC lacked extensive stratigraphic age constraints, resulting in much of the Cenozoic sediments attributed to the Esmeralda Formation (ranging in age from ~16 Ma- 6 Ma) and misinterpreted as recording only supradetchment sediments (Robinson, 1964; Davis, 1979, Albers and Stuart, 1972; Stuart and Diamond, 1990). Diamond and Ingersoll (2010) suggested that the Weepah Hills area recorded a post-detachment sequence, but lacked age data on the overlap sequence. The Esmeralda Formation was defined by Turner (1900) and since its inception has been utilized to loosley describe many heterogenous clastic rocks of the region. The ambiguous definition of the Esmeralda Formation has grown throughout the 20th century (e.g. Ferguson et al., 1953; Robinson et al., 1968; Albers and Stewart, 1972; Stewart et al., 1974). Due to the lack of consistency and ambiguity in its use, Oldow et al., (2009) suggests the Esmeralda Formation should be abandoned in the region. This study also advocates for the abandonment of the term Esmeralda Formation in order to move forward with a more constrained and detailed stratigraphic nomenclature.

Regional correlations of the WHMCC stratigraphic record to other basins in the greater Mina Deflection area is difficult due to pronounced lateral thickness variations and poor temporal constraints on the stratigraphy (Oldow et al., 2009). Despite this, other recent studies have constrained the tectonic evolution of sedimentologically similar localities that preserve the depositional record of the Mina Deflection area (e.g. Bradley et al., 2003; Petronis et al., 2007; Oldow et al., 2009; Petronis et al., 2009; Corbin et al.,

2010). The stratigraphy exposed in the Silver Peak Range area has been the topic of detailed studies (e.g. Petronis et al., 2007, 2009; Oldow et al., 2009) that document the tectonic evolution of the southwestern portion of the SPLM extensional complex. The strata exposed in the Silver Peak Range were deposited between ~22-5.8 Ma, with substantial lateral thickness varations throughout the Miocene section due to moved along syndepositional faults (Oldow et al., 2009). The Icehouse Canyon assemblage is comprised of a basal conglomerate with clasts of Palezoic rock overlain by a rhyolite tuff dated by K-Ar at 21.5-22.8 Ma; the rhyolite tuff is capped by andesite lava, lahar and debris flows (Oldow et al., 2009). This assemblage is correlative to the Lone Mountain group in the WHMCC, where the rhyolitic tuff yielded a ZHe age of 23.7±1.2 Ma and a conglomerate comprised of Paleozoic carbonate clasts is dated by ZHe at ~18 Ma are both unconformably overlain by volcanic and clastic sediments. In the Silver Peak stratigraphy, the Icehouse Canyon assemblage is unconformably overlain by sediments of the Coyote Hole Group that represent the diverse lithologies previously termed the Esmeralda Formation (Oldow et al., 2009). The internal stratigraphy of sedimentary packages of the Esmeralda Formation varies between the Silver Peak Range and the Weepah Hills, but detailed chronostratigraphy allows for correlative packages to be determined across the two localities.

The Coyote Hole Group is subdivided into four formations: the Silver Peak Formation composed of volcano-clastic sediments dated by K-Ar at 13-11 Ma, the Rhyolite Ridge tuff dated by K-Ar at 6.9±0.9 Ma, the Cave Springs Formation composed of volcano-clastic sediments, and the latite tuffs and lavas of the Argentite Canyon with

K-Ar ages of 5.9-6.1 Ma (Oldow et al., 2009). The Silver Peak Formation of the Coyote Hole Group is correlative to the Weepah Hills group of the WHMCC in both bulk lithology and thermochronogic age constraints. The Alum Mine formation of the WHMCC area is correlative to Rhyolite Ridge tuff and the Cave Springs Formation of the Coyote Hole Group described by Oldow et al., (2009) based on thermochronologic constraints. The bulk lithology between the two localities is similar for this section of the chronostratigraphy, but the Silver Peak Range has thicker volcanic deposits than the Weepah Hills area. The Monocline formation that caps the stratigraphy in the WHMCC is correlative to the Argentite Canyon Formation of the Coyote Hole Group described by Oldow et al., (2009), both recording late Miocene volcanism in the SPLM extensional system.

5.4 Lower Plate Corrugations and Upper Plate Folding

The undulatory geometry of detachment faulting is expressed as corrugations, with wavelengths often on the order of 1 to 5 km, in the lower plate of core complexes. Corrugations are typically attributed to either extension-perpendicular shortening that generates folds in the lower plate (e.g., Yin, 1991; Mancktelow and Pavlis, 1994; Oldow et al., 2009), or interpreted as primary fault grooves present at inception of the detachment (Spencer, 1985; Davis and Lister, 1988). These two models are the most widely accepted interpretations of detachment corrugations, but other models have also been proposed that suggest folding may be a result of displacement gradients along normal faults (Schlische, 1995; Kapp et al., 2008), doming by syn-extensional plutons (Yin, 1991), and

boudinage resulting from bidirectional extension (Perry, 2005). While these alternative models are conceptually plausible, they lack the field support that bolster the prominent interpretations.

Earlier research on the corrugated nature of detachment faulting focused on the interpretation that corrugations developed as primary features, influenced by a preexisting foliation structure (Davis and Lister, 1988), or that the rigid underside of a corrugated hanging wall imparts its undulatory form in a plastically deforming footwall that hardens with cooling due to exhumation (Spencer and Reynolds, 1991; Spencer, 1999). Later studies suggest that corrugations develop after initial detachment formation due to syn-extensional shortening strain that has been documented in transcurrent settings (Mancktelow and Pavlis, 1994; Oldow et al., 2009). Shortening perpendicular to the extension direction is supported by the observation of lower plate folds with axes parallel to the direction of extension in the central Mojave, Death Valley, and eastern Colorado extensional corridor areas (Fletcher and Bartley 1994; Mancktelow and Pavlis, 1994; Holm et al., 1994; Singleton, 2013), and upper-plate folds with axes roughly parallel to the extension direction (Yin, 1991; Singleton, 2013). Based on the evidence in support of both interpretations of corrugation formation, as either primary or secondary features, it can be inferred that corrugations may be a combination of these processes within a single terrane. Corrugations are typically associated with shortening on the order of a kilometer and extension on the order of tens of kilometers. With respect to the WHMCC, sedimentary structures and geochronologic constraints in the hanging wall of the detachment

reveal that shortening perpendicular to extension is the dominant method of corrugation development with respect to this particular transcurrent system.

Differences between velocity from GPS stations and strain field orientations observed in the Walker Lane are difficult to reconcile under plane-strain conditions, and require transtensional nonplane strain to resolve the oblique displacement (Dewey, 2003; Oldow et al., 2008). In the SPLM system, the nonplane strain associated with the transtensional deformation results in constrictional strain (Oldow et al., 2008) that is responsible for the progressive growth of corrugations in the lower plate of the detachment. Key lines of evidence from deformation and growth structures present in the upper-plate of the WHMCC yield insight into the timing of folding with respect to detachment activity. Spatial relationships between corrugations and folding in the upper plate of the detachment as well as temporally constrained onlapping strata defining a progressive unconformity in supradetachment sediments assert that folding in the WHMCC system was progressive and coeval with slip along the detachment (Figure 21). This evidence reveals that extension-perpendicular contractional strain was the dominant mechanism in generating the current geometry of corrugations exposed in the SPLM extensional complex. Despite this study's support for corrugations as a secondary feature, there is no evidence that can discount the potential for some of the undulatory geometry owing to primary folding initiated during the initial formation of the detachment. Regardless, it can be validated that the corrugation has increased in amplitude during late-stage detachment activity.

6. CONCLUSIONS

The WHMCC is located in a segment of the western Cordillera that has experienced Miocene Basin-and-Range style E-W extension overprinted by Mio-Pliocene Walker Lane transtension and core complex formation. Zircon U-Pb ages from lower plate rocks record Late Cretaceous and early Miocene (~19 Ma) magmatic events. Early Miocene plutonism was previously undocumented in the SPLM area. ZHe cooling ages from the lower plate represent cooling of the plutonic rocks below ~180˚C over a period from 12.1±1.9 Ma to 19.3±1.9 Ma, correlating to exhumation above ~6 km. AHe ages record rapid cooling of the entire footwall below ~60˚C, recording exhumation of the lower plate to depths of ~2 km by 9 Ma. Timing of exhumation along the detachment is constrained by (U-Th)/He thermochronometry of plutonic rocks and detailed chronostratigraphy of upper-plate strata to be bracketed between 9-6 Ma.

Previous research conducted in the WHMCC area suggested that upper-plate sediments were deposited as a single, temporally continuous stratigraphic package of supradetchment sediments, known as the Esmeralda Formation. ZHe geochronology reveals that the extensional allochthon represents three temporally distinct unconformity-bounded stratigraphic packages. The Lone Mountain group records deposition from ~23 Ma to 18 Ma, and sediments of the Weepah Hills group were deposited between ~12 Ma to 10 Ma. The Alum group is the upper sedimentary package, with sediments deposited from ~9 Ma to ~6 Ma. Zircons sampled from throughout the upper-plate stratigraphy have not been thermally reset, suggesting that the basin sediments have been buried no

deeper than ~6 km. Correlating the eruptive ZHe ages from basin sediments with lower plate cooling ages establishes that the three sedimentary packages record segments of basin evolution across the kinematic transition from Miocene extension (Lone Mountain group and Weepah Hills group) to Mio-Pliocene transtension (Alum group). Folding and a progressive unconfomity recorded in the upper-plate both correspond spatially to lower plate corrugations, suggesting that corrugation amplification can occur during late-stage detachment faulting in transtensional settings.

7. REFERENCES

Albers, J. P., and Stewart, J. H., 1972, Geology and mineral deposits of Esmeralda County, Nevada, Mackay School of Mines, University of Nevada.

Allmendinger, R.W., Cardozo, N., and Fisher, D., 2012, Structural geology algorithms: Vectors and tensors in structural geology: Cambridge University Press.

Atwater, T., and Stock, J., 1998, Pacific-North America plate tectonics of the Neogene southwestern United States: An Update: International Geology Review, v. 40, no. 5, p. 375-402.

Axen, G. J., and Fletcher, J. M., 1998, Late Miocene-Pleistocene extensional faulting, northern Gulf of California, Mexico and Salton Trough, California: International Geology Review, v. 40, no. 3, p. 217-244.

Bartley, J. M., Glazner, A. F., Coleman, D. S., Kylander-Clark, A., Mapes, R., and Friedrich, A. M., 2007, Large Laramide dextral offset across Owens Valley, California, and its possible relation to tectonic unroofing of the southern Sierra Nevada: Geological Society of America Special Papers, v. 434, p. 129-148.

Bennett, R. A., Wernicke, B. P., Niemi, N. A., Friedrich, A. M., and Davis, J. L., 2003, Contemporary strain rates in the northern Basin and Range province from GPS data: Tectonics, v. 22, no. 2.

Burchfiel, B., Cowan, D., and Davis, G., 1992, Tectonic overview of the Cordilleran orogen in the western United States: The Cordilleran orogen: Conterminous US: Boulder, Colorado, Geological Society of America, Geology of North America, v. 3, p. 407-479.

Burchfiel, B. C., Hodges, K. V., and Royden, L. H., 1987, Geology of Panamint Valley - Saline Valley Pull-Apart System, California: Palinspastic evidence for low-angle geometry of a Neogene Range-Bounding Fault: Journal of Geophysical Research: Solid Earth, v. 92, no. B10, p. 10422-10426.

Cashman, P. H., and Fontaine, S. A., 2000, Strain partitioning in the northern Walker Lane, western Nevada and northeastern California: Tectonophysics, v. 326, no. 1, p. 111-130.

Christiansen, R., Yeats, R., Graham, S., Niem, W., Niem, A., and Snavely, P., 1992, Post-Laramide geology of the US Cordilleran region: The Cordilleran orogen: Conterminous US: Boulder, Colorado, Geological Society of America, Geology of North America, v. 3, p. 261-406.

Davis, D. W., Krogh, T. E., and Williams, I. S., 2003, Historical development of zircon geochronology: Reviews in mineralogy and geochemistry, v. 53, no. 1, p. 145-181.

Davis, G.A., and Lister, G.S., 1988, Detachment faulting in continental extension; perspectives from the southwestern U.S. Cordillera, *in* Clark, S.P., Jr., et al., eds., Processes in Continental Lithosphere Deformation: Geological Society of America Special Paper 218, p. 133-159.

Diamond, D. S., and Ingersoll, R. V., 2010, Structural and Sedimentologic Evolution of a Miocene Supradetachment Basin, Silver Peak Range and Adjacent Areas, West-Central Nevada: International Geology Review, v. 44, no. 7, p. 588-623.

Dilles, J. H., and Gans, P. B., 1995, The chronology of Cenozoic volcanism and deformation in the Yerington area, western Basin and Range and Walker Lane: Geological Society of America Bulletin, v. 107, no. 4, p. 474-486.

Dixon, T. H., Miller, M., Farina, F., Wang, H., and Johnson, D., 2000, Present-day motion of the Sierra Nevada block and some tectonic implications for the Basin and Range province, North America: Tectonics, v. 19, p. 1-24.

Dodson, M. H., 1973, Closure temperature in cooling geochronological and petrological systems: Contributions to Mineralogy and Petrology, v. 40, no. 3, p. 259-274.

Dokka, R. K., and Travis, C. J., 1990, Role of the Eastern California Shear Zone in accommodating Pacific-North American Plate motion: Geophysical Research Letters, v. 17, no. 9, p. 1323-1326.

Dorsey, R. J., and Becker, U. L. F., 1995, Evolution of a large Miocene growth structure in the upper plate of the Whipple detachment fault, northeastern Whipple Mountains, California: Basin Research, v. 7, no. 2, p. 151-163.

Farley, K., Wolf, R., and Silver, L., 1996, The effects of long alpha-stopping distances on (U-Th)/He ages: Geochimica et Cosmochimica Acta, v. 60, no. 21, p. 4223-4229.

Faulds, J. E., and Henry, C. D., 2008, Tectonic influences on the spatial and temporal evolution of the Walker Lane: An incipient transform fault along the evolving Pacific–North American plate boundary: Ores and orogenesis: Circum-Pacific tectonics, geologic evolution, and ore deposits: Arizona Geological Society Digest, v. 22, p. 437-470.

Faulds, J. E., Henry, C. D., and Hinz, N. H., 2005, Kinematics of the northern Walker Lane: An incipient transform fault along the Pacific–North American plate boundary: Geology, v. 33, no. 6, p. 505-508.

Faulds, J. E., and Varga, R. J., 1998, The role of accommodation zones and transfer zones in the regional segmentation of extended terranes: Geological Society of America Special Papers, v. 323, p. 1-45.

Faure, G., 1998, Principles and applications of geochemistry: a comprehensive textbook for geology students: Prentice Hall.

Feng, R., Machado, N., and Ludden, J., 1993, Lead geochronology of zircon by Laser-Probe-Inductively coupled plasma mass spectrometry (LP-ICPMS): Geochimica et Cosmochimica Acta, v. 57, no. 14, p. 3479-3486.

Fletcher, J.M., and Bartley, J.M., 1994, Constrictional strain in a non-coaxial shear zone: Implications for fold and rock fabric development, central Mojave metamorphic core complex, California: Journal of Structural Geology, v. 16, p. 555-570.

Foy, T. A., Frankel, K. L., Lifton, Z. M., Johnson, C. W., and Caffee, M. W., 2012, Distributed extensional deformation in a zone of right-lateral shear: Implications for geodetic versus geologic rates of deformation in the eastern California shear zone-Walker Lane: Tectonics, v. 31, no. 4.

Frankel, K. L., Brantley, K. S., Dolan, J. F., Finkel, R. C., Klinger, R. E., Knott, J. R., Machette, M. N., Owen, L. A., Phillips, F. M., Slate, J. L., and Wernicke, B. P., 2007a, Cosmogenic 10Be and 36Cl geochronology of offset alluvial fans along the northern Death Valley fault zone: Implications for transient strain in the eastern California shear zone: Journal of Geophysical Research: Solid Earth, v. 112, no. B6.

Frankel, K. L., Dolan, J. F., Finkel, R. C., Owen, L. A., and Hoeft, J. S., 2007b, Spatial variations in slip rate along the Death Valley-Fish Lake Valley fault system determined from LiDAR topographic data and cosmogenic 10Be geochronology: Geophysical Research Letters, v. 34, no. 18.

Frankel, K. L., Glazner, A. F., Kirby, E., Monastero, F. C., Strane, M. D., Oskin, M. E., Unruh, J. R., Walker, J. D., Anandakrishnan, S., Bartley, J. M., Coleman, D. S., Dolan, J. F., Finkel, R. C., Greene, D., Kylander-Clark, A., Marrero, S., Owen, L. A., and Phillips, F., 2008, Active tectonics of the eastern California shear zone: Field Guides, v. 11, p. 43-81.

Friedmann, S. J., Davis, G. A., and Fowler, T. K., 1996, Geometry, paleodrainage, and geologic rates from the Miocene Shallow Valley supradetachment basin, eastern Mojave Desert, California: Geological Society of America Special Papers, v. 303, p. 85-105.

Fryer, B. J., Jackson, S. E., and Longerich, H. P., 1993, The application of laser ablation microprobe-inductively coupled plasma-mass spectrometry (LAM-ICP-MS) to in situ (U)- Pb geochronology: Chemical Geology, v. 109, no. 1, p. 1-8.

Ganev, P. N., Dolan, J. F., Frankel, K. L., and Finkel, R. C., 2010, Rates of extension along the Fish Lake Valley fault and transtensional deformation in the Eastern California shear zone–Walker Lane belt: Lithosphere, v. 2, no. 1, p. 33-49.

Gans, P., and Bohrson, W., 1998, Suppression of volcanism during rapid extension in the Basin and Range Province, United States: Science, v. 279, no. 5347, p. 66-68.

Gans, P. B., Mahood, G. A., and Schermer, E., 1989, Synextensional magmatism in the Basin and Range province: A case study from the eastern Great Basin, Geological Society of America Boulder, CO.

Hammond, W. C., and Thatcher, W., 2004, Contemporary tectonic deformation of the Basin and Range province, western United States: 10 years of observation with the Global Positioning System: Journal of Geophysical Research: Solid Earth, v. 109, no. B8.

Hardy, S., and Poblet, J., 1994, Geometric and numerical model of progressive limb rotation in detachment folds: Geology, v. 22, no. 4, p. 371-374.

Hardyman, R., and Oldow, J., Tertiary tectonic framework and Cenozoic history of the central Walker Lane, Nevada, in Proceedings Geology and ore deposits of the Great Basin: Geological Society of Nevada Symposium Proceedings1991, Volume 1, p. 279-301.

Henry, C. D., Faulds, J. E., and dePolo, C. M., 2007, Geometry and timing of strike-slip and normal faults in the northern Walker Lane, northwestern Nevada and northeastern California: Strain partitioning or sequential extensional and strike-slip deformation?: Geological Society of America Special Papers, v. 434, p. 59-79.

Hoeft, J. S., and Frankel, K. L., 2010, Temporal variations in extension rate on the Lone Mountain fault and strain distribution in the eastern California shear zone–Walker Lane: Geosphere, v. 6, no. 6, p. 917-936.

Holm, D.K., Fleck, R.J. and Lux, D.R., 1994, The Death Valley Turtlebacks reinterpreted as Miocene-Pliocene folds of a major detachment surface: The Journal of Geology, v. 102, p. 718-727.

House, M., Farley, K., and Stockli, D., 2000, Helium chronometry of apatite and titanite using Nd-YAG laser heating: Earth and Planetary Science Letters, v. 183, no. 3, p. 365-368.

Humphreys, E. D., and Weldon, R. J., 1994, Deformation across the western United States: A local estimate of Pacific-North America transform deformation: Journal of Geophysical Research: Solid Earth, v. 99, no. B10, p. 19975-20010.

Kirsch, S. A., 1971, Chaos Structure and Turtleback Dome, Mineral Ridge, Esmeralda County, Nevada: Geological Society of America Bulletin, v. 82, no. 11, p. 3169-3176.

Kruger, J. M., Johnson, R. A., and Houser, B. B., 1995, Miocene-Pliocene half-graben evolution, detachment faulting and late-stage core complex uplift from reflection seismic data in south-east Arizona: Basin Research, v. 7, no. 2, p. 129-149.

Kylander-Clark, A. R. C., Coleman, D. S., Glazner, A. F., and Bartley, J. M., 2005, Evidence for 65 km of dextral slip across Owens Valley, California, since 83 Ma: Geological Society of America Bulletin, v. 117, no. 7-8, p. 962-968.

Lee, J., Spencer, J., and Owen, L., 2001, Holocene slip rates along the Owens Valley fault, California: Implications for the recent evolution of the Eastern California Shear Zone: Geology, v. 29, no. 9, p. 819-822.

Lee, J., Stockli, D. F., Owen, L. A., Finkel, R. C., and Kislitsyn, R., 2009, Exhumation of the Inyo Mountains, California: Implications for the timing of extension along the western boundary of the Basin and Range Province and distribution of dextral fault slip rates across the eastern California shear zone: Tectonics, v. 28, no. 1.

Mancktelow, N.S., Pavlis, T.L., 1994, Fold-fault relationships in low-angle detachment systems: Tectonics, v. 13, p. 668-685.

Nielsen, R. L., 1965, Right-lateral strike-slip faulting in the Walker Lane, west-central Nevada: Geological Society of America Bulletin, v. 76, no. 11, p. 1301-1308.

Oldow, J., Late Cenozoic displacement partitioning in the northwestern Great Basin, in Proceedings Structure, Tectonics and Mineralization of the Walker Lane, Stewart, J., ed., Walker Lane Symposium Proceedings Volume, Geological Society of Nevada, Reno, NV1992, p. 17-52.

Oldow, J. S., 1984, Evolution of a late Mesozoic back-arc fold and thrust belt, northwestern Great Basin, USA: Tectonophysics, v. 102, no. 1, p. 245-274.

Oldow, J. S., 2003, Active transtensional boundary zone between the western Great Basin and Sierra Nevada block, western US Cordillera: Geology, v. 31, no. 12, p. 1033-1036.

Oldow, J. S., Aiken, C. L. V., Hare, J. L., Ferguson, J. F., and Hardyman, R. F., 2001, Active displacement transfer and differential block motion within the central Walker Lane, western Great Basin: Geology, v. 29, no. 1, p. 19-22.

Oldow, J. S., Elias, E. A., Ferranti, L., McClelland, W. C., and McIntosh, W. C., 2009, Late Miocene to Pliocene synextensional deposition in fault-bounded basins within the upper plate of the western Silver Peak–Lone Mountain extensional complex, west-central Nevada: Geological Society of America Special Papers, v. 447, p. 275-312.

Oldow, J. S., Geissman, J. W., and Stockli, D. F., 2008, Evolution and Strain Reorganization within Late Neogene Structural Stepovers Linking the Central Walker Lane and Northern Eastern California Shear Zone, Western Great Basin: International Geology Review, v. 50, no. 3, p. 270-290.

Oldow, J. S., Kohler, G., and Donelick, R. A., 1994, Late Cenozoic extensional transfer in the Walker Lane strike-slip belt, Nevada: Geology, v. 22, no. 7, p. 637-640.

Oskin, M., Perg, L., Blumentritt, D., Mukhopadhyay, S., and Iriondo, A., 2007, Slip rate of the Calico fault: Implications for geologic versus geodetic rate discrepancy in the Eastern California Shear Zone: Journal of Geophysical Research: Solid Earth, v. 112, no. B3.

Oswald, J. A., and Wesnousky, S. G., 2002, Neotectonics and Quaternary geology of the Hunter Mountain fault zone and Saline Valley region, southeastern California: Geomorphology, v. 42, no. 3–4, p. 255-278.

Peltzer, G., Crampé, F., Hensley, S., and Rosen, P., 2001, Transient strain accumulation and fault interaction in the Eastern California shear zone: Geology, v. 29, no. 11, p. 975-978.

Petronis, M. S., Geissman, J. W., Oldow, J. S., and McIntosh, W. C., 2007, Tectonism of the southern Silver Peak Range: Paleomagnetic and geochronologic data bearing on the Neogene development of a regional extensional complex, central Walker Lane, Nevada: Geological Society of America Special Papers, v. 434, p. 81-106.

Petronis, M. S., Geissman, J. W., Oldow, J. S., and McIntosh, W. C., 2009, Late Miocene to Pliocene vertical-axis rotation attending development of the Silver Peak–Lone Mountain displacement transfer zone, west-central Nevada: Geological Society of America Special Papers, v. 447, p. 215-253.

Proffett, J. M., 1977, Cenozoic geology of the Yerington district, Nevada, and implications for the nature and origin of Basin and Range faulting: Geological Society of America Bulletin, v. 88, no. 2, p. 247-266.

Reheis, M. C., and Sawyer, T. L., 1997, Late Cenozoic history and slip rates of the Fish Lake Valley, Emigrant Peak, and Deep Springs fault zones, Nevada and California: Geological Society of America Bulletin, v. 109, no. 3, p. 280-299.

Reiners, P. W., 2005, Zircon (U-Th)/He Thermochronometry: Reviews in Mineralogy and Geochemistry, v. 58, no. 1, p. 151-179.

Reiners, P. W., Farley, K. A., and Hickes, H. J., 2002, He diffusion and (U–Th)/He thermochronometry of zircon: initial results from Fish Canyon Tuff and Gold Butte: Tectonophysics, v. 349, no. 1, p. 297-308.

Reiners, P. W., Spell, T. L., Nicolescu, S., and Zanetti, K. A., 2004, Zircon (U-Th)/He thermochronometry: He diffusion and comparisons with $^{40}Ar/^{39}Ar$ dating: Geochimica et Cosmochimica Acta, v. 68, no. 8, p. 1857-1887.

Robinson, P. T., Stewart, J. H., Moiola, R. J., and Albers, J. P., 1976, Geologic map of the Rhyolite Ridge quadrangle: Esmeralda County, Nevada: US Geological Survey Geologic Quadrangle Map GQ-1325, scale, v. 1, no. 62,500.

Ryan, W. B. F., et al., 2009, Global Multi-Resolution Topography synthesis, Geochem. Geophys. Geosyst., Q03014, doi: 10.10292008GC002332.

Schneider, C. L., Hummon, C., Yeats, R. S., and Huftile, G. L., 1996, Structural evolution of the northern Los Angeles basin, California, based on growth strata: Tectonics, v. 15, no. 2, p. 341-355.

Singleton, J.S., 2013, Development of extension-parallel corrugations in the Buckskin-Rawhide metamorphic core complex, west-central Arizona: Geological Society of America Bulletin, v. 125, no. 3/4, p. 453-472.

Spencer, J.E., 1985, Miocene low-angle normal faulting and dike emplacement at Homer Mountain and surrounding areas, southeastern California and southernmost Nevada: Geological Society of America Bulletin, v. 96, p. 1140-1155.

Spencer, J.E., 1999, Geologic continuous casting below continental and deep-sea detachment faults and at the striated extrusion of Sacsayhuaman, Peru: Geology, v. 27, p. 327-330.

Spencer, J.E., and Reynolds, S.J., 1991, Tectonics of mid-Tertiary extension along a transect through west central Arizona: Tectonics, v. 10, p. 1204-1221.

Stewart, J., 1988, Tectonics of the Walker Lane belt, western Great Basin: Mesozoic and Cenozoic deformation in a zone of shear: Metamorphism and crustal evolution of the western United States, v. 7, p. 683-713.

Stewart, J. H., 1985, east-trending dextral faults in the western Great Basin: An explanation for anomalous trends of pre-Cenozoic strata and Cenozoic faults: Tectonics, v. 4, no. 6, p. 547-564.

Stewart, J.H., 1998, Regional characteristics, tilt domains, and extensional history of the later Cenozoic Basin and Range Province, western North America: Geological Society of America Special Papers, v. 323, p. 47-74.

Stewart, J. H., and Diamond, D., 1990, Changing patterns of extensional tectonics; overprinting of the basin of the middle and upper Miocene Esmeralda Formation in western Nevada by younger structural basins: Basin and Range extensional tectonics near the latitude of Las Vegas, Nevada: Geological Society of America Memoir, v. 176, p. 447-476.

Stockli, D. F., 2005, Application of low-temperature thermochronometry to extensional tectonic settings: Reviews in Mineralogy and Geochemistry, v. 58, no. 1, p. 411-448.

Stockli, D. F., Dumitru, T. A., McWilliams, M. O., and Farley, K. A., 2003, Cenozoic tectonic evolution of the White Mountains, California and Nevada: Geological Society of America Bulletin, v. 115, no. 7, p. 788-816.

Stockli, D. F., Farley, K. A., and Dumitru, T. A., 2000, Calibration of the apatite (U-Th)/He thermochronometer on an exhumed fault block, White Mountains, California: Geology, v. 28, no. 11, p. 983-986.

Stockli, D. F., Surpless, B. E., Dumitru, T. A., and Farley, K. A., 2002, Thermochronological constraints on the timing and magnitude of Miocene and Pliocene extension in the central Wassuk Range, western Nevada: Tectonics, v. 21, no. 4, p. 1028.

Surpless, B., 2008, Modern strain localization in the central Walker Lane, western United States: Implications for the evolution of intraplate deformation in transtensional settings: Tectonophysics, v. 457, no. 3–4, p. 239-253.

Surpless, B. E., Stockli, D. F., Dumitru, T. A., and Miller, E. L., 2002, Two-phase westward encroachment of Basin and Range extension into the northern Sierra Nevada: Tectonics, v. 21, no. 1, p. 2-1-2-10.

Tincher, C. R., and Stockli, D. F., 2009, Cenozoic volcanism and tectonics in the Queen Valley area, Esmeralda County, western Nevada: Geological Society of America Special Papers, v. 447, p. 255-274.

Wernicke, B., 1992, Cenozoic extensional tectonics of the US Cordillera: The Geology of North America, v. 3, p. 553-581.

Wesnousky, S. G., 2005, The San Andreas and Walker Lane fault systems, western North America: transpression, transtension, cumulative slip and the structural evolution of a major transform plate boundary: Journal of Structural Geology, v. 27, no. 8, p. 1505-1512.

Wolf, R., Farley, K., and Silver, L., 1996, Helium diffusion and low-temperature thermochronometry of apatite: Geochimica et Cosmochimica Acta, v. 60, no. 21, p. 4231-4240.

Wolfe, M. R., and Stockli, D. F., 2010, Zircon (U–Th)/He thermochronometry in the KTB drill hole, Germany, and its implications for bulk He diffusion kinetics in zircon: Earth and Planetary Science Letters, v. 295, no. 1, p. 69-82.

Yin, A., 1991, Mechanisms for the formation of domal basinal detachment faults: A three dimensional analysis: Journal of Geophysical Research, v. 96, p. 14,577-14,594, doi: 10.1029/91JB01113.

Zeitler, P., Herczeg, A., McDougall, I., and Honda, M., 1987, U-Th-He dating of apatite: A potential thermochronometer: Geochimica et Cosmochimica Acta, v. 51, no. 10, p. 2865-2868.